UNIVERSITÀ
DEGLI STUDI
FIRENZE

DOTTORATO DI RICERCA IN

Earth Sciences

CICLO XXXIII

COORDINATORE Prof. Francalanci Lorella

Regional scale satellite monitoring for hydrogeological risk reduction

Settore Scientifico Disciplinare GEO/05

Dottorando

Dott. Montalti Roberto

Tutore

Prof. Catani Filippo

Coordinatore

Prof Francalanci Lorella

Anni 2017/2020 *(di inizio e fine corso)*

"Έτσι, δεν γνωρίζω"

Table of Contents

Abstract

In the last decade satellite remote sensing has become an effective tool for monitoring geo-hazard-induced ground motions, and has been increasingly used by scientific community. Geo-hazards direct and indirect costs are currently rising, causing serious socio-economics and casualty losses. Therefore, creating a priority list turns out to be essential to highlight the most relevant ground deformations and to better focus the risk management practices at regional scale. The Sentinel-1 constellation, thanks to the 6-days repeatability and the free availability of the data, allows to easily update the geo-hazard-induced ground motions, compared to other kind of satellite sensors

In this PhD Thesis, the potentialities and drawbacks of the interferometric technique have been presented and then exploited to define three different procedures, applied in different environment and at different scales, for the use of multi-band PSI products. This thesis work represents the main outcome of a three years-long activity at the Department of Earth Sciences of the University of Florence, Centre technologic de telecomunicacions de Catalunya research center and TRE-Altamira (Barcelona). The main goal is to test and evaluate the potential and applicability of space-borne SAR data, processed by means of different PSI approaches, as operational tools for the characterization of geohazards in different geological and geomorphological environments.

For this work, two Italian test areas at regional scale are been selected: Tuscany and Valle d'Aosta Regions. Furthermore a site at detailed scale was analyzed, the mining area of Saline di Volterra (Tuscany). The main goal of the thesis hinges on illustrating different methodologies that could be merged in one single workflow to detect active moving areas, characterize them in detail and cross-correlate the satellite data with ancillary information, implementing the obtained products and results in the Civil Protection chain and geohazard risk management. The proposed case studies were intended as examples, although referred to different environments and geohazards, for the working approaches to be used from regional to detailed scale.

For the Tuscany Region, there were exploited Sentinel-1 images for active moving areas detection at regional scale. A hotspot-like methodology was used, exploiting the temporal repetitiveness of Sentinel-1 data analysed by means of the SqueeSAR algorithm to create deformation maps in three different periods with a 6 months update. Thanks to a filtering approach based on a velocity threshold, it was possible extract a total of 652 deformation clusters, divided in three different periods, to study their spatial and temporal evolution. The final output is a flexible geo-database that contains interferometric parameters, geographical, geomorphological and geological information, a brief evaluation of the possible triggering cause and information about the temporal evolution of the moving areas.

For the Valle d'Aosta Region, it was used a clustering analysis applied to a large stack of Sentinel-1 satellite interferometric products that has been derived using the SqueeSAR algorithm. Valle d'Aosta Region is an alpine region characterized by a wide spectrum of mass wasting phenomena. The approach, based on simple GIS tools and indexes, allowed detecting 277 moving areas above the selected velocity threshold. Overall, landslides (complex, rotational, Deep Seated Gravitational Slope Deformation (DSGSD)), rock glacier evolution and detrital-related deformation are responsible for the detected motions.
In mountainous areas, where the field data collection is sometimes limited or impossible, the presented approach is intended to create priority areas to be focused for further investigations. In this way, it is possible to increase, with reduced economic and personnel costs, the "landslide knowledge" of all the actors involved within the landslide risk management chain at regional scale.

In this context, easily updatable clustering methodologies are very useful tools for MTInSAR data analysts; it is possible to obtain reliable results in a fast way and to compare them with previous results.
Well knowing the limitations of the interferometric technique, especially in mountain regions, it is reasonable to rely on clustering approaches in order to derive multi-temporal synoptic views of ground motions over wide areas.

For the Saline di Volterra case, it is presented a local scale application of multi-temporal satellite interferometry targeting a solution mining area in southern Tuscany. The surroundings of Saline di Volterra host several brine wells that pump water into a salt level at a depth ranging between 60 and 400 m below surface. The mining activity has a relevant environmental impact in terms of depletion of the water resources and in terms of ground motion, creating several sinkholes which were mapped through multi-temporal analysis of orthophotos. The deformation map, obtained through the analysis of Sentinel-1 images, revealed the presence of several subsidence bowls, sometimes corresponding to sinkholes formed in the recent past. The subsidence bowls have a common deformation pattern, with LOS velocities increasing forward the center of the bowl. The temporal evolution of the measurement points can vary a lot on case-basis. Finally, a correlation between LOS velocities and age of formation of sinkholes have been found. The Sentinel-1 images were processed with an ad hoc processing chain, elaborated in Centre Technologic Telecomunicacions Catalunya research center (Barcelona). With this new procedure, it was possible to detect fast deformation rates that are usually puzzling to solve in mining areas. This detailed scale and target-oriented approach demonstrated its capability to provide useful information in terms of density of measurement points and quality of the time series.

Riassunto

Nell'ultimo decennio il telerilevamento satellitare è diventato uno fra gli strumenti più efficaci per il monitoraggio dei movimenti del suolo innescati dai geohazards. I costi diretti e indiretti di quest'ultimi sono attualmente in aumento, causando numerose problematiche socio-economiche. Pertanto, la creazione di una priority list risulta fondamentale per evidenziare le deformazioni del suolo più rilevanti e per gestire al meglio il rischio idrogeologico a scala regionale. La costellazione Sentinel-1, grazie al tempo di rivisitazione di soli 6 giorni e alla fruizione gratuita delle immagini, permette di aggiornare facilmente le aree in deformazione, rispetto ad altri tipi di sensori satellitari.

Questo lavoro rappresenta il risultato principale di tre anni di attività presso il Dipartimento di Scienze della Terra dell'Università di Firenze, il centro di ricerca Centre technologic de telecomunicacions de Catalunya (Barcelona) e TRE-Altamira (Barcelona). L'obiettivo principale è quello di testare e valutare il potenziale e l'applicabilità dei dati SAR spaziali, elaborati attraverso diversi approcci PSI, come strumenti operativi per la caratterizzazione dei geohazards in diversi patterns geologici e geomorfologici.

Per questo lavoro sono state selezionate come aree d'analisi le Regioni Toscana e Valle d'Aosta. Inoltre è stata analizzata anche l'area mineraria di Saline di Volterra, come sito a scala locale. L'obiettivo principale della tesi consiste nell'elaborare una metodologia efficace in grado di evidenziare le aree in deformazione più rappresentative, cross-correlando i dati satellitari con i dati ancillari a disposizione. Questo per migliorare le procedure di protezione civile per la gestione del rischio idrogeologico.

Per la Regione Toscana sono state utilizzate le immagini Sentinel-1 per il rilevamento delle aree in deformazione. Le immagini satellitari sono state elaborate con l'algoritmo SqueeSAR, in modo da ricavare mappe di deformazione in tre diversi periodi temporali, di sei mesi in sei mesi. L'obiettivo è stato quello di estrarre dei cluster di deformazione (un totale di 652), tramite una metodologia hotspot-like, che si basa sul filtraggio dei punti delle mappe di deformazione a seconda di una soglia specifica di velocità. Il risultato finale è un geodatabase flessibile che contiene parametri interferometrici, informazioni geografiche, geomorfologiche e geologiche, una breve valutazione della possibile causa scatenante e informazioni sull'evoluzione temporale delle aree in movimento.

Allo stesso modo, Per la Regione Valle d'Aosta è stata utilizzata una metodologia hotspot-like, processando le immagini Sentinel-1 mediante l'algoritmo SqueeSAR, permettendo di rilevare 277 aree in deformazione al di sopra della soglia di velocità applicata ai punti delle mappe di deformazione. La Regione Valle d'Aosta si trova in un contesto geomorfologico alpino, dove gli episodi di natura franosa sono piuttosto frequenti, come ad esempio le deformazioni gravitative profonde di versante. Nelle aree montuose, dove la raccolta di dati sul campo può essere limitata o impossibile, è fondamentale avere a disposizione un database con le aree di deformazione più rappresentative, per migliorare e rendere più gestibile la gestione del rischio idrogeologico. Tenendo conto dei limiti dell'interferometria satellitare in aree montuose, è stato possibile in ogni caso estrarre i cluster di deformazione, che hanno permesso una visione e una maggiore comprensione a larga scala del dissesto idrogeologico regionale.

Il caso Saline di Volterra rappresenta un'applicazione a scala locale dell'interferometria satellitare multi-temporale mirata all'analisi dell'area mineraria in zona. L'area all'interno di Saline viene sfruttata per l'estrazione di sale tramite dissoluzione. Questa tecnica consiste nel pompare acqua tramite dei pozzi negli strati d'alite nel sottosuolo, ad una profondità compresa tra 60 e 400 m. Successivamente l'acqua satura in sale viene pompata in superficie dove viene raccolta per la purificazione del minerale. L'attività mineraria ha un impatto ambientale rilevante in termini di esaurimento delle risorse idriche e di deformazione del suolo. Infatti, nelle aree circostanti ai pozzi, si formano cavità che danno origine a movimenti rapidi di subsidenza, che possono causare anche il collasso della superficie dando origine a fenomeni chiamati sink-holes. La mappa di deformazione, ottenuta attraverso l'analisi delle immagini di Sentinel-1, ha rivelato la presenza di diverse bolle di deformazione riconducibili a fenomeni di subsidenza, talvolta corrispondenti a sink-holes formati in passato. Le immagini Sentinel-1 sono state elaborate con una processing chain ad hoc, ideata nel centro di ricerca Centre Technologic Telecomunicacions Catalunya (Barcellona). Con questa nuova procedura, è stato possibile rilevare tassi di deformazione dalle velocità molto elevate, solitamente difficile da individuare in un contesto minerario. Questo approccio target oriented ha permesso di fornire risultati ottimi in termini di densità dei punti di misura e qualità delle serie temporali.

1.Introduction

In the last two decades, the high number of available spaceborne sensors able to quantify geophysical phenomena associated with earth surface movements (earthquakes, landslides, etc) changed the way the scientific community assesses and predicts natural disasters. The increasingly common use of Earth Observation (EO) techniques is in part due to increased awareness of environmental issues such as climate change, but also to the increase in geospatial technologies and the ability to provide up-to-date imagery to the public through the media and internet (Joyce et al., 2009). The scientific knowledge gained along with the ability to disseminate timely geospatial information is contributing to comprehensive risk mitigation planning and improved disaster response (Tralli et al., 2005). As technology is enhanced, expectations for near real-time assessment of natural hazard increase because of the improvements made to the satellite platforms (data acquisition rates, ground resolution) and to the reliability of processing and image analysis algorithms (Gillespie et al., 2007).

Observations from Earth orbiting satellites are complementary to local and regional airborne observations, and to traditional *in situ* field measurements and ground-based sensor networks in Earth and Environmental sciences. Satellite remote sensing is proving a systematic framework for scientific knowledge of the Earth, integrating multi-scale observations over a broad portion of the electromagnetic spectrum with increasingly refined spatial and spectral resolution and over time scales that encompass phenomenological lifecycles with requisite sampling frequency (Tralli et al., 2005). Advances in computational science and numerical simulations are allowing the study of long-term processes exploiting observational data for constraints and validation of the remotely sensed information (Donnellan et al., 2004).

Between 1999 and 2020, over 190 Earth observing satellites have been successfully launched (data provided by the ITC's database of satellites and sensors, available online at https://www.itc.nl/Pub/ sensordb). These satellites contain passive or active sensors that can be utilized by the scientific community for monitoring natural hazards. Passive sensors record reflected (visible and infrared wavelengths) and emitted energy (thermal wavelengths). Many passive sensors, providing panchromatic imagery are operational, such as IKONOS 2, QuickBird 2, SPOT 5 and OrbView 3 that acquire optical images at very high resolution (0.6 m to 2.5 m) and with short temporal repeatability (3 to 14 days). Shortwave infrared and thermal bands acquisition represent another commonly used application of passive sensors. MODIS and ASTER operate in these bands, with a lower ground resolution than panchromatic images (30m to 1 km) but with a very high temporal repeatability on an area (one day). Active sensors emit and receive an energy pulse to create an image; the most commonly used are the sensors using a radar (Radio Detecting and Ranging) signal that can penetrate cloud covers and that can operate both day and night. The radar sensors, known as Synthetic Aperture Radar (SAR), measures the backscattered microwave signal within discrete wavelengths (X-, C- and L- bands, ordered from the shortest to the longest).

The SAR sensors are the most commonly used for deriving ground deformation with centimeter to millimeter precision above large areas (up to 200 km) with medium (30 – 40 m for C-band data) to high resolution (1 m for X-band data). This is possible exploiting two or more SAR acquisitions above the same areas by means of the InSAR (Interferometric SAR) technique. This approach allows to derive the Earth's surface deformation with high precision and it is applicable for monitoring and detecting landslides, land subsidence, volcanic and tectonic motions. Moreover, has been successfully used to derive deformation data from single targets, with building scale analyses (Ferretti et al., 2006).

Many processing algorithms, generally named as Persistent Scatterer Interferometry (PSI), were developed, starting from early 2000, to retrieve the spatial distribution of displacements and their evolution along the monitored period at a relatively low cost over wide area. Thanks to the availability of historical archive datasets of SAR images acquired by ERS1/2 and ENVISAT satellites (ESA - European Spatial Agency), spanning from 1992 to 2010, and images by RADARSAT 1/2 (CSA - Canadian Spatial Agency) and Sentinel-1 (ESA) sensors, as well as satellite data from current X-band high resolution satellite systems, i.e. COSMO-SkyMed (ASI - Italian Space Agency) and TerraSAR-X (DLR - German Aerospace Center), PSI techniques can be applied to provide back analysis and monitoring of ground displacements with high precision up to about 1 mm/yr on a single measure. For all these characteristics, the PSI-derived products have demonstrated their usefulness as support tool for mapping and monitoring ground motions associated with a wide range of geohazards, from the local to the national scale (Bally et al., 2012).

In the last decade ESA, EC (European Commission), Civil Protection Authorities (CPA) and many other entities in charge of risk management started a wide range of projects contributing to the understanding, mitigation, preparedness and management of geological risks. In the European context, hydrogeological services and applications exploiting InSAR products are widely exploited and common part of the risk management chain in Italy, Switzerland and Spain and are becoming consolidated in Greece, Slovakia, Hungary, Germany, Poland and France. Many national initiatives such as the projects SLAM (Farina et al., 2006), DO-SMS (http://dosms.get.obs-mip.fr), and international projects such as ESA Terrafirma (Raspini et al., 2016), the EC FP7 SAFER (Casagli et al., 2016) and DORIS (http://www.doris-project.eu), are exploiting single-pair InSAR and multi-interferometric techniques such as Permanent Scatterer Interferometry (PSInSAR) and Small-Baseline (SBAS) approaches for geohazards mapping and operational support to regional and national bodies and local authorities in charge of hazard and risk management and land use planning. In Europe, thanks to the efforts made and the time spent by the scientific community in the last decade to make InSAR-based applications accepted among users and practitioners, 50 geological surveys have become users of terrain deformation services. Recent national initiatives (e.g., SAR.net 1/2 projects in 2005-2017) funded by the Italian National Civil Protection Department were carried out to enhance the acceptance of InSAR-based applications and services for landslide risk in Italy. These projects provided successful examples on how interferometric data can operatively support the CPA in the definition of operative procedures for the rapid assessment of risk during emergencies.

1.1 Purpose of the study

The thesis work represents the main outcome of three years-long activity at the Department of Earth Sciences of the University of Florence, with 1 year and a half of period abroad between the Centre Tecnològic Telecomunicacions Catalunya (CTTC) of Castelldefels (Barcelona) and TRE-Altamira (Barcelona). The main goal is to test and evaluate the potential and applicability of space-borne SAR data, processed by means of different PSI approaches, as operational tools for the characterization of geohazards in different geological and geomorphological environments, at regional and detailed scale. Three test sites were presented to show different approaches aimed both at reconstructing the deformation history of ground motions (mainly related to subsidence and landslides), in order to evaluate the effectiveness and the potential of InSAR data in a very different study areas geomorphological patterns, by means of the Sentinel-1 data analysis.

For the testing areas at regional scale, the methodology exploits a hot-spot-like method based on radar images processed by means of SqueeSAR algorithm to create a new geodatabase of moving areas, useful not

only from a scientific point view, but also for risk management and Civil Protection purposes. At the same time, a new processing chain for the detailed scale was developed, in order to overcome some InSAR limitation and highlight the fastest movements in the study area.

2 Radar Remote Sensing

Remote sensing data acquired by sensors operating in the microwave portion of the electromagnetic spectrum are nowadays widely used for detecting and monitoring hydrogeological phenomena. The microwaves are chosen between all the possible bands of the spectrum because of their capability of penetrating the atmosphere under virtually all conditions (clouds, smoke, night and so on). Moreover, the microwaves reflections or emissions from Earth materials bear no direct relationship to their counterparts in the visible or thermal portions of the spectrum (Lillesand and Kiefer, 1979). For example, a "rough" surface in the visible portion can appear "smooth" if seen by the microwaves and vice versa.

The word *radar* is an acronym for Radio Detection and Ranging, name that implies the use of radio waves to detect the presence of objects and determine their position (range). This process entails transmitting short burst or pulses of microwave energy, at a certain wavelength depending on the type of sensor, in the direction of interest, recording the strength and origin of the backscattered echoes received from different object in the field of view (FOV) of the sensor (Lillesand and Kiefer, 1979).

The capability of a sensor to identify as separate two closely spaced targets is called resolution. For a radar system, the resolution defines the minimum ground distance between two object that allows the receiving antenna to record two different backscattered signals, so identifying the targets in the radar image. In particular, a simple mathematical law regulates the resolution of a radar sensor in the azimuth direction, parallel to its orbit:

$R_{azimuth}=R \times b$

where R is the target-sensor distance and b is defined as:

$b = \lambda/L$

where b is the width of the radar beam, λ is the wavelength of the signal and L is the length of the transmitting antenna.

Considering these laws, for a beam width of 10 milliradians, at a distance of 800 km, the azimuth resolution will be 8 km; as the results suggest, this resolution is not suitable for monitoring ground movements, that are the final target of the microwave remote sensing. For guarantying a suitable resolution two changes have to be made: i) increase the length of the physical transmitting antenna or ii) use a shorter wavelength. The latter, would led to a higher atmosphere and cloud impact on the capability of imaging radars, so worsening the obtainable results. On the other hand, to obtain an acceptable azimuth resolution for a real-aperture radar system, it would be necessary a very long physical antenna, e.g. some kilometers long. This is due to the inverse relation between the area illuminated on the ground and the physical dimensions of the antenna (Skolnik, 2001).

For overcoming these limitations, the SAR (Synthetic Aperture Radar) systems were designed. A SAR system acquires at long wavelengths (centimetric) by using a small antenna and obtains the required ground resolution by means of a particular acquisition strategy (Figure 1). The SAR concept separates two targets at

the same range but at different azimuth positions by their dissimilar relative velocities with respect to the moving sensor. The reflected monochromatic waves from two different targets, illuminated by the same beam, have different Doppler shifts (phases) associated with them. Knowing the path of the satellite orbit, it is possible to compute the exact phase history for every point target on the ground. Multiple echoes are than combined to effectively create a synthetic aperture that is able to separate the two targets; this aperture is longer that the "real" one and so called *synthetic*. The final resolution is dependent on the total amount of phase information available for each target: the longer the target is illuminated, the higher is the resolution obtainable. A SAR sensor exploits a single beam antenna, few meters long, for repeatedly illuminating the area of interest; during the forward movement of the satellite, the scene is then illuminated from different positions in distinct instants, guarantying the necessary repeatability. Individual echoes, received successively at the different antenna positions, are recorded, stored, combined and then processed together, simulating a "synthetic aperture", to provide the required azimuth resolution (Hooper, 2006).

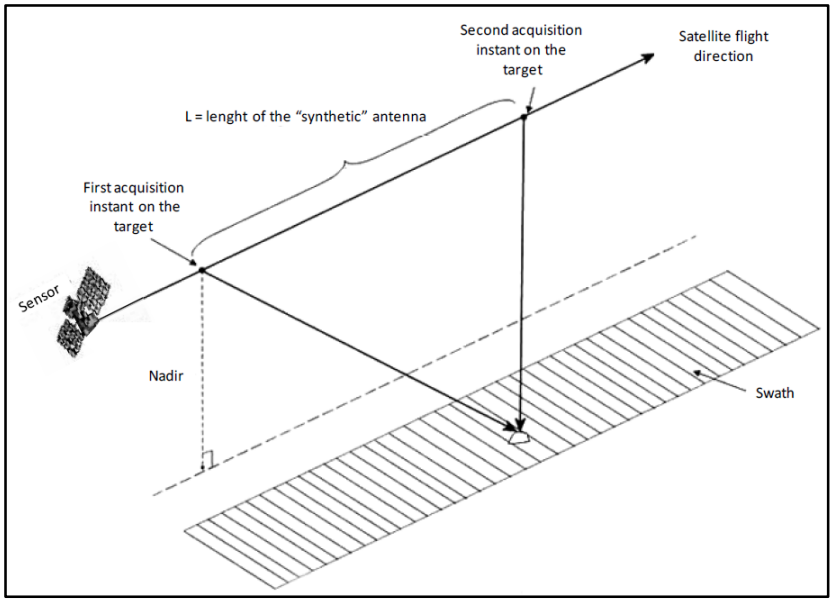

Figure 1 - SAR system: the sensor, observing repeatedly the target and recording the backscattered echoes, simulates a "real" aperture antenna, obtaining a high-resolution image (from http://treuropa.com).

The product acquired by a SAR sensor has to be processed in order to be used for further analysis. The algorithms of image analysis are used to convert the recorded echoes into a high-resolution image of ground in a Single Look Complex (SLC) format, that is the standard for this type of image processing. A review of the many different algorithms present in the scientific community was proposed by Cumming and Wong, 2005. The SLC image is composed by an array of complex numbers ordered in a matrix of pixels. The indices of pixels in the matrix are directly related to the azimuth and range position of the scatterers with respect to a reference point on the platform's path.

In particular, each pixel value corresponds to both amplitude and phase information about the backscattered microwave signal. The phase refers to the oscillation of electromagnetic waves of the radar signal and mainly depends on the sensor-to-target distance. The amplitude represents the radiation backscattered by the objects towards the radar. Typically, exposed rocks or metal structures have a high capacity to reflect incident radar energy and thus the amplitude of the corresponding pixel is high. Reflectivity of smooth flat surfaces like water basins or soil is lower, so the amplitude of the reflected signal decreases. Besides the material,

amplitude depends on the shape, size, orientation and moisture content of the scatterers, and on the characteristics of the radar beam (frequency, polarization and incident angle of the radar pulses).

A spaceborne SAR sensor is carried by a satellite along a predefined polar orbit with the transmitting antenna pointed to the ground surface in the plane perpendicular to the orbit (Hooper, 2006). The *incidence angle* of the radar signal on the assumed flat Earth surface is equal to the inclination of the antenna with respect to the nadir direction (*Off-nadir angle*). The SAR sensor are usually "right-looking", meaning that the antenna illuminates the ground surface always from the right side along its flight, this direction is called *azimuth direction*. The area illuminated on the ground is called *antenna footprint*, while the direction of the main lobe of the transmitting antenna is called *ground range direction*. The width of the illuminated area is called *swath*. Finally, the satellite-to-target direction is called *slant range*.

In Figure 2 the standard acquisition scheme for a SAR sensor acquiring in the widely used Stripmap mode is shown. Less common acquisition modes are the ScanSAR and SpotlightSAR. The first, is based on the concept of a multi-beam antenna that can illuminate different sub-swath through different beams (Monti Guarnieri & Prati, 1996); by merging this sub-swath images is possible to generate a wider swath image than the one obtainable by the Stripmap mode (400 – 500 km). The increase in the acquisition area is contrasted by the loss in resolution, especially along the azimuth direction (Monti Guarnieri & Rocca, 1999). More accurate description of benefits and disadvantages of ScanSAR mode are included in Monti Guarnieri and Prati (1996), Moreira et al. (1996) and Holzner & Bamler (2002). The second mode uses a large real antenna to achieve a good signal to noise ratio focusing on a target of interest, obtaining a great increase in the resolution; on the other hand, the large antenna used have a small bandwidth that can guarantee the illumination of a limited area of the Earth surface (Belcher & Baker, 1996).

A further development of the acquisition modes of a SAR satellite is the TOPSAR mode, that overcomes the limitations imposed by the ScanSAR wide swath mode. During the acquisition, the antenna is steered along the track from backwards to forwards, so that every target on the ground is observed with the complete azimuth antenna pattern. The TOPS mode was firstly experimentally applied by the German X-band sensor TerraSAR-X (Meta et al., 2010) and then became the standard acquisition mode of the European C-band sensor Sentinel-1, launched in October 2014 (Yagüe-Martínez et al., 2016).

Each SAR sensor is designed to work at a specific wavelength, ranging from the shortest one, K_a, to the longest one, P (Figure 3). The letter codes for the various bands were originally selected arbitrarily to ensure military security during the early stages of development of the radar technology. Every sensor emits its signal at a specific central frequency (operating frequency) that defines the signal propagation and penetration features. For satellite applications, the three most commonly used bands are: C-band (4-8 GHz, ≈5.6 cm wavelength), X-band (8-12 GHz, ≈3.1 cm wavelength) and L-band (1-2 GHz, ≈23 cm wavelength).

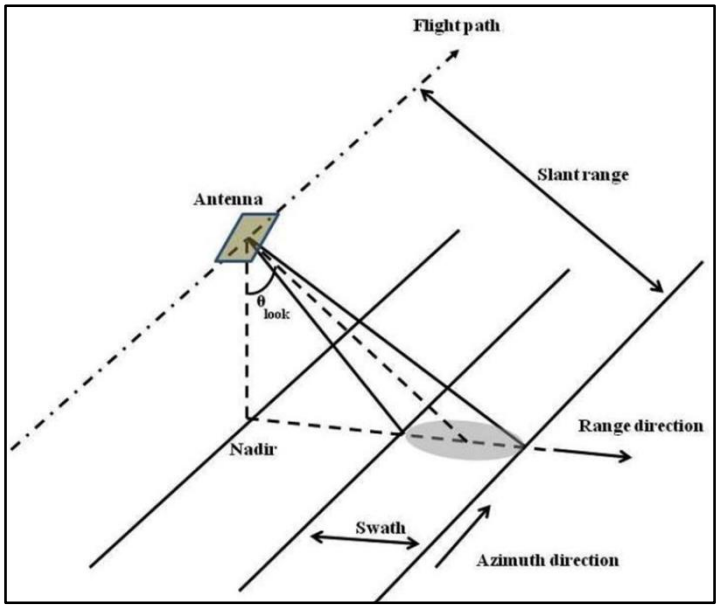

Figure 2 – Stripmap mode acquisition scheme. The elliptical grey area represents the footprint (from https://www.asf.alaska.edu /about-sar/sar-basics).

The satellites that usually carry the SAR sensor travel along a near-polar sun-synchronous orbit, inclined of a certain angle with respect of the Earth meridians at an altitude ranging from 500 to 800 km above ground surface. The sensor-to-target direction is called *Line Of Sight* (LOS), inclined of an angle θ (*off-nadir angle*) with respect to the vertical; this angle is an intrinsic characteristic of every sensor and varies between 23° to 45° (Figure 4A). A SAR satellite has two polar orbit directions: ascending, if the sensor moves from the south pole to the north, and descending, when the sensor moves on the second half of its orbit (from north towards south). During its movement, the SAR sensor always acquires to the right side of the track, thus observing the same scene from the East in the descending orbit and from the West when capturing images in ascending orbit (Figure 4B). The COSMO-SkyMed sensor has the possibility of acquiring to the left side for short period of time if specific requests are made, i.e. during environmental emergencies.

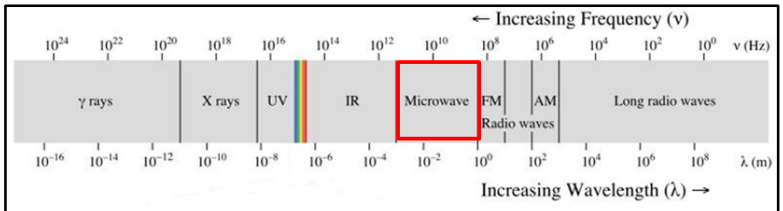

Band	Wavelenght (λ, cm)	Frequency (f, MHz)
K_a	0.75 – 1.1	40000 – 26500
K	1.1 – 1.67	26500 – 18000
K_u	1.67 – 2.4	18000 – 12500
X	2.4 – 3.75 CF 3.1	12500 – 8000
C	3.75 – 7.5 CF 5.6	8000 – 4000
S	7.5 – 15.0	4000 – 2000
L	15.0 – 30.0 CF 23.0	2000 – 1000
P	30.0 – 100.0	1000 - 300

Figure 3 - Electromagnetic spectrum. In red the wavelength range for the microwaves. The table shows the different bands composing the microwaves, in which the most common bands for satellite sensors are highlighted in yellow. CF, central frequency.

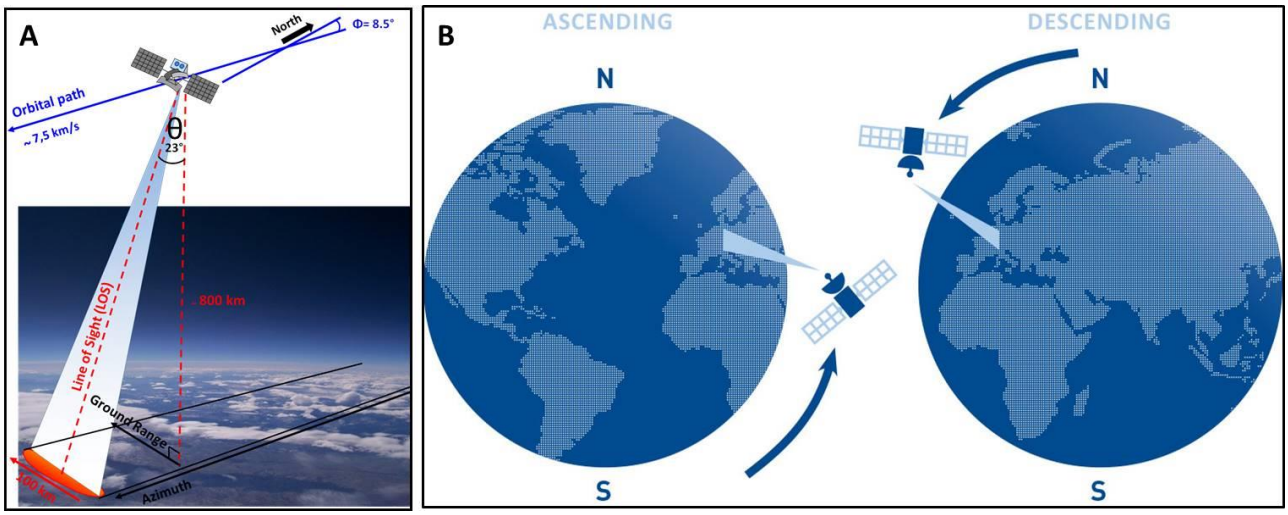

Figure 4 – SAR sensor acquisition geometry. A) ERS 1/2 satellite imaging geometry (from http://esrl.noaa.gov); B) Ascending and descending geometries for the Sentinel-1 satellite (from http://tre-altamira.com).

One of the most important characteristics of a SAR sensor is its capability of acquiring data on the same area in a certain time that is called *revisiting time*. The technological evolution of the satellites allowed to greatly reduce this time, passing from the 46 and 35 days of the first L- and C- band sensors (ALOS-1 and ERS 1/2) to the 6 days of the Sentinel-1 twin constellation (Figure 5). This parameter is fundamental not only for the temporal density of image acquired but also for the quality of the obtainable results; in fact, increasing the number the images in a certain time interval allows deriving high quality InSAR results because of the high redundancy of data (Hooper, 2008). Starting from the 1992, several satellite-based SAR sensors have been launched, providing images acquired at different wavelengths and that can be used for ground deformation monitoring (Figure 5).

Another fundamental feature is the ground resolution of the sensor that defines the dimension of the pixels of the SAR image. In fact, the applicability of a typology of SAR data to the monitoring of a specific environment highly depends on this parameter. The lowest ground resolution is obtained by the L-band sensors ALOS 1 and ALOS 2 whereas the highest is reached by the X-band sensors (1 m). The ground resolution of the C-band sensors varies between 30 m (Envisat) and 10 m (Sentinel-1 A&B). The L-band data, despite having the lowest ground resolution, are suited for environmental applications, such as land cover and land use monitoring (Longépé et al., 2011), forestry management (Shimada et al., 2014), oceanography (Karang & Nishio, 2011) and snow researches (Singh et al., 2014). This is possible because of the ground and vegetation penetration of the L-band; moreover, the quadra-polarization asset of the ALOS sensors signal allows studying landslide-related deformation where a high density of vegetation is present (Yonezawa et al., 2012). On the other hand, the X-band data are ideally suited for studies in urban areas, especially focusing on single building monitoring, thanks to their very high ground resolution (Bonano et al., 2013).

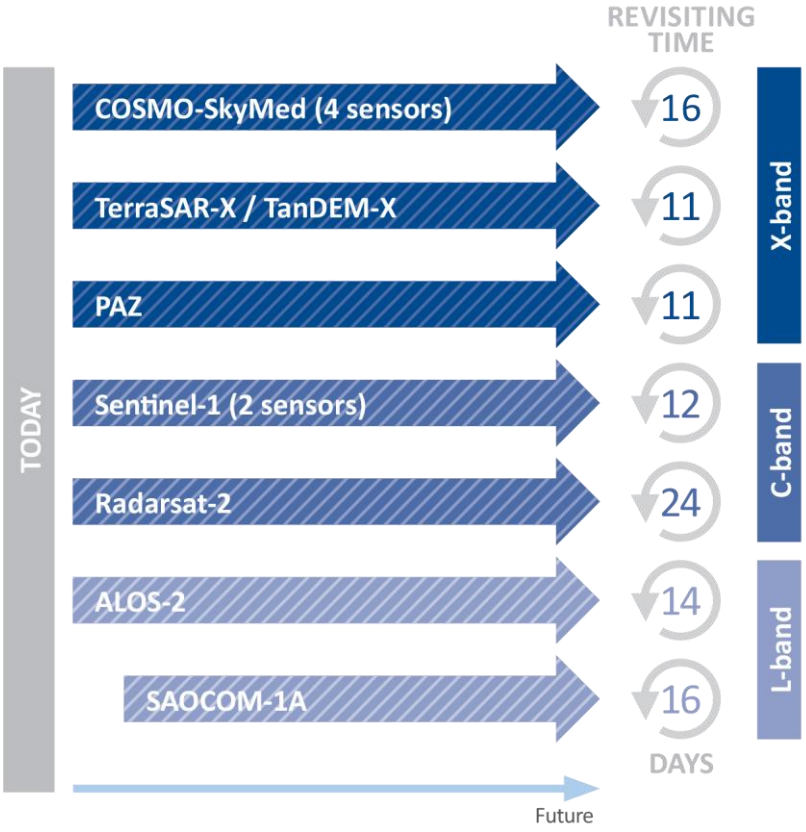

Figure 5 – Available satellites for interferometric applications (from http://tre-altamira.com). The revisiting time and ground resolution of each sensor is shown.

Distortions in radar images are frequent, especially when sensors illuminate target surfaces such as mountain slopes with high relief (i.e., surfaces with different angles). These distortions are clearly visible as effects on radar images, whose appearance and information can significantly vary. The most common, well-known effects in radar images are *Foreshortening*, *Shadowing* and *Layover* (Figure 6). As the terrain slope increases with respect to a flat horizontal surface (i.e. as the perpendicular to the terrain moves toward the LOS), ground resolution cell dimension in range increases. Thus, this terrain slope, facing the illumination of side-looking radar, is subject to a spatial distortion. This effect is called Foreshortening and it can be defined as a compression (shortening) of those slopes on the illuminated side of the beam. Shortened slopes appear bright-toned in the radar image. On the contrary, when the terrain slope is close to the radar off-nadir angle, the cell dimension becomes very large and all the details are lost. This happens when topographic surfaces on the opposite side of incoming beam generally are not illuminated and they suffer of Shadowing (dark-toned). The effect is more pronounced for sensors that use steeper incidence angles and for steeper slopes. In some situations, the terrain slope exceeds the radar off-nadir angle, and so the scatterers are imaged in reverse order and superimposed on the contribution coming from other areas. In other words, the electromagnetic beam reaches the top of the slope facing the illuminating front before it reaches the foot of the slope. As a consequence, the top of the slope is reflected first to the receiving antenna and seems to be closer to the radar, in the slant range direction, than the lower portion of the slope. This is called Layover effect and it is most pronounced in near range field and for sensors with smaller incidence angle.

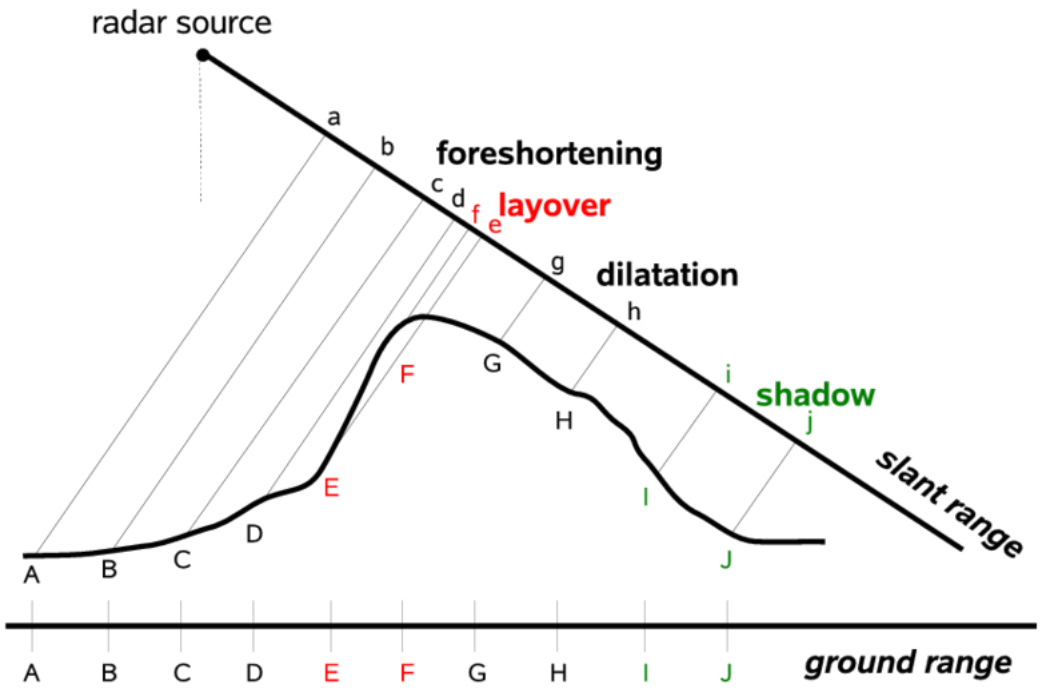

Figure 6 – SAR images distortions related to local topographic effects.

A SAR image is visualized using a grey scale levels because of the single frequency acquisition (Figure 7). Bright pixels correspond to strong reflecting objects (e.g. urban areas, exposed rocks, metallic structures) while dark pixels correspond to low backscattered radiation (e.g. water basin without waves, woods). Multiple object, with different reflectivity values, are found in the resolution cell of a SAR image. The registered echoes can add both constructively and destructively, creating a noise effect attributed to random interference between the coherent returns issued from the numerous scatterers present on the surface (Gagnon and Jouan, 1997). This effect is known as *speckle* and it is easily recognizable by a granular degradation of the image (salt and pepper visualization).

Figure 7 – SAR amplitude image acquired by the Sentinel-1 C-band satellite over Houston (Texas). Black pixels represent radar-absorbing surfaces (i.e. water) whereas white pixels indicate radar-reflective surfaces (i.e. rocks or buildings). All the surfaces with intermediate radar reflectance are represented in grey tones.

2.1 SAR interferometry – Fundamental laws

For the use of the phase signal included in each image pixel, a single SAR image is not useful. To obtain this information, at least one other image, acquired above the same area, is required to be "interfered" with the first image. This technique is called interferometry and the principle of using space-borne SAR systems as "interferometers" dates back to early 1970s (Richman, 1971). The conventional Synthetic Aperture Radar Interferometry (InSAR) deals with the pixel-by-pixel phase difference of two acquisitions, gathered at different times with slightly different looking angles. In particular, InSAR is the measurement of signal phase change of two or more SAR images over the same scene, acquired at two different times and/or slightly different locations (Bamler and Hartl, 1998).

The basic principles that regulates the conventional InSAR technique are briefly explained below. Firstly, considering a single pixel (P) on the ground, the sensor acquires a SAR image from a M position along its orbit, measuring a φ_M phase (1, Crosetto et al., 2016):

$$\phi_M = \phi_{GEOM-M} + \phi_{SCATT-M} = \frac{4\pi * MT}{\lambda} + \phi_{SCATT-M} \quad (1)$$

where MT is the sensor to target distance referred to the position M, φ_{SCATT} is the phase shift generated during the interaction between the radar signal and the target, the 4π is referred to the two-way path "sensor-target-sensor". Assuming that the sensor acquires a second image above the same area but from a different position (S) along the orbit, the phase φ_S can be calculated with equation (1), with the only difference that the sensor to target difference is referred to the position S (and to the distance ST). The phase difference between 2 images is then derived using (2, Crosetto et al., 2016):

$$\Delta\phi_{INT} = \phi_S - \phi_M = \frac{SP-MP}{\frac{\lambda}{4\pi}} + \phi_{SCATT-S} - \phi_{SCATT-M} \quad (2)$$

This equation allows deriving the interferometric phase for each pixel and is related to the distance difference SP-MP, which is necessary for extracting the interferometric Digital Elevation Model (DEM) and estimating the topography of the observed scene. This is true in the case of a not moving target; If the target moves from a position P to a position P', the second image is acquired from the satellite position S referred to the target to sensor distance SP'. In this case, the interferometric phase is given by (Crosetto et al., 2016):

$$\Delta\phi_{INT} = \phi_S - \phi_M = \frac{SP-MP}{\frac{\lambda}{4\pi}} + \frac{SP'-SP}{\frac{\lambda}{4\pi}} + \phi_{SCATT-S} - \phi_{SCATT-M} \quad (3)$$

where the first term is the component related to the topography (φ_{TOPO}) and the second term is the displacement phase component (φ_{DISP}) related to the movement of the target P between the two images acquired at the position M and S. The last 2 terms of the equation can be removed in the calculation, so obtaining that the interferometric phase is only dependent from the displacement and topographic components. The latter can be simulated (φ_{TOPO_SIMU}) if a DEM of the area of interest is available and then subtracted to the φ_{DISP} component; we derive the DInSAR phase in this way (4):

$$\Delta\phi_{D-INT} = \Delta\phi_{INT} - \phi_{TOPO\_SIMU} = \phi_{DISP} \quad (4)$$

This equation represents the fundamental principle that allows deriving the displacements from two SAR images acquired above the same area of interest (Massonet & Feigl, 1998; Hanssen, 2001). The equation (4) represents only a simplified version of a more comprehensive equation that includes other components (5):

$$\Delta\phi_{D-INT} = \phi_{DISP} + \phi_{TOPO_{RES}} + \phi_{ATM_S} - \phi_{ATM_M} + \phi_{ORB_S} - \phi_{ORB_M} + \phi_{NOISE} + 2k\pi \quad (5)$$

where:

- φ_{TOPO_RES} is the residual topographic error (RTE). This component represents an effect of the local topography that cannot be perfectly removed and that increases with the normal baseline (distance between the acquisition orbits of two SAR images, usually below 1km) and the elevation error of the DEM (Ferretti et al., 2000);
- φ_{ATM} is the atmospheric phase component at the time of the two acquisitions (S and M). The physical characteristics of the atmosphere, especially if the troposphere, can impact the performance of spaceborne SAR systems. In fact, the signals emitted by the sensor propagate through the spatially

inhomogeneous atmosphere, which has a slightly higher index of refraction than free space, producing delays in the signals and reduction of the velocity of the microwaves that contaminate the observations (Zebker et al., 1997);

- φ_{ORB} is the phase component due to the orbital errors of each image that could affect the positions M and S. Small variation of the cross-track and along track components of the orbit during the SAR acquisition can generate artifacts in the derived interferograms, producing orbital fringes not related to a real ground displacement (Shirzaei & Walter, 2011);

- φ_{NOISE} is the noise component of the phase. It can be related to speckle effect that are generally considered undesirable since they damage the radiometric resolution of the images (Achim et al., 2003) or can be associated to the temporal and geometric decorrelation of the illuminated surfaces and so of the received signal (Hanssen, 2001). For example, in vegetated areas the plants growth can produce decorrelation, reducing the coherence of the image,

- k is an integer value called *phase ambiguity* that is a result of the wrapped nature of the interferometric phase that is bounded in the range $-\pi$, $+\pi$ and that has to be unwrapped to determine the displacement occurred between two SAR images (Ghiglia & Pritt, 1998).

An interferogram is formed by the complex product of the two SAR images (called the *master* and the *slave*) and its phase, which contains all the information and errors contained the equation (5). The main purpose of an interferometric process is to separate the different components, extracting only the one related to the displacements and removing or minimizing the others.

2.2 Differential interferometry (DInSAR)

The retrieval of the ground displacements that occurred between two different SAR acquisitions can be achieved by Differential InSAR (DInSAR) within the repeat-pass interferometry method (Rosen et al., 2000). Since the first description of the technique, which was based on L-band SEASAT SAR data (Gabriel et al., 1989), the great potential of DInSAR for land deformation applications has been recognized. Of major interest were the wide areas covered by each image, the global coverage and the repeat observation capabilities, associated with the intrinsic high metric quality of the DInSAR observations (Crosetto et al., 2005).

In Figure 8 the process of deriving deformation measurements from SAR images is shown. In the time interval between the acquisition of the two images, the target on the ground changes its relative position (in this case for a tectonic movement) and the phase component related to the displacement varies. For every image pixel, the displacement occurred, ranging between $-\pi$ and $+\pi$, is then calculated and the interferogram derived. The displacement in an interferogram is usually highlighted by a fringe of movement (equal to ±3.14 cm). Wherever fringes occur, it is possible to calculate deformation by calculating the number of fringes and multiplying them by half of the wavelength. These fringes can be observed only where the image is coherent enough; for being coherent an image has to maintain its surface electromagnetic characteristics between the two images used to derive the interferogram (Hanssen, 2001). If the ground surface loses its electromagnetic "stability" (i.e. in agricultural or wooded areas), the noise level of the image increases due to the temporal decorrelation of the signal and the coherence consequently decreases; in this case, parts or the totality of the image appear to be speckled

The coherence of an interferogram is affected by other factors: the time between two images (temporal baseline, longer time interval means lower level of coherence), the distance between the orbits of the two images (normal baseline, higher distance means lower coherence), the local topography (the presence of

steep slopes, oriented parallel to the sensor orbit, reduce the coherence) and the terrain properties (humidity reduce the coherence). Coherence is usually measured by an index ranging from 0, completely decorrelation, to 1, completely coherent.

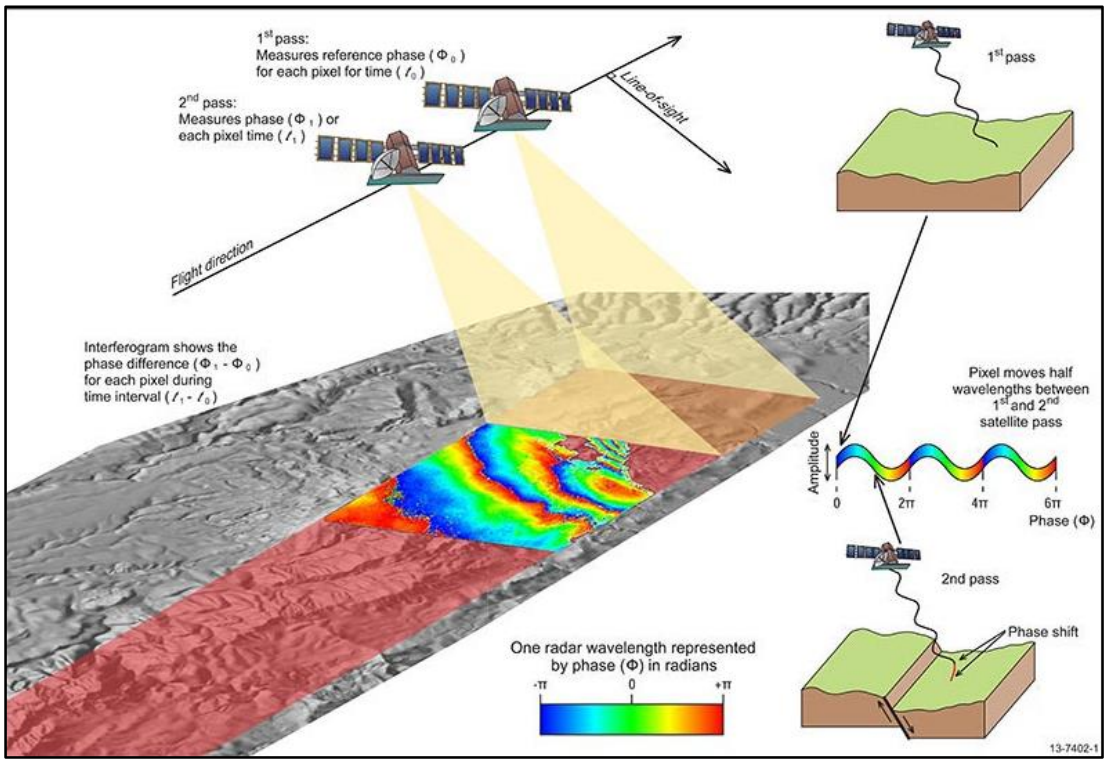

Figure 8 – Schematic picture showing basic principle of DInSAR and the relationship between ground displacement and signal phase shift (from http://www.ga.gov.au/scientific-topics).

As shown by equation (5), the level of noise, the atmospheric effects and the geometric distortions have to be compensated, minimized and removed throughout the application to the SLC images of specific filters (i.e. Goldstein filter for atmospheric removal; Goldstein and Werner, 1998). These image correction procedures allow obtaining an interferogram in which the phase variation is largely due to the displacement occurred between the two SAR acquisitions. This is true only for very short temporal intervals and represent almost ideal conditions; in a common situation, all the sources of noise cannot be totally removed.

Despite these limitations, DInSAR has been widely used to detect, map and quantify surface deformations with centimeter precision over large, contiguous areas along the sensor's line-of-sight direction (Figure 9). In particular, the technique represents an ideal solution for monitoring:

- subsidence (i.e. Ferretti et al., 2000; Mora et al., 2001; Crosetto et al. 2003; Tomás et al., 2010; Sarychikhina et al., 2011);
- tectonic motions and earthquake-induced deformations (i.e. Stramondo et al.; 2002; Hernandez et al., 2004; Atzori et al., 2009; Chini et al., 2010; Solari et al., 2016);
- landslides (i.e. Refice et al., 2001; Nagler et al., 2002; Ferretti et al., 2005; Peyret et al., 2008; Jebur et al., 2015);

- mining activity (i.e. Spreckels et al., 2001; Chang et al., 2005; Herrera et al., 2007; Przyłucka et al., 2015);
- volcanic activity (i.e. Avallone et al., 1999; Pritchard & Simons, 2004; Lagios et al., 2005; Papageorgiu et al., 2012; Del Negro et al., 2013).

In the last two decades, space-borne DInSAR techniques have improved their capability in a wide range of application fields. Nowadays this technique became a consolidates and well-established measurement tool that has become the starting base of several projects and scientific studies. Moreover, in the last years, free software and web platforms (i.e. SNAP software, developed by ESA) grew up to allow new users to apply the DInSAR approach, expanding the scientific community.

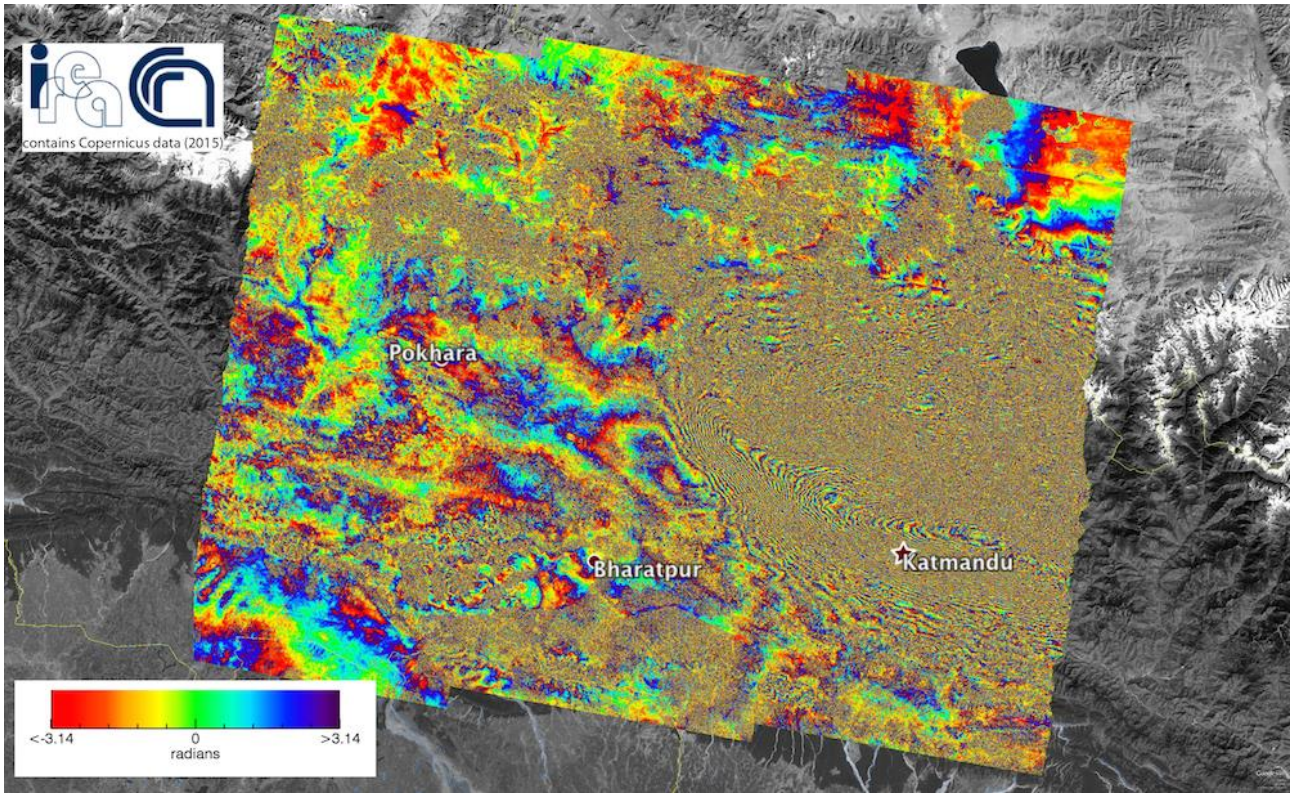

Figure 9 – Example of DInSAR-derived deformation maps. Earthquake-induced deformation derived from Sentinel 1-A carried out by IREA-CNR.

2.3 Persistent Scatterers Interferometry (PSI)

To overcome the main limitations of the single-pair interferometry (difficult atmospheric and decorrelation phenomena removal), a new technique, exploiting long stack of interferograms, was developed starting from the early 2000s. This technique is called Persistent Scatterers Interferometry and it includes numerous approaches, developed by different scientific groups worldwide, for deriving the multi-temporal behavior of the ground movements in an area.

PSI hence represents a specific class of DInSAR, which exploits multiple SAR images to separate the phase component related to the displacement (φ_{DISP}) from all the other noise sources (see equation 5) in a more reliable way than the DInSAR technique, throughout the exploitation of appropriate algorithms of analysis.

The number of images that construct the data stack to be exploited in a PSI analysis depends on the revisiting time of the sensor, on the data acquisition policy (a regular acquisition plan is not possible for all the world and for all the satellites) and on the orbital tube that is the set of distances between the multiple SAR images (Rocca et al., 2004). Considering these limitations, a minimum of 20 images is needed to perform a reliable analysis on C-band data; this number decreases if X band data are used. In fact, the shorter wavelength and higher resolution allow obtaining consistent results with a shorter data stack (Bovenga et al., 2012). Anyhow, if the number of images increases, the estimation of the deformation values and of the time series will greatly improve (Crosetto et al., 2016).

The PSI approach cannot derive measurement points from every Earth surface; it is able to derive the displacements only from the available Persistent Scatterers (PS). These points represent surfaces or objects with that reveals stable amplitude properties and coherent signal phase within a resolution cell, throughout all of the SAR images within a data stack. PS point-wise targets exhibit reduced temporal decorrelation due to their high electromagnetic reflectivity and their coherent and stable scattering behavior. Having a stable radar signature, PS are only slightly affected by decorrelation effects and the backscattered radar signal is much higher than the noise of the sensor (Ferretti et al., 2001). PS are abundant over urban areas, where buildings, man-made metallic structures and roads are found, in rocky areas or where isolated buildings or metallic elements are found (Figure 10). The PS density is very low in vegetated, forested, agricultural or low-reflectivity areas and in steep slopes facing the radar sensor (shadowing effect). Snow coverage, construction work and roads re-pavement can lead to the complete or partial loss of PS (Crosetto et al., 2016). The exploitation of PSI data allows remarkably increasing the number of measurement points in an area, at a relatively low cost, compared to GPS (Global Positioning System) surveys, for example. On the other hand, the position of a PS cannot be known before the processing of the data; this can be critical for the study of targets with small spatial extent, because they can be under sampled or not sampled at all. This fact can be partially mitigated by using X-band very high-resolution data (Crosetto et al., 2010). Another crucial point is the difficulty to assign a PS to a specific part of the analyzed object, i.e. a group of PS referred to a building. This fact represents a limitation, especially when working at building scale. Some experiments where proposed by Auer et al., 2011 to improve the understanding of multiple reflections of the radar signal on buildings and so the interpretation of PSI data.

The density of PS in an area can be artificially improved by deploying Corner Reflectors (CR). These metallic structure, installed in situ, provide an almost perfect reflection of the SAR signal, resulting in an improvement of the coherence of the ground surface where they are used and guaranteeing the estimation of the deformation (Sarabandi & Chiu, 1996). The CR can be permanently and strategically installed in vegetated areas, especially where landslide movements have to be monitored, in order to provide deformation measurements where it was not possible before. Many examples of their application for ground movements

monitoring can be found in bibliography, i.e. Xia et al., 2002; Ferretti et al., 2007; Fan et al., 2010; Crosetto et al., 2013; North et al., 2017; Aslan et al., 2020)

PSI deformation rates measurement are 1D, projected along the LOS of the sensor and so estimating only one component of the deformation (Figure 11). The displacement vector measured in this way is so underestimating the real displacement vector. A way to obtain a 2D reconstruction of this vector is the decomposition of the LOS vector into the vertical and east-to-west horizontal components of deformation; this is possible only if data acquired in both orbits and processed separately are available (Ferretti et al., 2007 - Figure 11). Each measurement point is characterized by a value of velocity (usually in mm/yr of cm/yr) estimated on the basis of a linear or non-linear model, depending on the type of deformation (Kempes, 2006). Moreover, the velocity value is always referred to a reference point (one for all the data stack), assumed to be completely stable and characterized by a very high value of coherence (> 0.95). The velocity will have a sign, depending on the ground movement in respect of the LOS of the satellite: positive velocities indicate movements through the sensor (uplift or movement along slope), negative velocities indicate movements away from the sensor (subsidence or movement along slope).

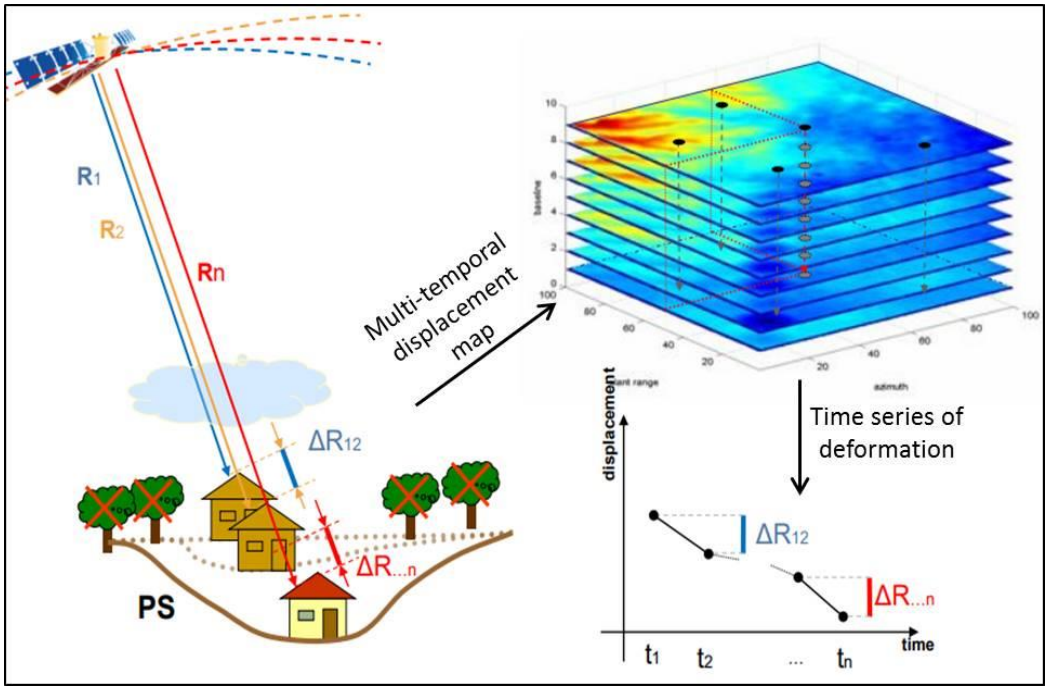

Figure 10 – Basic principles of the PSI technique. The satellite acquires multiple n images above the same moving area (R_n indicates the motion of the target). At every new acquisition of the sensor a new interferogram is formed between the last image and the new one. The displacement maps are then derived from the interferogram and stacked together, composing the final product. For every coherent pixel (i.e. PS) of the displacement map the time series of deformation is finally derived.

Each PS point contains also the information referred to the cumulated displacement of every acquisition, allowing the reconstruction of the deformation history of a point throughout the analysis of the so derived time series of deformation. These series are fundamental to study the kinematic of a phenomenon, highlighting accelerations, decelerations, hyperbolic trends (typical of pre-failure) and correlate these trend changes with external and causative factors (Cigna et al., 2011). The time series of deformation are a zero-redundancy product, in fact, for every acquisition only one data of displacement is available; for this reason, they are particularly sensitive to the phase noise. This is evident especially for C-band data, while X-band data

show a remarkable quality improvement of the time series (Crosetto et al., 2010). The deformation time series can be affected also by anomalous trend not related to real ground motions that can be easily detected because affecting the whole dataset. They can be due to (Notti et al., 2015): long term geological processes, errors in the atmosphere correction during the data processing, uncompensated phase ramps, reference point not stable, thermal effects on the target. The latter is particularly important in urban areas (buildings and bridges). Due to the high sensitivity of the interferometric phase, the thermal expansion of the materials caused by temperature variations can produce distortions in the deformation time series, especially when the PSI dataset is short and when very high-resolution X-band data are used (Crosetto et al., 2015). The effect of temperature in urban areas is not usually modeled during the data processing but is possible to estimate the thermal expansion parameters (deriving thermal maps) for selected areas, if a high precision of the time series is needed for a building scale analysis (Monserrat et al., 2011).

One big limitation of the PSI technique is its impossibility of capturing "fast" deformations due to the intrinsic wrapped nature of the phase. Considering the fundamental equations that regulate the SAR interferometry, if the deformation phase between two acquisitions is bigger than π, the real deformation cannot be retrieved unambiguously (Crosetto et al., 2016). This limit corresponds to a maximum differential deformation between two acquisitions of λ/4 over the revisit interval (Ferretti et al., 2007). Considering the wavelength and the revisiting time, the maximum differential deformation rate measurable for the most used SAR sensor is: 14.7 cm/yr for ERS 1/2 and Envisat, 21.2 cm/yr for RADARSAT-2, 25.7 cm/yr for TerraSAR-X, 35.3 for COSMO-SkyMed, 42.6 cm/yr for Sentinel-1 (A&B) and 46.8 cm/yr for ALOS-2.

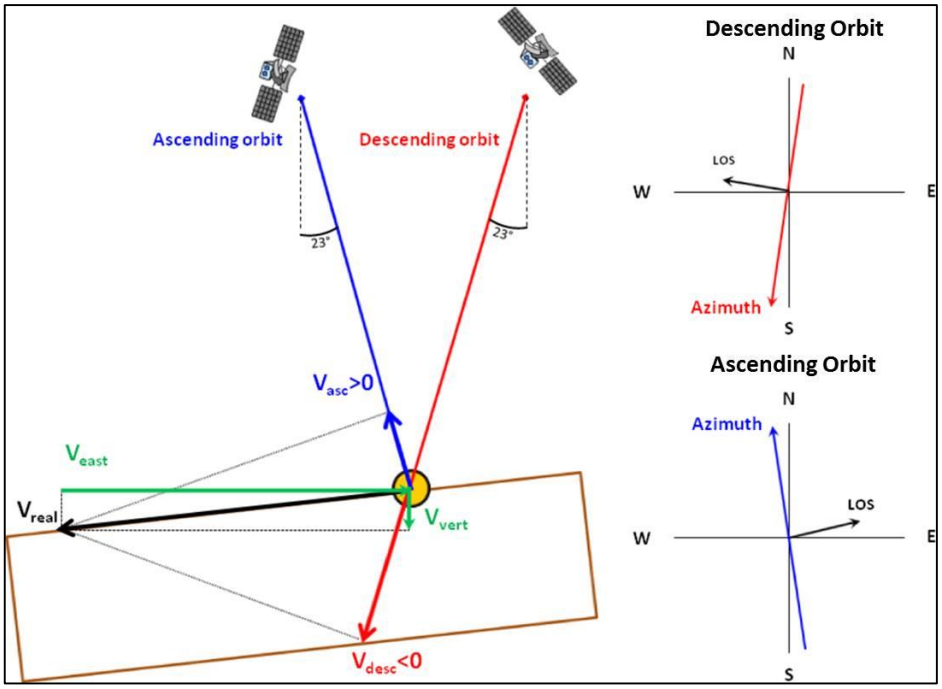

Figure 11 - Extraction of vertical and horizontal (E-W) deformation components, projecting the ascending and descending acquisition geometries (from Tofani et al., 2013).

After almost 20 years of advance and improvement of the PSI technique, at least 15 different algorithms were developed by private companies or research entities (Table 1). The first PSI approach proposed is the PSInSAR (Ferretti et al., 2000, 2001), developed by a spin-off of the University of Milano that is now a private

company, TRE-Telerilevamento Europa. Few years later, the SBAS algorithm (Berardino et al., 2002) was developed by the CNR-IREA of Naples. These two pioneering algorithms, constructed on different strategies, represent the starting points for the evolution end development of the PSI analyses. In the next years, several approaches that modify the PSInSAR or the SBAS techniques were proposed, such as: IPTA, developed by Swiss company Gamma Remote Sensing (Werner et al., 2003), the STaMPS method developed by Hooper et al. (2004) at the Stanford University. The latter, represents one of the first examples of freely available software, for non-commercial use, for SAR images PSI processing. Another technological step forward was made in 2011, when the SqueeSAR algorithm was firstly presented (Ferretti et al., 2011).

In the following section, a brief description of each one of these methods will be illustrated:

- PSInSAR; this technique analyzes long stacks of co-registered SAR images to identify point-wise targets (PS, Permanent Scatterers) within the ground resolution cell which can be natural or man-made and have stable radiometric characteristics during the entire acquisition interval. Phase information backscattered from these coherent points is used to derive the ground displacement and the temporal evolution of the movement. The PS approach adopts essentially a model-based, temporal unwrapping strategy that necessitates to know a priori the characteristics of the motions to be analyzed. In general, the average linear displacement velocity and the DEM error are considered as the two major parameters of 2D linear regression of the wrapped phases (Ferretti et al., 2001);

- SqueeSAR; this approach represents the evolution of the PSInSAR technique, in which the displacement information is retrieved from the Distributed Scatterers (DS), measurements points referred to partially coherent areas and not to single coherent objects (buildings, man-made structures, etc…) as the standard PSInSAR. The SqueeSAR algorithm was developed to process the signals reflected from these low-reflectivity homogeneous areas, but it also incorporates PS data, hence no information is loss and the measurement accuracy is improved (Ferretti et al., 2011).

- SBAS; the key feature of this algorithm's chain is the selection of the SAR images that will be used to generate the interferograms; this is done by choosing only those data pairs characterized by short temporal and perpendicular baselines (Berardino et al., 2002). This procedure allows for a minimization of the noise effects thus maximizing the number of coherent pixels in the generated interferograms. Independent acquisition datasets, separated by large baselines, are properly linked by applying the Singular Value Decomposition (SVD) method, to retrieve deformation time series and velocity maps. The SBAS algorithm is also capable of producing results at two different scales (Lanari et al., 2004): a regional-scale, for investigating diffused deformation phenomena at a medium spatial resolution (the cell resolution ranges from 100 × 100 m to 30 × 30 m); and a local scale, which exploits the full resolution interferograms (benefiting from the high-resolution capability of the SAR satellite system) for generating products ideally suited for building analysis.

- CPS; this approach includes three main processing blocks. In the first one, a set of correctly unwrapped and temporally ordered phases are derived, which are computed on Persistent Scatterers (PSs). The key element of this block is given by the so-called Cousin PSs (CPSs), which are PSs characterized by a moderate spatial phase variation that ensures a correct phase unwrapping. In the second block, the above phases are used to estimate the atmospheric phase screen. The third block is used to derive the PS deformation velocity and time series. Its key tool is a 2+1D phase unwrapping using a set of redundant interferograms (Devanthéry et al., 2014).

PSI method	Main references
PSInSAR (Permanent Scatterers Interferometry)	Ferretti et al., 2000, 2001
SBAS (Small Baseline Subset)	Berardino et al., 2002
CPT (Coherent Pixels Technique)	Mora et al., 2003; Blanco et al., 2006
Modified SBAS	Schmidt & Burgmann, 2003
IPTA (Interferometric Point Target Analysis)	Werner et al., 2003
SPN (Stable Point Network)	Duro et al., 2003; Crosetto et al., 2008
StaMPS (Stanford Method for Persistent Scatterers)	Hooper et al. 2004
STUN (Spatio-Temporal Unwrapping Network)	Kampes, 2006;
PSP (Persistent Scatterers Pairs)	Constantini et al., 2008, 2014
DePSI (Delft Persistent Scatterer Interferometry)	Ketelaar, 2009
SqueeSAR	Ferretti et al., 2011
WAP (Wide Area Product)	Adam et al., 2011
SARproZ	Perissin & Wang, 2012
MInTS (Multiscale InSAR Time Series)	Hetland et al., 2012
Distributed Scatterers approach	Goel & Adam, 2014
Modified SqueeSAR	Lv et al., 2014
CPS (Cousin PS)	Devanthéry et al., 2014

Table 1 – List of the main PSI approaches in chronological order.

3. PSI data for geohazards monitoring

The results retrieved from satellite InSAR make it a unique instrument for ground displacement analysis, which contributes to the portfolio of technologies of traditional monitoring techniques and can be used in many diverse applications (Ferretti, 2014). PSI is often seen as a "new technology" for surface deformation monitoring and its potential is commonly underestimated, even within the scientific community (Ferretti et al., 2015). By the way, the successful application of the PSI algorithms for the detection of ground motions at different scales, ranging from buildings to entire regions or nations, has shown that the interferometric approach is a mature technology, based on robust algorithms that can pave the way to new applications (Ferretti et al., 2015).

PSI is defined as a multi-scale tool that offers the ability to detect ground displacements over wide areas (i.e. 10000 km^2 for a ERS1/2 and Envisat StripMap frame or 62500 km^2 for a Sentinel-1 Interferometric Wide Swath frame) with relatively high spatial density of measures. At the same time, the technique can be efficaciously exploited for monitoring single infrastructures or small areal extent phenomena thanks to its high sensitivity to small deformations, moreover when using X-band data. The availability of these type of

data since 2007 has significantly increased the application potential of PSI (Crosetto et al., 2016). A unique aspect of PSI is the possibility to construct large archives of SAR images, going back in time of many years before the phenomenon occurrence. PSI also enables to potentially reduce the amount of ground-based observations needed to analyze a geohazard and so the personnel time and costs.

In addition, the Sentinel-1 launch in 2014 represent a fundamental passage between multi-purpose SAR sensors (even with military functions) to a fully free civilian satellite specifically designed for surface deformation monitoring over large areas (Torres et al., 2012). Apart from Sentinel-1, the number of satellite data sources is continuously increasing (at least 8 satellites are operative at the moment), guaranteeing to design redundant acquisition schemes in which the possible failure of one of the systems chosen cannot compromises the monitoring strategy (Ferretti et al., 2015).

All these features can be extremely useful in characterizing and addressing hazardous areas over hundreds or thousands of square kilometers, allowing Civil Protection Authorities (CPA) to evaluate different scenarios and to plan specific actions based on homogeneous and reliable measurements. The technological evolution reached by the PSI algorithm and the data processing and storage capabilities of the cloud computing, added to the SAR sensors temporal and spatial resolution, allow thinking and designing a satellite-based early warning system that cover a region.

In the following section, a general review of PSI approaches applied to monitor different geohazards (landslide, subsidence, tectonic and volcanic motions) is proposed, as well as a brief overview on the regional and national monitoring systems based on InSAR data.

3.1 Landslides

Spaceborne SAR sensors are usually used for the detection of unstable landslide prone and affected areas, and for the assessment of the long-term behavior of the detected phenomena. The multi-temporal InSAR (MT-InSAR) analysis allows deriving useful information on the dynamics and behavior of mass movements (Hilley et al., 2004; Strozzi et al., 2005) and can be successfully exploited to improve or create Landslide Inventories Maps (LIM), and updating the state of activity of already mapped phenomena (Farina et al., 2006; Singhroy et al., 2009; Hölbling et al., 2012). The scale of the analysis ranges between 1:250000 to 1:5000 (Fell et al., 2008); this is true not only for landslides but for all the different geohazards.

The main limitation to the definition of an InSAR-based strategy for landslide monitoring is related to the maximum displacement detectable between two SAR images. As stated in Chapter 2.3 Persistent Scatterers Interferometry (PSI)" this intrinsic threshold of the InSAR approach depends on the wavelength of the SAR sensor and to the revisiting time of the satellite above a certain target. For this reason, only landslides classified as "extremely slow" or "very slow" can be detected; their definition is based on the classification proposed in 1996 by Cruden and Varnes in which the "extremely slow" landslides register velocity below 16 mm/yr, while the "very slow" landslides show velocity below 1.6 m/yr. Landslide characterized by velocities higher than these thresholds cannot be detected because of the impossibility of completely and coherently unwrap the phase signal due to the ground deformation.

For the abovementioned limitations, intrinsically fast-moving landslides (e.g. rockfalls, topples, debris flows and rock avalanches) cannot be detected or their movement can be underestimated because of phase unwrapping errors (Cigna et al., 2011). Regarding rockfalls, the PSI data have been successfully used to detect precursors of the landslide on top of the rock slope (Frodella et al., 2016). Rotational and translational slides can be profitably monitored by means of the PSI technique (i.e. Notti et al., 2010; Bianchini et al., 2015).

Regarding flow-like landslides, a distinction depending on the involved material has to be made: rock flows, characterized by slow movements of the entire mass or of portions regularly distributed in the dislocated mass without a well-defined slip surface can be effectively monitored with the MT-InSAR approach, moreover because of the high reflectivity of the rocky outcrops (Kenyi & Kaufmann, 2003). Earth flows can be detected only if the landslide mass has low deformation rates and so has a low water content that cannot lead to the fluidification of the moving material (Greif & Vlcko, 2012). Debris flows, that usually register very high velocities, cannot be monitored by means of the PSI technique. Spreads can be partially analyzed by the satellite sensors, since only the sub-vertical component of the motion can be measured, related to the sinking of the upper coherent layers and induced by the lateral or sub-horizontal spreading of the lower fine-grained layers (Sato & Une, 2016). Lateral spreads due to liquefaction cannot be monitored by satellite interferometry because of their rapid occurrence.

The choice of the best radar data stack for monitoring a landslide has to be taken depending on two factors: orientation of the slope and land cover. The first parameter is fundamental for knowing a priori if there could be geometrical errors induced by the slope orientation (foreshortening, shadowing, etc…); the optimal choice is using data provided by both satellite orbits (ascending and descending), in this way it is possible to compare the data and improve the "radar interpretation" of the data (Farina et al., 2007). The second parameter has a crucial importance for deciding which band length is more suitable for a PSI analysis above the area of interest. Overall, few considerations can be made on the applicability of each band for landslide monitoring:

- C-band satellites cover large areas and are ideally suited for regional analysis at medium resolution exploiting very large databases of images (data stacks that start in 1992 with the ERS 1/2 data) and for the "back monitoring" of very slow- moving landslides (Cigna et al., 2011);
- X-band sensors, thanks to their temporal and spatial resolution, are ideally suited for building-scale analysis in urban areas affected by landslide movements (Notti et al., 2010). Moreover, exploiting not the phase but the amplitude component of the radar signal of X-band data, is possible to derive the deformation field induced by the landslide exploiting the Rapid Motion Technique (RMT, Raspini et al. 2015; Solari et al., 2017c). This approach can be used in case of displacements exceeding the phase unwrapping threshold;
- L-band data are useful in case of landslides affecting densely vegetated areas, thanks to the high penetration coefficient of the radar signal (Jebur et al., 2015); moreover, because of the long wavelength, it is possible to detect faster landslides (in terms of displacement rates) than the other two bands (Strozzi et al., 2005), reducing the decorrelation phenomena.

In summary, the main applications of PSI in landslide practices are:

- detection of slow moving landslides, reconstructing the historical deformation field of the event and combining the PSI-derived information with ground data and ground-based monitoring systems;
- landslide mapping at basin to regional scale, providing an update of preexistent LIMs;
- define the main components of the movement and the vector of displacement, providing useful information for the reconstruction, throughout a back-analysis process, of the original slope geometry. This can be made also exploiting interferometry-derived DEMs (Digital Elevation Models);
- define the triggering factor of the landslide by comparing rainfall data with the displacement time series;

- refinement of susceptibility models using the PSI data to improve the prediction reliability of the susceptibility maps;
- quantify the impact of landslides on a territory, deriving impact assessment maps that can be used as input for more sophisticated hazard and risk analysis;
- asses building damage and derive fragility curves for each building.

3.2 Subsidence

Land subsidence detection is one of the most common application of the PSI technique because of two main reasons: firstly, it is a phenomenon that usually involve urban areas, so allowing to obtain reliable results with a dense measurement grid (thousands of points for km^2), secondly, it is related to a mainly vertical component of the ground motion. The latter, simplifies a lot the PSI data interpretation, allowing to use only one orbit, not necessitating of post-processing analysis (i.e. projection of the LOS data in the slope direction or decomposition of the LOS vector into the vertical and horizontal components (see Chapter 2.3 Persistent Scatterers Interferometry (PSI)"). In the case of sinkhole-related subsidence this simplification can be not true, because of the presence of a relevant horizontal component, especially a certain period before the ground collapse occurrence (Jones & Blom, 2014). Moreover, the monitoring of surface motions related to ground collapses can be difficult with the PSI technique because of the high displacements rates sometimes recorded before the failure, near the $\lambda/4$ limit of the PSI approach, thus generating decorrelation phenomena. In this case, the classical DInSAR approach is preferable (Rucker et al., 2013).

The term land subsidence usually refers both to a gradual, gentle down-warping and to a sudden sinking of the Earth's surface (Galloway & Burbey, 2011). Subsidence can be triggered by natural or anthropogenic factors. Among the natural causes, it is worth to remember long periods of drought, dissolution of evaporite rocks below a sedimentary superficial layer, isostatic adjustments, long-term natural compaction of clayey sediments and peat oxidation in organic soils. Common causes of land subsidence from human activity are collapse of underground mines or cavities, tunneling, drainage of organic soils, hydro-compaction for extensive irrigation, rapid urbanization, load imposition (moreover for recent urban sprawl), drainage of reclamations or marshlands and backfill compaction in urban areas. Anyway, the most common human factor is the water-use practices; water overexploitation is recognized as one of the most important anthropogenic causes of subsidence (Hu et al., 2004). In addition, the extraction of deep fluids (water, oil, natural gas) is another human activity that can trigger land subsidence with huge areal extent (Galloway & Burbey, 2011).

Starting from the end of the nineteens, the D-InSAR and then the PSI approaches were exploited to detect land subsidence in urban and peri-urban areas all around the world. The scale of analysis depends on the type of phenomenon to be analyzed, large subsidence bowls, caused by water overexploitation are usually examined at small scale, focusing more on the general distribution of the displacements. On the other hand, building scale analyses are chosen when local ground lowering is found, caused by geological or anthropogenic factors (presence of high compressibility and organic layers, recent urbanization, cavities collapse, etc…).

3.3 Volcanic activity and tectonic motions

For seismic faults and volcanic motions monitoring a very high precision is usually required, because ground deformations can be extremely slow (Massonet & Feigl, 1998). This precision allows detecting more accurate displacement information and so deriving better fault dynamic models, improving the evaluation of seismic hazard. PSI data can be really useful in this context because of the density of measurements (orders of magnitude greater than the GPS) and for their higher vertical precision than that of a GPS network (Ferretti et al., 2006). Especially in volcanic environments, where the height changes abruptly, leading to intense atmosphere variations, thus representing a major limitation for the application of a "classical" two-interferograms approach, the PSI technique has proven to be reliable in estimating and removing the atmospheric phase delay that can cause misinterpretation errors (Bonforte et al., 2011). For these reasons, the PSI approach was chosen by several authors to analyze and monitor ground deformation related to active or quiescent volcanic systems or to faults activity.

3.4 Building and infrastructures

The PSI approach is also commonly used for the monitoring of the structural stability of single buildings or main infrastructures (e.g. bridges, pipelines) and of elements of the cultural heritage. This application is possible thank to the high number of PS point obtainable from a man-made structure, especially when the data processing is dedicated, and the SAR images used are acquired by X-band sensors.

Regarding the structural monitoring of buildings and infrastructures, Sousa & Bastos (2013) demonstrated the potential of MT-InSAR technique for detection of the deformation registered starting from 1995 of a bridge, crossing the Douro River in Northern Portugal, that collapsed in March 2001, killing 59 people. The satellite data confirmed the existence of high deformation rates in the sector of the future bridge collapse. Lazecký et al. (2014) proposed a multi-temporal monitoring, exploiting both C- and X-band SAR images, of a sector of a main Czech highway recently built on an undermined area affected by severe ground subsidence and fissuring. Bianchini et al. (2015) developed a methodology for assessing the stability of buildings affected by landslide phenomena based on two parameters derived on the basis of the PSI-derived deformation rates (maximum differential settlement and angular distortion). Huang et al. (2017) focused their analysis, exploiting Sentinel-1 C-band data, on determining the health of a high-speed railway bridge that crosses the Yangtze River in China; moreover, longitudinal profiles were used to defines the direct correlation between temperature and recorded displacements variations in the investigated time period. Another important application of PSI for infrastructural monitoring is the stability of artificial dams, that can register deformations connected to the water pressure, to bad design problems or to the compaction of the constructive materials (earth dams); in this case, the PSI data are extremely useful for preventing possible collapses of the structures (e.g. Wang et al., 2011; Tomás et al., 2013; Di Martire et al., 2014).

The monitoring of cultural heritage elements it is another common research topic. Tomás et al. (2012) analyzed the general stability of a gothic church (Santas Justa and Rufina) in the historical city center of Orihuela (Alicante Province, Spain), comparing PSI-derived deformation maps, piezometric level decrease, geological asset (presence of compressible layers) and the structure design of the church with the detected damage. Tapete et al. (2012) verified the possible application of PSI-derived C-band products for monitoring different archeological site in the center of Rome (Roman Forum, Palatino and Oppio Hills), obtaining reliable results confirmed by site evidences. Alberti et al. (2017) exploited the SqueeSAR algorithm to verify the stability of the stone monuments of the archeological UNESCO heritage of Petra in Jordan, in a non-urban environment, challenging for this type of analysis that anyway gave reliable results, confirmed by in situ

geotechnical data. Cigna & Tapete (2017) catalogued and assessed the availability of satellite-derived ground motion information from multi-temporal InSAR and Persistent Scatterers (PS) techniques for several European UNESCO sites. This work, in the framework of the PROTHEGO project, represent a valuable overview of all the open access data available and a literature review of preexistent researches, providing the coverage and the gaps of PSI data for each of the European World Heritage List.

3.5 Regional and national scale applications

The maturity of the interferometric algorithms coupled with the increasing computational power of personal computers allow rethinking the scale of analysis of the PSI approach. In fact, in recent years, projects and few applications aiming at exploiting PSI data at regional or national scale grew up, raising this technique to a new level in which it can be used not only for single sites characterization.

Italy represents the first example of this new way of considering the PSI data. Back in 2007, the Italian Government began supporting the largest ever InSAR analysis to be founded by a national government. The project was designed to map unstable areas over the entire national territory. This was possible thanks to the combined effort between Tre-Telerilevamento Europa, e-geos and Compulab (Costantini et al., 2015). The project involved processing, by means of the PSInSAR and the PSP techniques, the entire ERS 1/2 and Envisat archives over Italy (more than 15000 SAR images covering more than 330000 km^2), which called for the creation of a dedicated geospatial database to manage millions of PS points (MATTM, 2010). This interferometric database, spanning from November 1992 to September 2010, is freely available online by everyone interested in this topic (http://www.pcn.minambiente.it/mattm/progetto-piano-straordinario-di-telerilevamento/, National Cartographic Portal). The reliability of these interferometric data has successfully been proven by other authors in other Italian study cases (e.g. Pratesi et al., 2015; Peduto et al., 2017; Solari et al., 2017a). The data provided by this platform will be used in the Chapter 4 of this Thesis to demonstrate their usefulness in a building-scale analysis of deformation induced by land subsidence in the city of Pisa (Central Italy).

In the last year, a new project that exploits the capabilities of multi-pass interferometric Sentinel-1 images, has been developed by the Department of Earth Sciences of the University of Florence for continuous monitoring of ground deformation induced by hydrogeological processes in the entire Tuscany Region (Raspini et al., 2017). The SAR images, analyzed by means of the SqueeSAR algorithm, are implemented in an operational service devoted to the generation of advanced interferometric products ideally suited for being included in the risk management chain of the region. This service relies on the systematic and automatic processing of Sentinel-1 images to create updated ground deformation maps and displacement time series at every new Sentinel-1 acquisition. Moreover, deformation time series are automatically analyzed through a new post-processing method, devoted to the early identification of any anomalous trend and/or acceleration occurring during the monitoring period.

In other world nations, Sentinel-1 or data provide by other sensors have been used only to assess the feasibility of region-to-nationwide surface displacement mapping. In Great Britain ERS 1/2 and Envisat coverage was simulated and the density of PS predicted considering the possible geometric distortions generated by the topography, using what has been called “visibility map”, and the land cover of the national territory (Cigna et al., 2014). An update of this work, referred to Sentinel-1 data, was presented by Novellino et al. (2017). Similar approaches have been followed in Denmark (Marinkovic et al., 2016), in the Vorarlberg Region in Austria (Vecchiotti et al., 2017) and in Germany (Kalia et al., 2017).

4 Test sites characterization

For this work two Italian test areas at regional scale are been selected: Tuscany and Valle d'Aosta Regions. Furthermore a site at detailed scale was analyzed, the mining area of Saline di Volterra (Tuscany). In this chapter, the main geological and geomorphological characteristics of the study areas will be explained.

4.1 Geographical and geomorphological setting of Tuscany Region

The Tuscany Region is located in central Italy and extends up about 22.994 km². It is administratively subdivided into 279 municipalities and 10 provinces: Arezzo (AR), Siena (SI), Grosseto (GR), Pisa (PI), Livorno (LI), Massa-Carra (MC), Pistoia (PT), Prato (PR) and Lucca (LU). Furthermore, the Tuscan territory includes an island archipelago composed by six main islands and other small ones. The regional capital is Florence, the most populated city, with about 380.000 inhabitants.

Tuscany Region presents an extremely variegated landscape. Mountains cover 25.1% of the region from NW to SE along the Apennines, where mountain heights can be greater than 2000 meters a.s.l. (the highest Monte Prado, 2054 meters a.s.l.). The central part of the territory is predominantly characterized by hills (66.5%) and flat areas (8.4%), or wide valleys where the main rivers flow (Figure 12a).

From the climatic point of view, the region is generally Mediterranean, with hot and dry summers and moist and mild winters (Csa as in the Köppen-Geiger classification) (Peel et al., 2007), even if it locally can vary according to the position of orographic elements and coast. By a rainfall point of view, there are two precipitation peaks: the main one during the autumn period, the second one during winter or spring period. Summer is the driest season of the year (Rapetti and Vittorini, 1974). The major rainfall events are located along the Apennines, especially in the NW part, with mean annual peaks up to 2000 mm/year in Apuan Alps. Instead, the lower rainfall values are typical in the southern Tuscany, with mean annual peaks lower than 600 mm/yr (Rapetti and Vittorini, 1974; Rosi et al. 2012).

By a geological point of view, Tuscany Region belongs to the Northern Apennine. The geological setting is characterized by an overlapping of three main geological units: Ligurian, Tuscanian and Umbro-Marchigian. The Apennines are one of the youngest mountain chains in the world, formed during the Neogene and Quaternario. Active tectonic makes Apenninic area prone to several geological hazards such as earthquakes and slope instability (Bortolotti 1992; Vai and Martini, 2001).

Tuscany Region is characterized by various geological and topographic patterns; thus, geo-hazards are heterogeneously distributed throughout the territory. Figure 12b shows the spatial distribution of typical phenomena observable by radar satellite, such as landslides and subsidence. In this work it was used the landslides database published by Rosi et al. (2017), based on the improvement of Italian Landslides Inventory (IFFI) project, produced by Institute for Environmental Protection and Research (ISPRA). In this database 117.000 landslides are identified and mapped, with the definition of their state of activity; 22% of them are classified as "active", 74% as "dormant" and 4% as "stabilised". Rosi et al. (2016) derived a subsidence database for the Tuscany Region, on the basis of ERS 1/2 and Envisat interferometric products. This database is composed by 13 main zones, with a total area of 2035 km^2, equals to the 9% of the Tuscany surface. In Figure 12b shows the distribution of landslides or/and subsidence for each municipality. Sixty nine percent of the municipalities include mapped landslides, 28% record both landslides and known subsidence areas and only 0.4% of them register no-known geohazards (i.e. 1 of the 279 municipalities). These data confirm the need and importance of a priority list to manage geo-risks in an effective way.

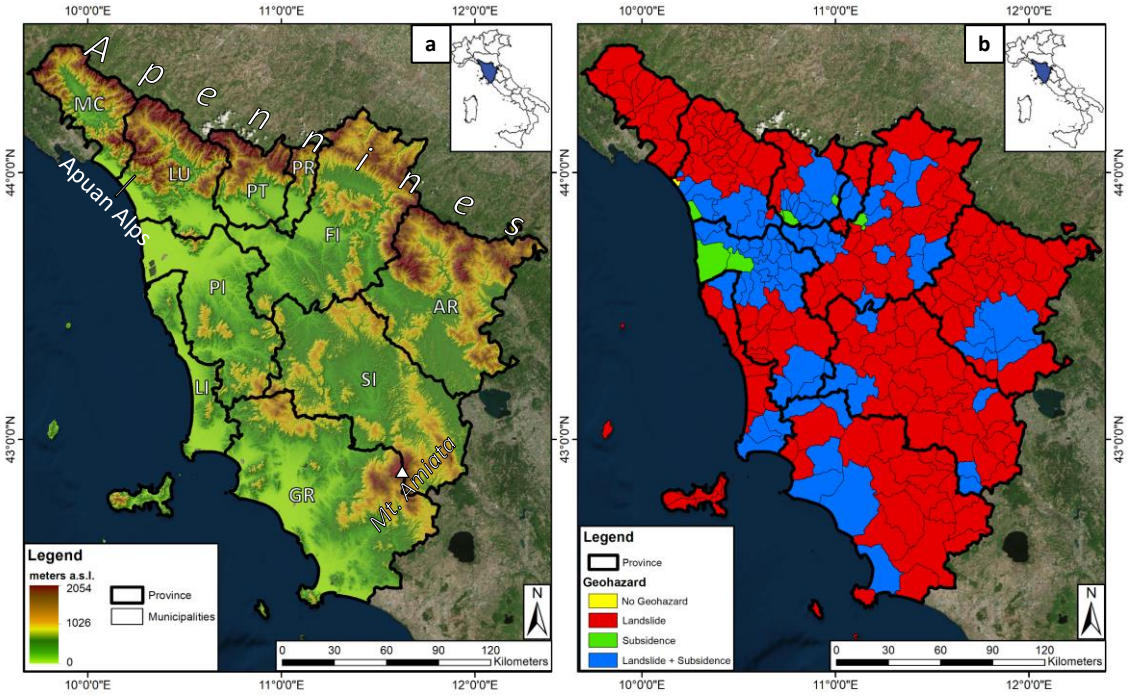

Figure 12 - Geographical characterization and Digital Elevation Model (DEM) of Tuscany Region (a) and spatial distribution of geohazard observable by satellite radar data (b).

4.2 Saline di Volterra mining site

The area of interest is located a few kilometers southwards the cities of Volterra and Montecatini Val di Cecina in the Tuscany Region (central Italy) within a hilly landscape dominated by gentle slopes and moderate reliefs (Figure 13). The village of Saline di Volterra is surrounded by 5 different mining concessions where the two deformation targets of this research are located (Figure 13). The name of the village "Saline" (salt mine in English) reflects the long-term mining activity of this area. The mining concessions cover a total of 28.5 km^2; the biggest one, Buriano, spreads for 10 km^2, whereas the smallest one, Casanova, has a surface of only 1 km^2 (Figure 13).

In addition to mining-related phenomena (i.e. sinkholes) the slopes surrounding the study area are characterized by intense denudation processes and superficial erosion phenomena that reach their maximum evolution forming badlands areas whose presence creates a peculiar landscape (Bianchini et al., 2016).

The following three chapters introduce i) the local geological context, which facilitated and promoted the mining activities, ii) the history of the Saline di Volterra brine fields with an overview on the mining activity and iii) the ground effects registered in the area.

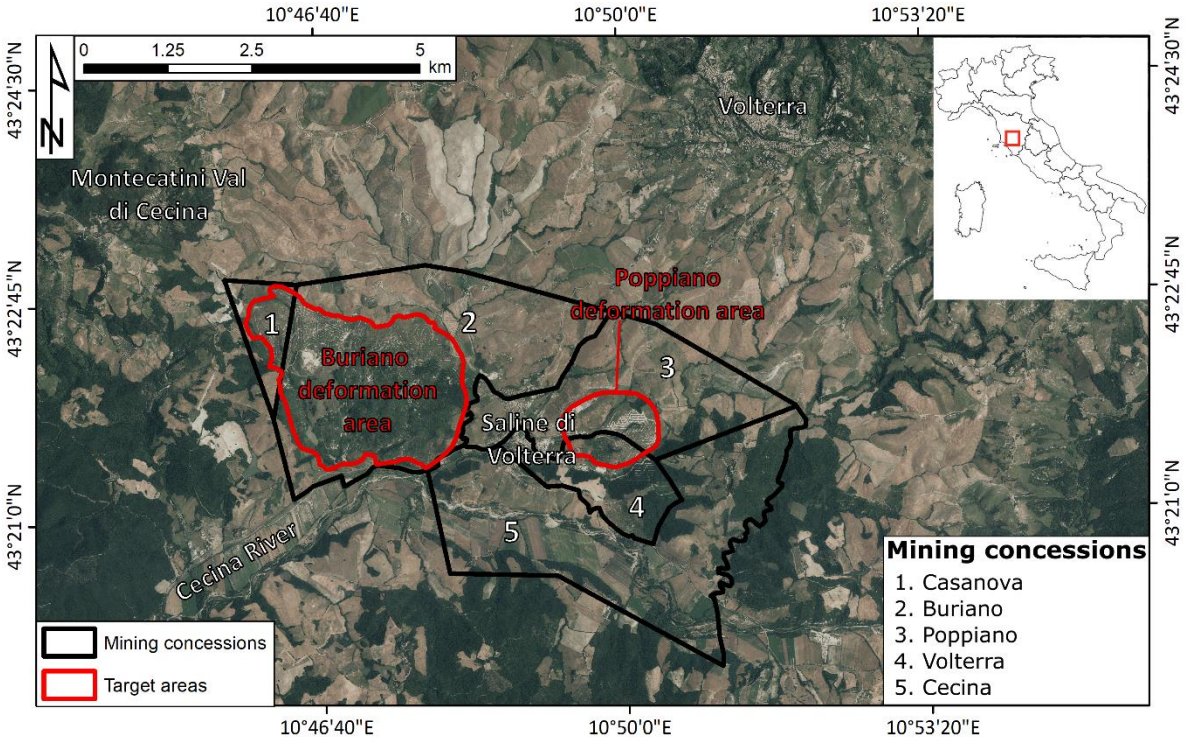

Figure 13 – Localization of the area of interest and of the mining concessions in the surroundings of Saline di Volterra in the Volterra Municipality. The background image is a 20cm AGEA orthophoto (from http://www502.regione.toscana.it/geoscopio/servizi/wms/OFC.htm).

By a geological point of view, the area of interest is located in the Volterra basin, a NW-SE oriented Miocene-Pliocene extensional basin developed in response to the eastward migration of the Apennine thrust-belt (Patacca et al., 1990). The basin is filled by a sedimentary succession ~2500 m thick (Testa and Lugli, 2000) that includes an evaporitic Messinian succession composed by gypsum and halite layers alternated with conglomerates, sandstone and claystone (Speranza et al., 2016). The upper part of this Messinian sequence, known as "Saline di Volterra formation", hosts laminitic gypsum, turbiditic gypsarenite, microcrystalline gypsum and halite with intercalations of clay, silt and sandstones (Testa and Lugli, 2000). The Saline di Volterra formation has a variable thickness ranging from a few meters to 200 m, depending on the position within the Volterra basin (Speranza et al., 2016). The whole sequence is unconformably overlaid by Pliocene marine clays ("Blue Clays"), which represent the closing sedimentation of the basin and widely outcrop in the investigated area (Figure 14).

Just a few information is available to reconstruct the subsurface setting of the Messinian sequence in the area of interest. Nicolich et al. (2002) investigated the area of the Buriano mining concession through high resolution 3D seismic surveys, discovering the presence of cavities in the saline layer at a depth of 150 m to 300 m. Burgalassi et al. (2010), stated that the productive salt levels are 10 to 40 m thick and are found at a depth ranging from 60 to 400 m. Speranza et al. (2013, 2016) analyzed the rheological properties of the salt levels in the mining area of Saline di Volterra. The salt samplings were collected from deep cores which intersected the salt deposit between 122 and 165 m below surface, for a total thickness of 43 m. These authors recognized four salt facies, with variable percentage of halite and gypsum layers and variable grain size of the crystals. Speranza et al. (2016) estimated that halite represents the 40% of the total volume of the Messinian series.

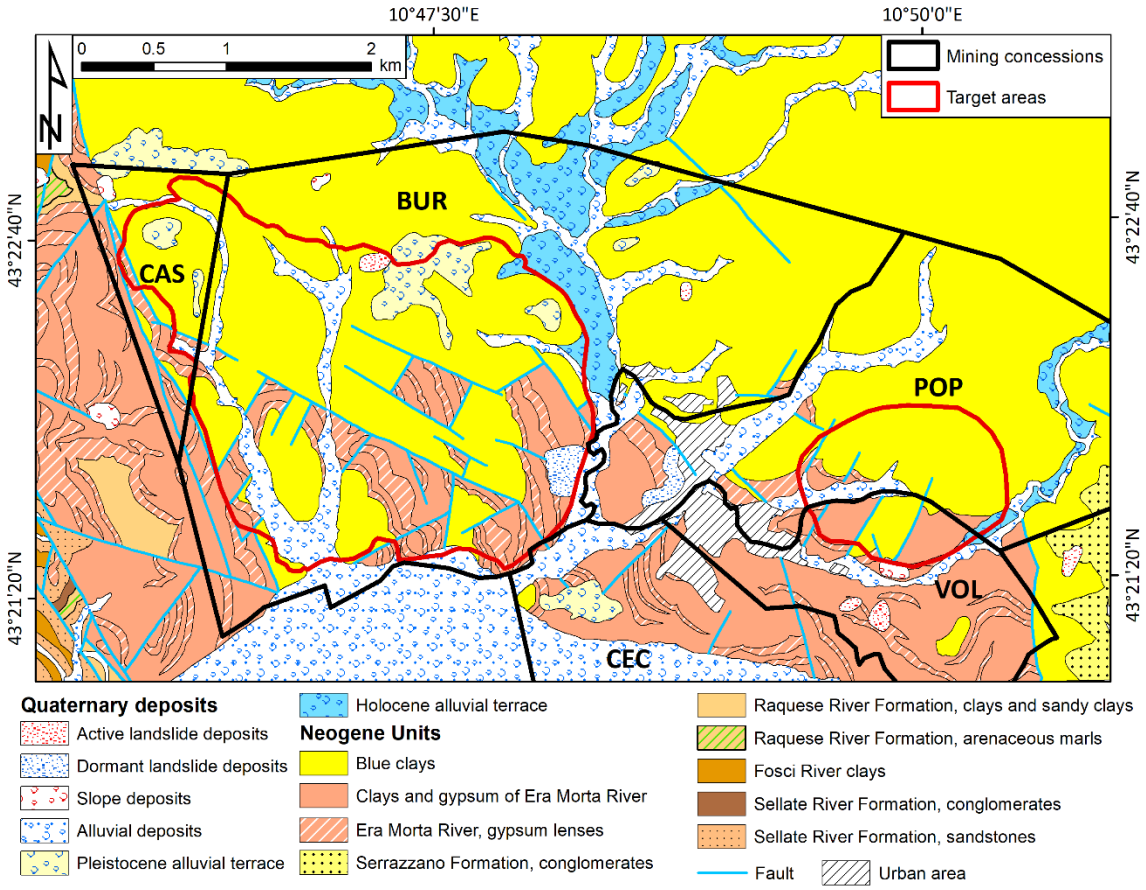

Figure 14 – Geological map of the study area. From the Geological Map of Italy, 1:50.000 scale, Sheet 295-Pomarance (https://www.isprambiente.gov.it/Media/carg/note_illustrative/295_Pomarance.pdf).

The presence of exploitable salt levels in Saline di Volterra was already known during the Roman Empire. The Romans called the area “moje” from the Latin word “muriae” (brine in English). The real exploitation of the salt layers started in the Middle Ages when the saturated water that gushed out from several springs was left evaporating naturally (Nannoni and Capperi, 1989). The intensive industrial extraction of the salt levels started at the beginning of the nineteenth century (1910) by the Saline di Stato, a company ruled by the central government, and by the private company Solvay (Burgalassi et al. 2010). In the area of interest, five mining concessions are present (Figure 13): Buriano and Casanova in the Montecatini Val di Cecina municipality, Cecina, Poppiano and Volterra in the Volterra municipality.

Salt solution is the mining technique applied here, following the Trump method. Such method is rather simple: a dissolving fluid, typically water, is pumped at the depth of interest to dissolve the salt level; the saturated brine is then pumped back to the surface (Johnson, 1998; Warren, 2016). The process is subdivided in two phases. Firstly, water is pumped through the boreholes at the depth of interest and starts to dissolve the salt level. Compressed air is used to constrict and contain the fluid within the salt level, creating a flow that allows connecting the multiple cavities created by adjacent boreholes. Then, some boreholes are equipped with pumps to extract the produced semi-saturated brines; other boreholes continue to reinject new fresh water. After multiple cycles, the final saturation value of 300 g/L is reached (Burgalassi et al., 2010) and the brine is extracted and channeled, through a system of pipes, to the treatment plant of Rosignano, along the coast (38 km western than Saline di Volterra). In the treatment plant, the sodium chloride is finally extracted from the brine trough a chemical process. The injection/extraction boreholes are disposed in the mining concessions in a regular grid with spacing between the boreholes of 40-45 m. Every mining panel

counts 60 to 360 boreholes (Burgalassi et al., 2010). As stated by ARPAT (2006) the actual production rate requires to drill 50-60 additional boreholes per year.
Burglassi et al., 2010 estimated that the total amount of salt deposits in the subsurface of this area is 466 million tons; however, considering an extraction ratio of 65% (Pinna, 2002), the effective amount of mineable material is 300 million tons. The time needed for the total consumption of this resource has been estimated in about 200 years. The main environmental impacts of the mining activity are three: i) overexploitation of fresh water, ii) salinization of streams and aquifers and iii) subsidence/sinkholes (http://www.arpat.toscana.it/notizie/arpatnews/2013/174-13/174-13-gli-impatti-ambientali-nelle-attivita-minerarie-connesse-alla-coltivazione-del-salgemma).

4.3 Geographical and geomorphological context of Valle D'Aosta Region

Valle d'Aosta (VdA) is the smallest Italian Region, covering only 3,262 km^2. Almost the 50% of its territory has an elevation higher than 2,000 m. a.s.l., thus it can be considered as a mountain region with peaks reaching 4,000 m. a.s.l. and main valleys above 300 m. a.s.l. (Figure 15).
By the geological point of view VdA is part of the Western Alps, cutting through the main alpine structural domains: Austroalpine, Penninic and Helvetic (Dal Piaz et al., 2003). All the units show a metamorphic imprinting passing from eclogitic or blueschist facies to low grade metamorphism (Frey et al., 1999). Therefore, the geological context of VdA is characterized by a complex pile of metamorphic-tectonic nappes, consequence of an intense post collisional and neo-tectonic activity (Bistacchi et al., 2001). Thus, the tectonic and geo-structural characters influenced the evolution of the reliefs and the current slope dynamics (Martinotti et al., 2011).
Glacial action is another main factor that control the past and current orography of VdA (Martinotti et al., 2011). The main morphological traits of VdA are: i) a central valley, east-west oriented, in which the Dora Baltea River flows, and ii) several lateral/tributaries valleys north-south oriented. This configuration is a remnant of the Quaternary glacial modelling still influencing slope dynamics (Carraro et al., 2004). The glacial morphology has been progressively deepened by fluvial action that eroded glacial landforms, depositing alluvial fans at valley bottoms (Martinotti et al., 2011).
VdA has a high population density only along the main valley whereas entire portions of the regional territory are partially or totally inhabited. The land cover is mainly composed of forests and grasslands, gradually replaced at high altitudes by exposed rocks, debris with sparse or no vegetation and glaciers. This environmental asset is strongly influenced by local climatic variations produced by high peaks that act as morphological barriers for humid air masses coming from the Mediterranean Sea or the Atlantic Ocean (Ratto et al., 2003). Thus, the morphology of VdA creates a wide spectrum of temperature and snow/rain precipitation regimes in which mountainous areas records abundant snowfalls and average rainfalls around 1,000-1,100 mm/yr, whereas along the main valley the climate is drier with average precipitation around 600 mm/yr (Ratto et al., 2003).
In the VdA Region 2,052 landslides have been mapped in the framework of the Italian Landslide Inventory (IFFI) project, founded by the Italian Government and conducted by the Institute for Environmental Protection and Research (ISPRA) starting from 1999 (Trigila et al., 2010). The VdA database includes both landslide and DSGSD phenomena, covering 592 km^2, and has been updated in 2015 (Figure 15). The density of slope movements is equal to 0.7 phenomena/km^2 and the landslide index (ratio between area covered by landslides and the regional territory) amounts to the 18%. The 30% of landslides mapped are classified as rockfalls (including topples) mainly affecting metamorphic rocks (Giardino et al., 2007). Shallow landslides and mud/debris flows are quite frequent as well, composing the 24% of the landslides mapped. These

motions are related to intense rainfalls events that also locally induce flooding (Salvatici et al., 2018). Despite being only the 13% of the total known phenomena, DSGSD cover the 76% of the total area occupied by landslides, sometimes involving entire mountain flanks (e.g. Hône, Villeneuve, Quart and Breuil-Cervinia DSGSD).

Considering its geomorphological and climatic context, VdA is characterized by mass movements related to periglacial landforms, such as rock glaciers, that are quite common in alpine environments (Haeberli et al., 2006). Rock glaciers are defined as ice-rich or frozen debris steadily creeping along non-glacierized mountain slopes; they are commonly subdivided in active, inactive or relict, depending on their ice content (Haeberli et al., 2006). Active rock glaciers register a steady-state creep with deformation rates varying from cm/yr to several m/yr (Haeberli et al., 2006), whereas inactive and relict rock glaciers, because of the low or null ice content, do not almost move (Barsch, 1996). In VdA 937 rock glaciers are mapped, covering the 2% of its territory; 57% of them are classified as relict (Morra et al., 2011). Active rock glaciers are usually found above 2,200 m. a.s.l. along north-exposed slopes whereas relict landforms are found at lower altitudes, but never below 1,600 m. a.s.l. (Cignetti et al., 2016).

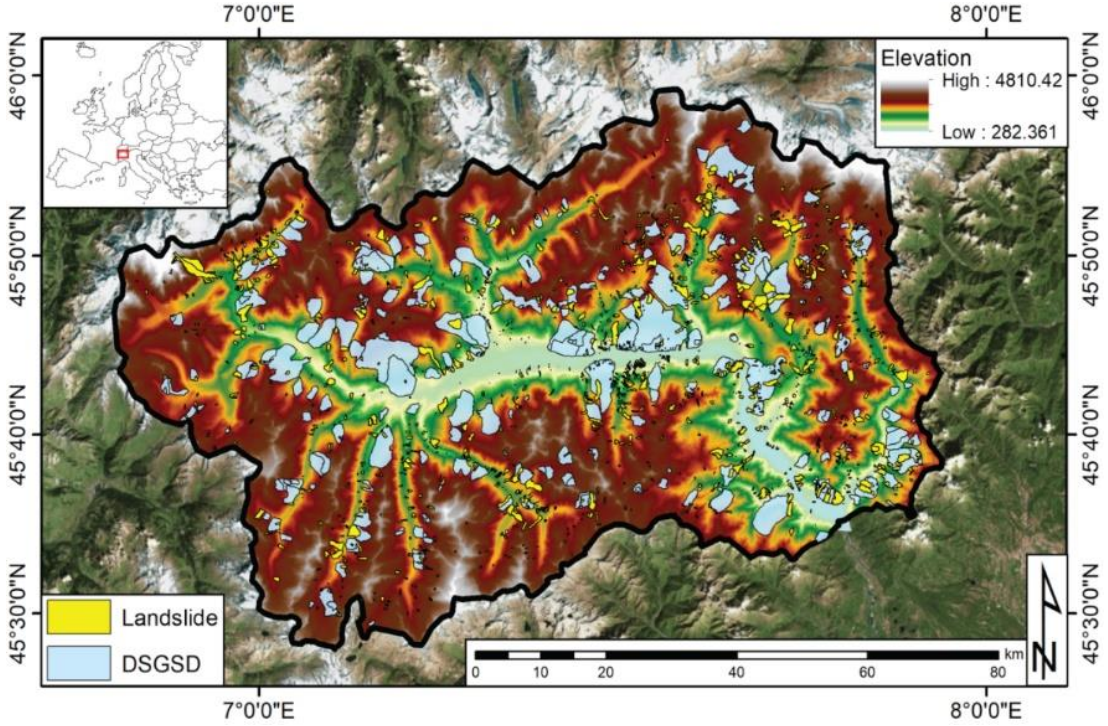

Figure 15 - Geographical localization and digital elevation model of the Valle d'Aosta Region. The landslide contours and the DSGSD are included in the IFFI catalogue of VdA. The map is overlaid on a Bing Aerial image.

5. Methodology

In this chapter, it will be explained the methodological approach in order to retrieve the most representative moving areas in the Tuscany and Valle d'Aosta Regions. Furthermore, the target oriented processing approach for Saline di Volterra mining area it will be presented.

5.1 Tuscany region: wide area mapping

The goal of this methodology is to highlight the most relevant ground deformations in Tuscany Region by means of satellite interferometry and using simple GIS (Geographical Information System) tools, making an analysis from April 2017 to April 2018 subdivided into three periods. The workflow is conceived to be reproducible and fast to apply, providing a geodatabase that contains interferometric and qualitative parameters, concerning the hydrogeological phenomena.

The methodology is subdivided into three main steps:

(1) deformation map generation;
(2) active moving areas extraction;
(3) cluster classification and persistence analysis.

5.1.1 Deformation maps generation

To obtain the ground deformation map of Tuscany Region we used Sentinel-1A and Sentinel-1B images from October 2014 to April 2017, to create the first deformation map by means of SqueeSAR algorithm (Ferretti et al., 2011). After that, others two deformation maps were obtained, i.e. from October 2014 to October 2017, and from October 2014 to April 2018, in order to update the results every six months and highlight the evolution of the hydrogeological phenomena of interest. For these three periods, a total of 130 Sentinel-1 images have been used.

The SqueeSAR algorithm represents the evolution of the Permanent Scatterer SAR Interferometry (PSInSAR) (Ferretti et al., 2001), that is aimed at identifying radiometrically stable reflectors called Permanent Scatterers (PS), exploiting the whole stack of SAR images. Every PS represents a pixel of a SAR image with high signal coherence, mainly corresponding to rock outcrops and man-made objects. The main drawback of this technique is the low density of PS that could be obtained in agricultural and peri-urban areas (< 10 PS/km^2 using C-band radar images), compared to the PS density in urban areas (> 100PS/km^2 using C-band radar images).

The SqueeSAR algorithm was designed to overcome this limitation, defining a new type of PS points: the Distributed Scatterers (DS). A DS is a target corresponding to an area, where a certain number of neighbouring pixels share similar reflectivity values and moderate interferometric coherence. By combining and merging the signal of these pixels, it is possible to extract a point-like feature with high interferometric coherence. DS typically match with homogeneous areas such as deserts, debris areas or uncultivated area. SqueeSAR approach jointly process PS and DS considering their different statistical behaviour. This is possible thanks to a space adaptive filtering, DespecKS (Ferretti et al., 2011), that is able to statistically average homogeneous pixels (SHP) preserving the information of point-wise associated to point targets. The filter is based on Kolmogorov-Smirnov statistical test (Stephens 1970; Kvam et al., 2007). Basically, for every image-pixel, this kind of statistical test is applied to all the pixels within a certain estimation window, centred on the

pixel under analysis to select SHP families (Ferretti et al., 2011). After that, it is possible 1) to despeckl amplitude data; 2) to filter interferometric phase values; 3) to estimate coherence values properly.

5.1.2 Active moving areas extraction

Extracting deformation maps from Multi-temporal InSAR technique represents a good starting-point to highlight possible relevant zones affected by hydrogeological risk. In this case, we derived active moving areas using a simple hot-spot-like method in GIS environment, already followed by other authors (Meisina et al., 2008; Barra et al., 2017), divided in two main steps:

- Velocity filtering: PS and DS points were filtered with a velocity threshold of ±7,5 mm/year. This value is equal to three times the standard deviation of the velocity values of both datasets. This value has been chosen to extract just the most representative points for "fast" moving areas at regional scale.
- Cluster extraction: the resulting filtered map was further analysed to derive the final moving areas. This product was obtained buffering PS/DS. We choose a buffer size of 100 meters and a cluster size with minimum three PS. We chose this buffer size and cluster size based on our knowledge, defining the common size of a landslide (Bianchini et al., 2012). Each cluster is characterized by a value of mean velocity, mean standard deviation and mean coherence of the time series of PS/DS points composing the clusters.

5.1.3 Cluster classification and persistence analysis

The classification of each cluster is based on radar interpretation, as firstly defined by Farina et al., (2007), introducing the PSI analysis cross-compared with ancillary data, such as geology, geomorphology, multi-temporal ortophoto, regional technical maps. For every type of geohazard the following databases were used:

- for lanslides (La) phenomena, the IFFI inventory improved with ERS 1/2 and Envisat interferometric data (Rosi et al., 2017);
- for subsidence (Su) and uplift (Up) phenomena, the inventory published by Rosi et al., (2016);
- for deformations due to geothermal activity (GA), the geothermal inventory of Tuscany Region;
- for deformations due to mining activity (MA), the mining inventory of Tuscany Region.

Furthermore, the three periods were analysed to highlight possible temporal and geometric persistence areas (TGPA) among clusters. A TGPA is defined when clusters of moving points, which are present in each period and acquisition geometry, overlap each other. TPGA represent the most enduring and representative ground deformations, thus they are useful to highlight the most relevant situation that have to be prioritized.

5.2 Saline di Volterra detailed scale target oriented processing

In this case, a detailed scale processing approach developed in the CTTC research centre was used, in order to improve the point density and to catch properly the most representative deformation movements. It is based on the direct integration of the interferograms, in order to retrieve the deformation occurred in the mining area of Saline di Volterra. The workflow of the methodology is presented in Figure 16.

5.2.1 Processing set up

Data processing starts with the generation of the interferogram stack, following the classical differential interferometry approach (Rosen et al., 2000). Interferograms (ITFs) are generated starting from a stack of

127 coregistered Sentinel-1 images (both 1A and 1B). The images cover the period between September 2016 and November 2018. ITFs are generated with the shorter temporal baseline possible, i.e. 6 or 12 days. A 30 m Shuttle Radar Topographic Mission (SRTM) Digital Elevation Model is used to remove the topographic contribution from the interferograms. The precise orbits provided by the European Space Agency are used as well.

Phase splitting is performed on the stack of wrapped ITFs to extract the low (LF) and high (HF) frequency components. A spatial filter is applied to every ITF to do so. A Butterworth filter is used in this work, in the form:

$$G(\Omega) = \frac{1}{\sqrt{1 + \left(\frac{\Omega}{\Omega_C}\right)^{2N}}} \quad (1)$$

where G is the gain, Ω is the frequency, Ω_C is the cut-off frequency and N is the order. The spatial filtering generates the LF interferograms, whose residuals represent the HF component. The LF component is assumed to be almost completely formed by the atmospheric contribution (Gomba et al., 2015) although some fast movements with high spatial correlation can still be present. The HF component contains the slow movements (few mm/yr to several cm/yr), the fast local movements (below 2 mm/day) and the residual topographic errors (Crosetto et al 2011). The analysis of LF and HF ITFs is performed by following two parallel paths (Figure 4).

The HF path is composed of three steps: i) pixel selection, ii) phase unwrapping and iii) direct integration. Pixel selection is based on a novel approach called “triplets closure”. As the name suggests, the method is based on triplets of radar images (i, j and k) and interferograms generated with different temporal baselines, in this case 6 and 12 days ($\Delta\Phi_{i\text{-}j}$, $\Delta\Phi_{j\text{-}k}$, $\Delta\Phi_{i\text{-}k}$). Assuming that the sum of the short baseline ITFs ($\Delta\Phi_{i\text{-}j} + \Delta\Phi_{j\text{-}k}$) equalizes $\Delta\Phi_{i\text{-}k}$, the error (ε) is:

$$\varepsilon_{i-j} + \varepsilon_{j-k} = \varepsilon_{i-k} \quad (2)$$

in case of low noise ITFS, ε is close to zero. The error increases along to the level of noise. The standard deviation of ε calculated with (2) over the whole interferograms stack for each pixel is used to select the points reliable enough to unwrap the phase. The pixels with standard deviation values below the threshold are selected as phase unwrapping candidates. Phase unwrapping is performed by means of the Minimum Cost Flow method (Costantini et al., 1999). Finally, a point-wise direct integration of the unwrapped interferograms is performed. The direct integration is expressed in the form:

$$n = 0 \div N \begin{cases} \Phi_n = \Phi_{n-1} + \Delta\Phi_{(n-1)n} \\ \Phi_0 = 0 \end{cases} \quad (3)$$

where Φ_n is the accumulated phase at the acquisition time n, $\Phi_{n\text{-}1}$ is the accumulated phase at the acquisition time n-1 and $\Phi_{(n\text{-}1)n}$ is the unwrapped interferometric phase of the interferogram calculated using the images acquired at the times n-1 and n. The first image is set to zero (Φ_0). The output of the direct integration is, for each point, the temporal evolution of the phase with respect the first acquisition. The phase is converted in displacement by following:

$$Disp_n = \frac{\Phi_n}{4\pi}\lambda \quad (4)$$

where $Disp_n$ is the accumulated displacement of the point at the acquisition time n, Φ_n is the accumulated phase at the acquisition time n (in radians) and λ is the wavelength of the satellite. Each point is then characterized by n values of displacement, forming the time series, and by a value of velocity calculated over the reference period.

The LF path is composed by three steps: i) network generation, ii) pixel selection, iii) 2+1D phase unwrapping. The LF analysis begins with the set of short baseline LF ITFs which were previously generated. In order to increase the redundancy of the network, the LF ITFs are crossed to derive synthetic ITFs with longer temporal baselines. The measurement point candidates are then selected by applying the triplets closure concept (2) to the newest LF network of interferograms. The 2+1D unwrapping method is finally applied to derive the time series of deformation (Devanthéry et al., 2014). Through this method is possible to check the consistency of the spatial unwrapping in time, thanks to the redundant ITFs network, and on a pixel-wise basis, i.e. on the points selected with the triplets closure method.

The final products of the two parallel processing paths are time series and deformation maps for the low and high frequency components. The two products are then combined again in order to annul the accumulation of errors related to the LF-HF splitting. This error accumulation results in residual trends, with opposite sign between the LF and HF results. Finally, a classical atmospheric phase filtering is applied to remove the remaining low frequency signal not due to the ground deformation. The final deformation map is then georeferenced in a geographic reference system.

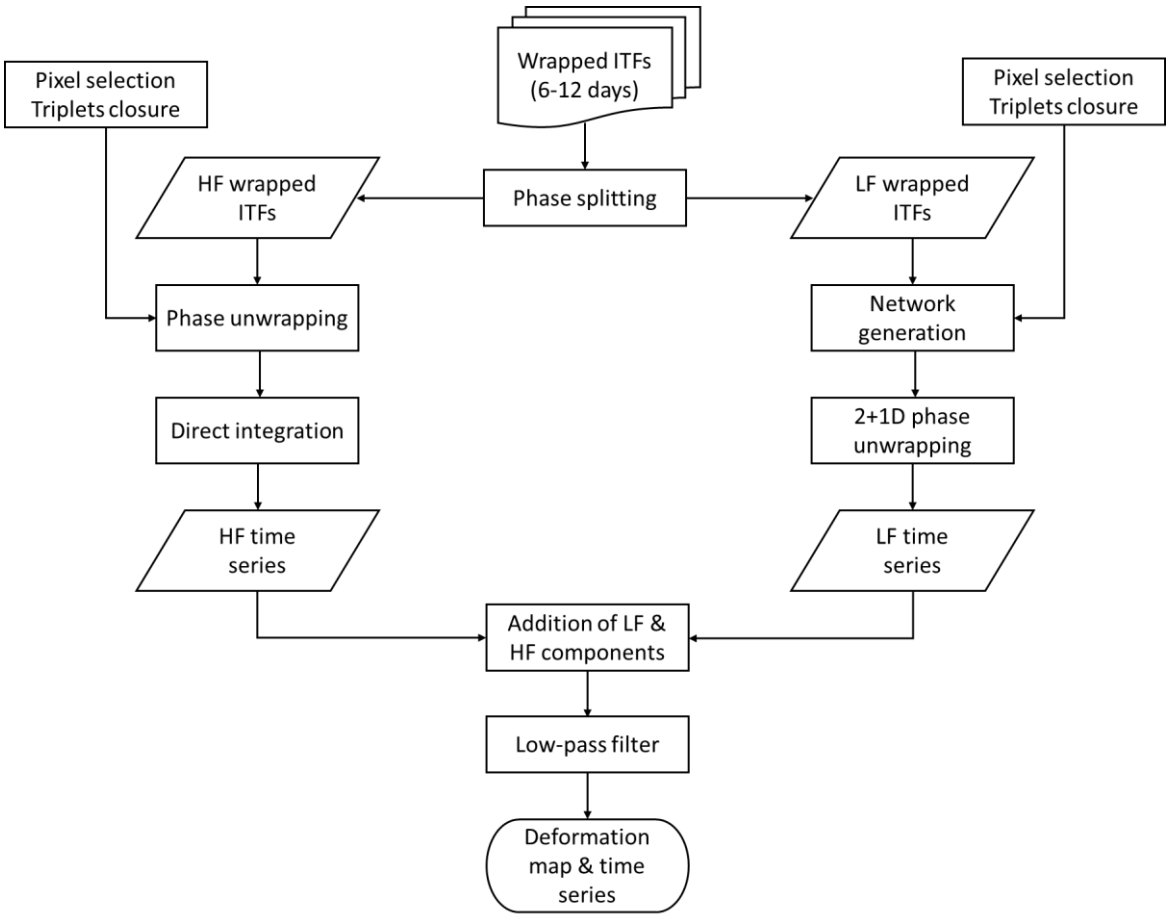

Figure 16 – Workflow of the processing approach. ITFs, interferograms; HF, high frequency; LF, low frequency.

5.3 Valle D'Aosta Region wide area mapping

The concept of the methodology is to extract moving areas from large interferometric datasets that are subsequently radar-interpreted by using simple GIS (Geographical Information System) tools (Farina et al., 2007). The final output is a geo-database containing multiple information, regarding both magnitude of ground motion and type of process that generated it. In addition, a qualitative parameter for the evaluation of the "interferometric reliability" of each moving area is derived.

Following this concept, the methodology is subdivided into four main phases:

1) pre-processing analyses:
2) deformation map generation;
3) active moving areas extraction;
4) radar-interpretation and geo-database compilation.

5.3.1 Pre-processing analyses

Because of its climate, morphology and land cover, VdA is a challenging environment for interferometric analyses. Considering this facet, we performed a pre-processing analysis of the possible topographical and land cover effects on the spatial distribution of PS/DS points. For this aim we exploited the methodology presented by Notti et al. 2014, that allows deriving the Corrected R Index (CRI), a combination between the effects of topography (R Index - RI) and land cover (Land Cover Index - LUI) on PS points detection.

The RI depends on the terrain morphology (slope and aspect) and on the radar geometry (incidence and azimuth angles). It varies between 0 and 100, where 0 means that layover, foreshortening or shadowing effects limit the detection of radar targets; on the other hand, 100 defines an area where the topography is "radar friendly", thus guaranteeing the recognition of PS points. Usually, a value of RI higher than 50 ensures that the topography not much affects the obtainable results; in this case the land cover acts as main factor for radar targets detection (Notti et al., 2014; Bianchini et al., 2013). In this work, we used a 10 m resolution Digital Elevation Model for deriving slope and aspect maps of the VdA.

The definition of the LUI is not related to a fixed rule, but to an empirical classification of land cover that varies depending on the land use, on the sensor band, as well as on the PSI processing. The LUI ranges between 0 and 100, where 0 means that a surface with extremely low probability of producing radar targets whereas the value 100 identifies a surface with a very high probability of hosting PS points. Table 2 presents the values of LUI selected for the VdA Region, considering the acquisition band and the type of processing (C band/SqueeSAR algorithm). In fact, for a SqueeSAR approach the values of LUI can be slightly increased, especially in grasslands and cultivated areas. Table 2 has been used to reclassify the Corine Land Cover (CLC) of the VdA produced, at the 1:100,000 nominal scale, for the whole Italian territory in 2012 (Corine Land Cover of Italy (2012) available online).

The final CRI is obtained as a weighted average of RI and LUI. In case of RI values higher than 50 only the LUI is considered (Notti et al., 2014). If just one of the two input layers is equal to 0, the CRI will be null. The input data and the output map are simply derived in a GIS system by means of standard tools, common for the most used GIS environments.

CLC class	Description	LUI value
111	Continuous urban fabric	100
112	Discontinuous urban fabric	90
121	Industrial or commercial units	100
122	Road and rail networks and associated land	100
124	Airports	100
131	Mineral extraction sites	80
142	Sport and leisure facilities	60
221	Vineyards	40
222	Fruit trees and berry plantations	30
231	Pastures	40
242	Complex cultivation patterns	40
243	Land principally occupied by agriculture, with significant areas of natural vegetation	40
311	Broad-leaved forest	10
312	Coniferous forest	10
313	Mixed forest	10
321	Natural grasslands	50
322	Moors and heathland	40
324	Transitional woodland-shrub	50
332	Bare rocks	80
333	Sparsely vegetated areas	70
335	Glaciers and perpetual snow	0
511	Water courses	0
512	Water bodies	0

Table 2 - LUI values for the different classes of the third level CLC of the VdA Region.

5.3.2 Deformation map generation and moving areas mapping

The ground deformation map for the whole VdA Region is derived by analyzing large stacks of C-band Sentinel-1 images, composed by 130 images reaching the end of February 2018, starting from October 2014 for the ascending orbit and from November 2014 for the descending orbit. They are been processed by means of the SqueeSAR algorithm, the same used for the Tuscany region site, obtaining one deformation map for each geometry.

Firstly, the deformation map is filtered to extract the PS points in both orbits that records the highest deformation rates above the region. A stability threshold equal to 10 mm/yr is set to this aim. This quite high value, equal to 4 times the standard deviation of the datasets, has been chosen for detecting only the highest deformation rates that commonly characterize unstable rock debris on the steep slopes of VdA. The value is near the threshold of 16 mm/yr used for distinguishing very slow and slow landslides, as defined by Cruden and Varnes, 1996. Moreover, this value has been chosen jointly with the regional authorities, considering their specific requirements. Considering this, we will not map DSGSD-related deformation that involve large slope sectors with deformation rates frequently lower than 10 mm/yr (Crosta et al., 2013). Activations of portions of DSGSD systems are anyway *a priori* not excluded.

Secondly, the filtered deformation maps are further analyzed to extract significant deformation clusters and remove isolated, non-representative, points. This is done by buffering the PS points of the filtered deformation maps and then automatically join adjacent PS in a GIS environment. We choose, as for the Tuscany region, a buffer size of 100 m and a minimum cluster size of 3 PS points for obtaining the final moving areas (Bianchini et al., 2012).

Finally, for each moving area an index of the “interferometric reliability” of the measured deformation is derived. This index is based on two parameters: i) mean coherence of the time series of the PS points composing the cluster and ii) percentage of the real ground motion vector that can be registered considering the Line Of Sight (LOS) of the sensor (coefficient C). Coherence is used as a proxy for the noise of the time series, considering the parameter as the deviation between the linear model used to calculate the velocity and the real time series. This parameter gives hints on the presence of possible non-linear deformation affecting the PS point. Coefficient C is calculated starting from a relationship between slope, aspect and direction cosine of the LOS, as defined by Notti et al., 2014. This parameter is a powerful index for evaluating the magnitude of the real displacement vector that can be seen along the LOS of the sensor. Coefficient C ranges between -1 and 1; values close to zero means that the ground motion cannot be correctly estimated or that can be highly underestimated. For combing these two parameters we defined a contingency matrix, shown in Figure 17. The result of the matrix is a code that express the level of interferometric reliability depending on the quality of the time series (coherence) and on the topography effect (coefficient C).

The final moving areas are delivered in shapefile format, one for each orbit, containing the value of mean velocity, mean coherence, mean standard deviation and interferometric reliability of each one of them.

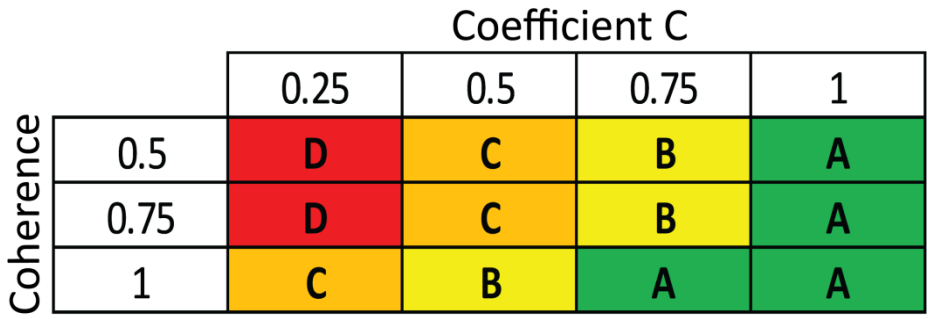

Figure 17 - Contingency matrix for the calculation of the interferometric reliability of each moving area. Values ranges between A (high reliability) to D (not reliable).

5.3.3 Radar-interpretation and geo-database creation

To provide a complete database of ground motions, functional for Civil Protection practices, the moving areas have to be radar interpreted (Farina et al., 2007) and included into a specifically designed geodatabase.

In addition to the interferometric data, the geodatabase contains information regarding:

- geographical localization of the moving area, i.e. municipality, local toponym, nearest road name;
- morphological context, i.e. mean altitude and slope;
- intersection between moving areas and VdA landslide inventory (i.e., 2015 IFFI catalogue). If a moving area contains or is contained into an already mapped landslide specific information regarding the phenomenon will be added to the geodatabase (type of movement, identification code, year of occurrence and so on);
- intersection between moving areas and VdA catalogue of rock glaciers. These data could be useful to identify the high-altitude instabilities of permafrost-rich rock masses. The catalogue is available online and contains information about the location of glaciers and rock glaciers and their state of activity (Valle d'Aosta Region Glaciers and Rock Glaciers Catalogue, 2018).

6. Results

In this chapter the results obtained by following the previous methodologies will be explained for all of the test areas.

6.1 Tuscany Region

The first step of the methodology is devoted to the generation of three deformation maps performing a SqueeSAR analysis of Sentinel-1 images. Figure 18a and Figure 18b show the deformation maps regarding the first period (October 2014 - April 2017), representing the starting point for the multi-temporal comparison of deformation clusters. These maps offer a great wealth of information of ground velocity distribution and they can be used to spot unstable area at regional scale. It is possible to observe two main areas in red (representing points with negative velocities, i.e. movements away from the sensor), the first one located in northern Tuscany and the biggest one in the south-western part. These areas are well-known in scientific environment, both referred to subsidence phenomena: the first one along the Firenze-Prato-Pistoia basin (Colombo et al., 2003; Del Soldato et al., 2018b) and the second one in the Larderello-Travale area where geothermal activities take place (Batini et al., 2003), producing relevant subsidence effects (Manzella et al., 2018). In the same way, it is possible observing PS/DS points probably attributable to landslides phenomena, both in the Apennine area and in the southern part of the Tuscany Region.

Table 3 shows the information about PS data of the three analysed periods. The deformation maps were obtained starting from a minimum of 68/70 radar images for the first period (October 2014 – April 2017) to a maximum of 126/130 images for the last period (October 2014 – April 2018). The number of PS/DS extracted is between 855.000 and 863.000, with a mean density of 33 points/km². This latter parameter turns out to be maximum in urban areas, while minimum or equal to zero in cultivated areas and forested Apennine areas.

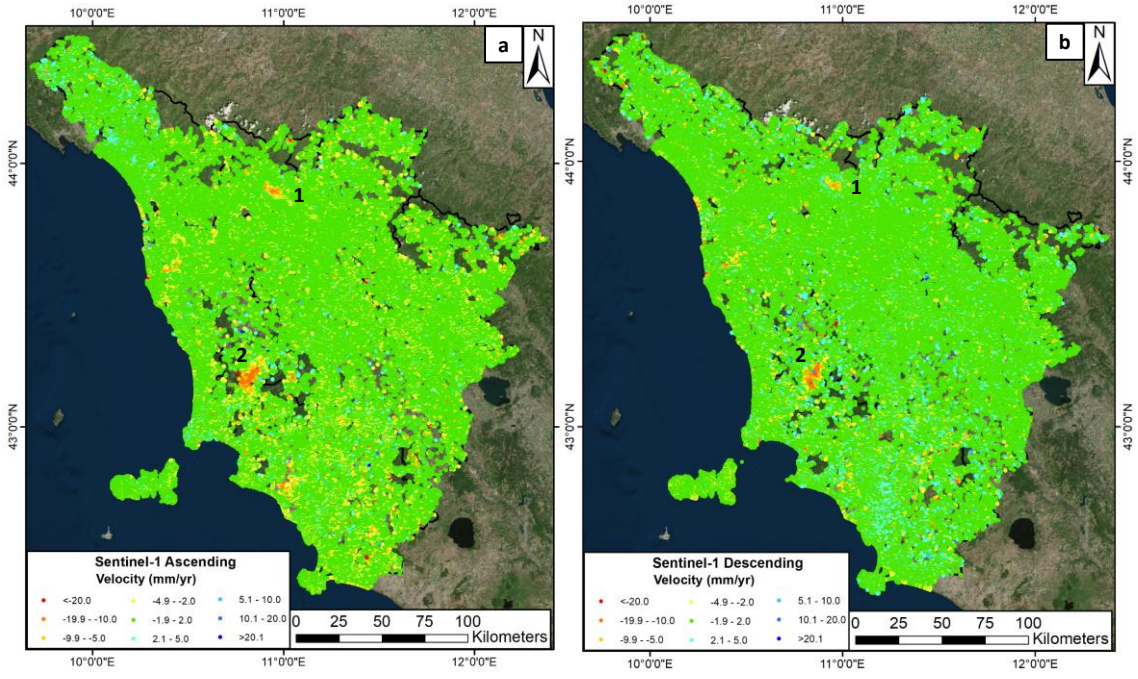

Figure 18 - Deformation map in ascending geometry (a) and descending geometry (b) from October 2014 to April 2017 using SqueeSAR algorithm. 1): Firenze-Prato-Pistoia basin; 2): Larderello-Travale area.

Period	Geometry	Images	PS/DS	Velocity (mm/yr)			Mean Coherence
				min	mean	max	
1°	Asc	70	858.000	-63	0.9	26	0.89
1°	Desc	68	855.000	-104	0.87	43	0.91
2°	Asc	99	863.000	-77	0.95	22	0.9
2°	Desc	96	861.000	-43	0.92	43	0.9
3°	Asc	130	860.000	-65	1.2	21	0.9
3°	Desc	126	859.000	-39	1.1	34	0.88

Table 3. Statistics of deformation maps. 1° period: October 2014 to April 2017, 2° period: October 2014 to October 2017, 3° period: October 2014 to April 2018.

6.1.1 Active moving areas extraction

Once that the deformation maps are obtained, it is possible to extract the active moving areas as described in the Chapter 5.1.2. After the velocity filtering equal to ± 7,5 mm/yr, the PS/DS number is decreased by 99% in all the acquisition periods and geometries. In Table 4, the statistics about clusters extraction are summarised. "PS/DS" column indicates the number of remaining points after velocity filtering; this number decrease from the first to the third period, with a maximum of 5.818 points in the first one, and a minimum of 4.328 points in the third one. This is due to a reduction of the general noise level of the datasets connected to the increase of the number of radar images analysed that grants an improvement of the accuracy of the results and of the velocity estimation. Consequently, the number of single points, that could represent false positive, is reduced. In the same way, clusters extracted from the deformation maps decrease from the first to third period as well, with a minimum of 86 in the 3° period, to a maximum of 127 in the 1° period. The percentage of clusters overlapping in different periods is equal to 50% in ascending geometry and 62% in descending orbit.

Period	Geometry	PS/DS	Clusters	Overlapping percentage
1°	Asc	5.818	127	**50%**
2°	Asc	5.490	94	
3°	Asc	4.328	86	
1°	Desc	5.694	120	**62%**
2°	Desc	5.113	123	
3°	Desc	4.845	102	

Table 4 - Statistics for filtered deformation maps. 1° period: October 2014 to April 2016, 2° period: October 2014 to October 2017, 3° period: October 2014 to April 2018.

6.1.2 Clusters classification

Following the last step of the methodology, the deformation clusters are classified on the basis of their triggering factor. Figure 19 shows the classification and position of the clusters and TGPA. The clusters due to landslides are located especially in the mountain areas (88%) along the Apennine chain and near Mt. Amiata. The landslide cluster with the highest PS/DS density is located in the mucipality of Cavriglia (Arezzo province), with a maximum of PS/DS points of 210 in the second period and a minimum of 90 in the third period, in an area of 1.6 km^2. The maximum LOS velocity recorded is equals to 24 mm/yr. The 100% of the clusters due to geothermal activity are located in Larderello-Travale area, the most ancient exploited geothermal field in the world (Batini et al., 2003). The clusters due to subsidence phenomena are mainly found in the Pisa and Livorno provinces, with a percentage equals to the 60% of the total. They are mainly located in agricultural areas, likely due to the exploitation of groundwater, and in harbour areas, related to sediment compaction. In this zone, the main group of clusters, with an area of 9 km^2, affect the structures of the Livorno freight terminal, started to be built in 2000, and composed by heavy facilities, such as warehouses and commercial areas. The subsidence probably depends on the consolidation process of compressible soils induced by the construction of heavy buildings. LOS velocities reach the maximum rate of 40 mm/yr. Another interesting and relevant group of subsidence clusters is situated along Firenze-Prato-Pistoia basin. This group is composed of five clusters covering a total area of 44 km^2 during the first period. The number of PS/DS points forming the clusters decrease along the time, therefore also their areal distribution decreases, reaching 39 km^2 in the third monitored period (October 2014 – April 2018). LOS velocities recorded a little variation of few mm/yr, with maximum subsidence rates decreasing from 21 mm/yr to 18 mm/yr.

Figure 20 shows the temporal evolution of moving areas over Tuscany Region and their classification. The results indicate a homogeneous percentage among geohazard, with the landslides as the most occurring phenomenon, followed by the subsidence and the geothermal activity. On the other hand, the most common triggering cause for TPGA is subsidence (47%), followed by landslides (21%) and geothermal activity (14%). The percentage of landslides is reduced by more than a half considering the first and the last monitoring period, whereas the percentage of subsidence-related clusters is doubled. This is due to three principal factors: i) in general, the subsidence has a deformation velocity more linear and regular than a movement caused by a landslide, and with a lower spatial and temporal variability; ii) subsidence phenomena are located in flat areas, which are not subjected to typical radar distortions, such as foreshortening, layover and shadowing. Sometimes from a slope, on the basis of its aspect, it can be easier extract data in ascending geometry, rather than in descending geometry and vice versa, with differences in terms of PS/DS density and velocity; iii) landslide phenomena are connected with rainfall, therefore during periods with low rainfall rates, the landslide velocity could fall below the used threshold.

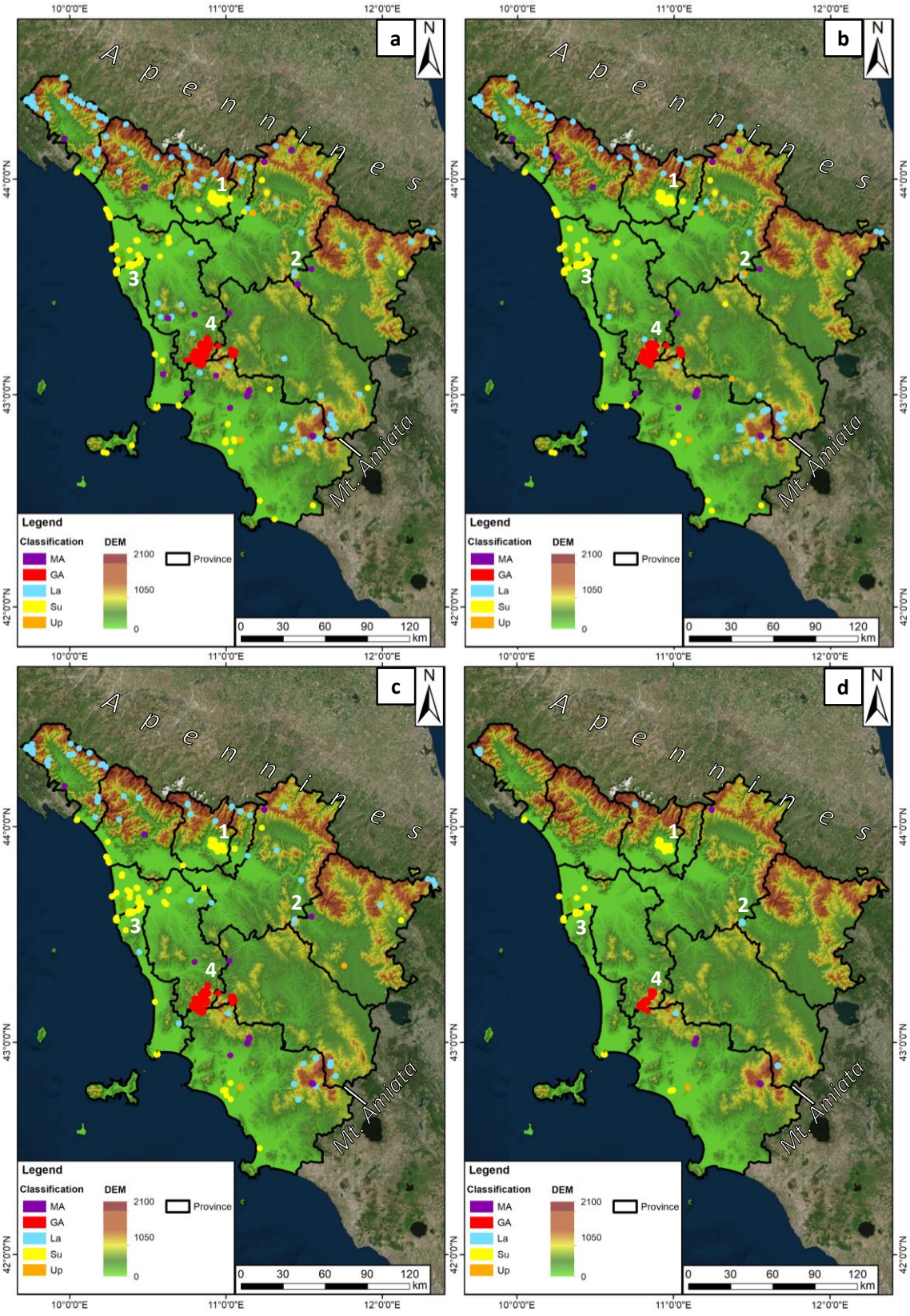

Figure 19 - Cluster classification and TGPA maps. a): 1° period (October 2014 – April 2017); b): 2° period (October 2014 – October 2017); c): 3° period (October 2014 – April 2018); d): Temporal and Geometric Persistent Areas. GA: Geothermal Activity; La: Landslide; Su: Subsidence; MA: Mining Activity; Up: Uplift. 1): Firenze-Prato-Pistoia basin; 2) Cavriglia's landslide; 3): Livorno freight terminal; 4): Larderello-Travale area.

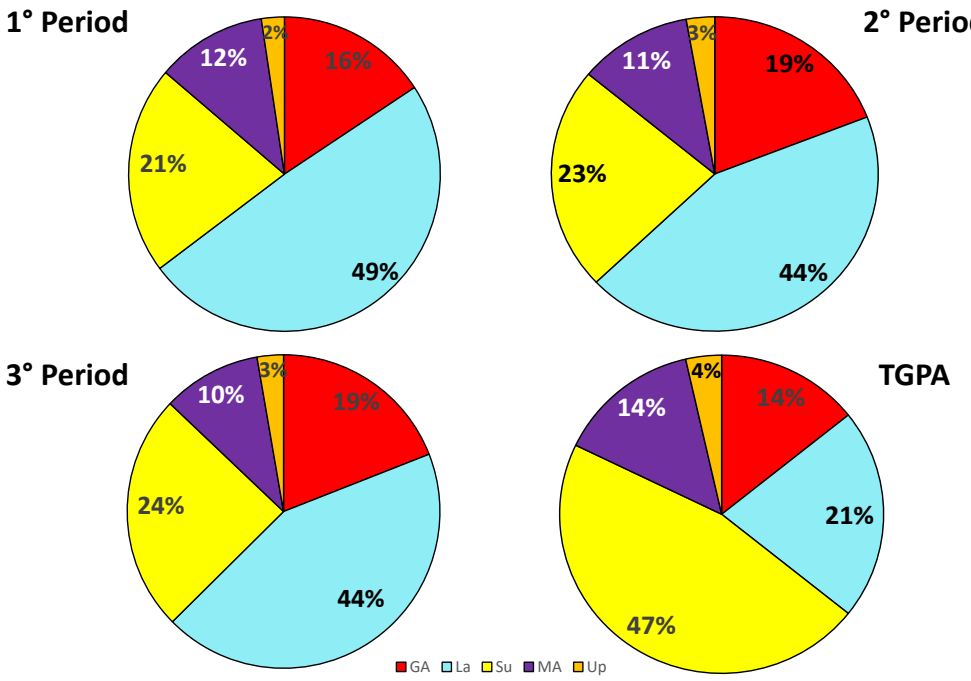

Figure 20 - Classification statistics of the clusters in TR during the 1° period (October 2014 – April 2017), 2° period (October 2014 – October 2017), 3° period (October 2014 – April 2018) and Temporally and Geometric Persistent Areas. GA: Geothermal Activity; La: Landslide; Su: Subsidence; MA: Mining Activity; Up: Uplift.

Figure 21 presents an example of TGPA, related to subsidence due to water overexploitation, located in the plain between the cities of Prato and Pistoia, in the central portion of the Firenze-Prato-Pistoia basin. The Firenze-Prato-Pistoia basin has an extension of approximately 824 km2 and a mean elevation of ca. 50 m a.s.l. The plain is crossed by the Ombrone creek in the Pistoia area, the Bisenzio River in the Prato province and the Arno River in the Florence area. The plain has an oblong shape in the NW–SE direction and is approximately 35 km wide and 100 km long (Del Soldato et al., 2018b). By geological point of view, this plain is an intermountain valley formed during the late extensional phase of the formation of the northern Apennines and later filled with alluvial deposits, reaching a thickness of hundreds of metres. The shape is defined by normal faults in the NO flank, forming a semi-graben filled by an important thickness of marshy-lacustrine sediments (Capecchi et al., 1975). The hydrogeological setting of the area is characterised by several confined aquifers situated at different depth, composed by clay lenses where water is extracted. Such aquifers supply the municipal aqueducts, the textile industries as well as trees and flowers nurseries that characterize the importance of this area. They were overexploited for more than thirty years, creating large subsidence bowl already detected by means of ERS 1/2 and Envisat interferometric products (Colombo et al., 2003; Del Soldato et al., 2018b). The TGPA (12 km²) is composed by an average of 1756 PS/DS in the first period, 1730 for the second one, 1717 for the last one. The velocity analysis shows that the mean velocity is equal to 10.4mm/yr and the maximum 19,3 mm/yr; for the second one the mean velocity is 10.1 mm/yr and the maximum 21 mm/yr; for the last one a mean velocity of 9,9 mm/yr and the maximum of 17,2 mm/yr. The time series of deformation show a linear and constant motion in the whole investigated period, the series shown in Figure 21 is an example.

Figure 22 shows an example of TGPA related to a landslide motion taken from the municipality of Abbadia San Salvatore located in the Siena province along the eastern flank of the Amiata Mountain (1780 a.s.l.), a

Middle-Late Pleistocene volcano. By a geological point of view, Amiata Mountain is characterized by a superimposition of different tectono-stratigraphic units, through the action of low-angle normal faults of different ages. The geological setting is subdivided from the bottom to the top: the Tuscan Nappe succession (Late Triassic), the Ligurian Complex (Middle Jurassic – Olocene), the sediments of Radicofani basin (Early-Middle Pliocene), the magmatic complex (300 ka) Calamai et al. (1970); Gianelli et al. (1988); Brogi (2007). According to the study of Coltorti et al. (2009), Abbadia San Salvatore and the eastern flank of the Volcano are characterized by a deep-seated gravitational slope deformation (DSGSD), subdivided in a deeper part with an activity difficult to verify and an active shallower part. The TGPA (500 m^2), located in the northern part of the municipality, is composed by 99 PS/DS in the first period, whit a maximum velocity of 24 mm/yr and a mean velocity of 14 mm/yr. The second period has a total of 79 PS/DS with a maximum velocity 19 mm/yr and a mean velocity of 12.1 mm/yr. The last one has 67 PS/DS, with a maximum velocity of 18 mm/yr and a mean velocity of 11.7 mm/yr. The motion is linear through the whole monitored period in both orbits, as testified by the time series shown Figure 22.

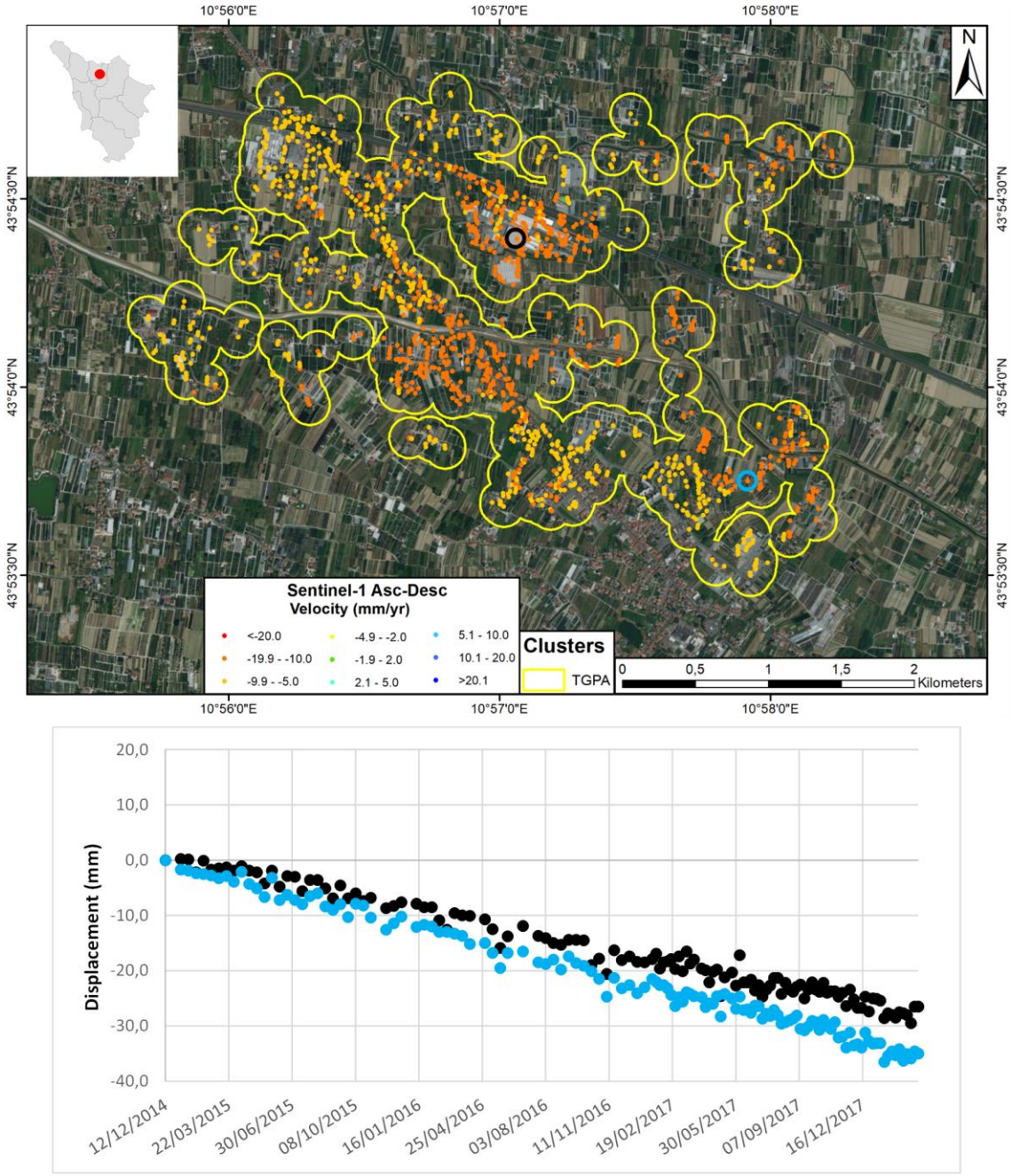

Figure 21 - Example of TGPA in Pistoia - Prato - Firenze basin affected by subsidence phenomena. The PS/DS data correspond to the period from October 2014 to April 2018. The black, blue, green and red circles indicate the PS points from which time series were extracted.

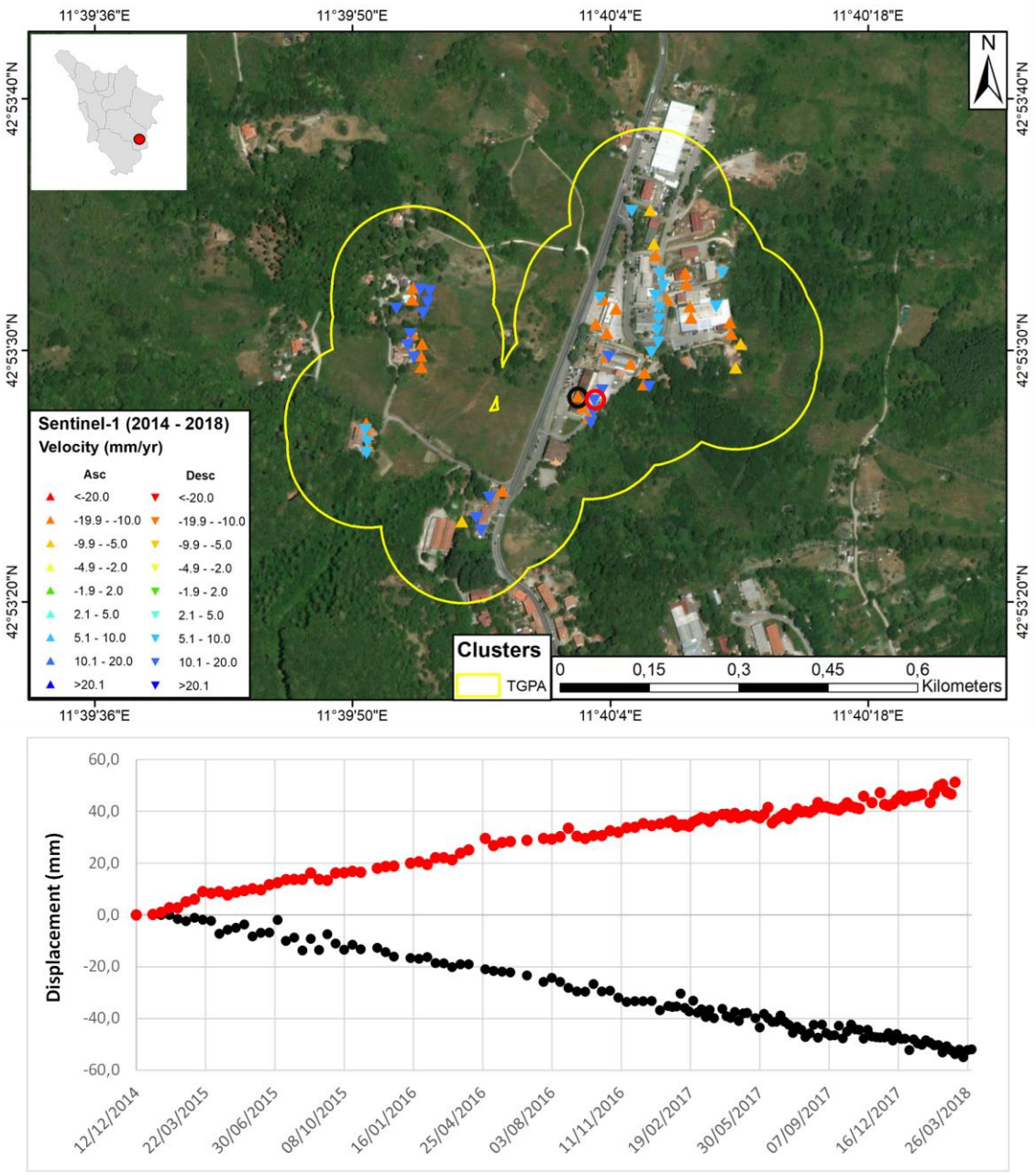

Figure 22 - Example of TGPA Abbadia San Salvatore (SI) affected by landslides phenomena. The PS/DS data correspond to the period from October 2014 to April 2018. The black and the red circles indicate the PS points from which time series were extracted.

6.1.3 Update of the landslide's state of activity

The cluster database can be a reliable tool for the checking landslide's State of Activity (SoA). In Figure 23a the municipalities map is shown, classified on the basis of the Landslides Activity Index (LAI), which is the ratio between the number of active landslides and the total number of landslides, in order to highlight the municipalities with the higher critical level. Figure 23b shows the municipalities where the landslide's state of activity is changed, and where new landslides are found thanks to the analysis of Sentinel-1 data. In 50 municipalities at least one landslide changed its SoA with respect to the IFFI database (already updated by

means of ERS 1/2 and Envisat data), (Rosi et al., 2017) and 12 of these register the presence of potential "new detected" landslides. A total of 197 landslides have been updated from "dormant" to "stable".

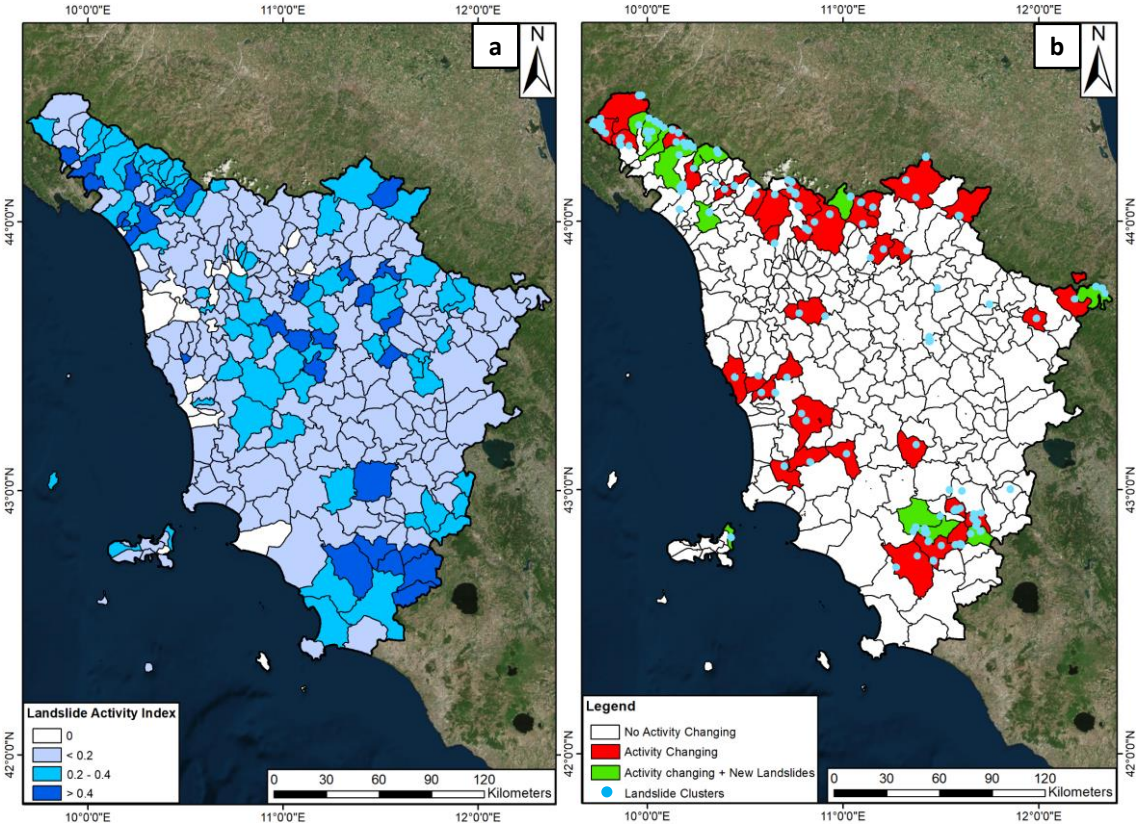

Figure 23 - a): shows the municipalities classified based on Landslide Activity Index. b): shows in red the municipalities where the landslides changed their state of activity in "active" and, in green, if there are also new landslides in municipalities' territories.

6.2 Saline di Volterra

As previously said in chapter 4.2, subsidence is one of the main environmental impacts of the mining activity in Saline di Volterra. Sinkholes are the clearest evidence of this process. So, in order to better understand the evolution of these phenomena an aerial orthophotos are exploited to create a multi-temporal inventory of sinkholes occurrence for the two target areas. Digital orthophotos were made available through the web map service of the Tuscany Region (http://www502.regione.toscana.it/geoscopio/servizi/wms/OFC.htm). Sinkholes were manually mapped using a database of 9 orthophotos acquired in different years, i.e. ranging between 1954 to 2018 (Table 5).

Year	Nominal scale	Image acquisition	Data owner
1954	1:10’000	Italian Aeronautical Group (GAI)	Italian Geographic Military Institute (IGM)
1978	1:10’000	Rossi Brescia Aerophotogrammetry	Tuscany Region
1988	1:10’000	CGR Parma	Tuscany Region
1999	1:10’000	CGR Parma	Agricultural Payments Agency (AGEA)
2003	1:10’000	CGR Parma	Agricultural Payments Agency (AGEA)
2007	1:10’000	BLOM-C.G.R.	BLOM-C.G.R.
2010	1:10’000	Rossi Brescia Aerophotogrammetry	Agricultural Payments Agency (AGEA)
2013	1:10’000	BLOM-C.G.R.	Agricultural Payments Agency (AGEA)
2018	1:5’000	BLOM-C.G.R.	Agricultural Payments Agency (AGEA)

Table 5 – Digital orthophotos used to create the multi-temporal sinkhole database.

Figure 24 presents the results of the orthophoto analysis for the mining concessions of Buriano-Casanova (Figure 24A) and Poppiano-Volterra (Figure 24B). It is worth noting that the definition of the sinkhole contours can be affected by the quality of the oldest images and by the not perfect alignment of some of the WMS services used. This is acceptable since the contours are only used to testify the surface effects of the mining activity.

The total number of mapped sinkholes is 105, with a maximum of 22 and 19 phenomena for the periods 1954-1978 and 1978-1988, respectively. The age of the sinkholes is clearly connected to the activity of the salt dissolution wells. Buriano-Casanova was the first oldest area where the mining activity took place; thus, it is the area where the oldest sinkholes are recorded. On the contrary, Poppiano-Volterra is the newest most recent concession to be exploited for salt extraction. As said before, salt dissolution mining began in 1910 and, until 1978, it was mainly localized in the south-western sector of the Buriano concession. Then, the mining activity expanded to the north, involving the Casanova concession as well. In Poppiano-Volterra a small sector of the Volterra concession was active already before 1978. The expansion of the mining activity to the Poppiano concession took place at the beginning of the 2000s. The oldest sector seems to be nowadays inactive, as testified by the migration of the sinkhole occurrence in the two areas of interest.

The raise and decrease of the number of sinkholes for comparable time periods, e.g. 1978-1988 and 1988-1999 or 2007-2010 and 2010-2013, is probably related to different rates of extraction. Of course, the development of sinkholes is not instantaneous and there can be a lag time of years between their formation and the mining exploration of a salt level in a certain area. Moreover, considering the fact that not the entire water pumped underground is extracted, the dissolution of the underground holes and chambers can continue for years (Warren, 2016).

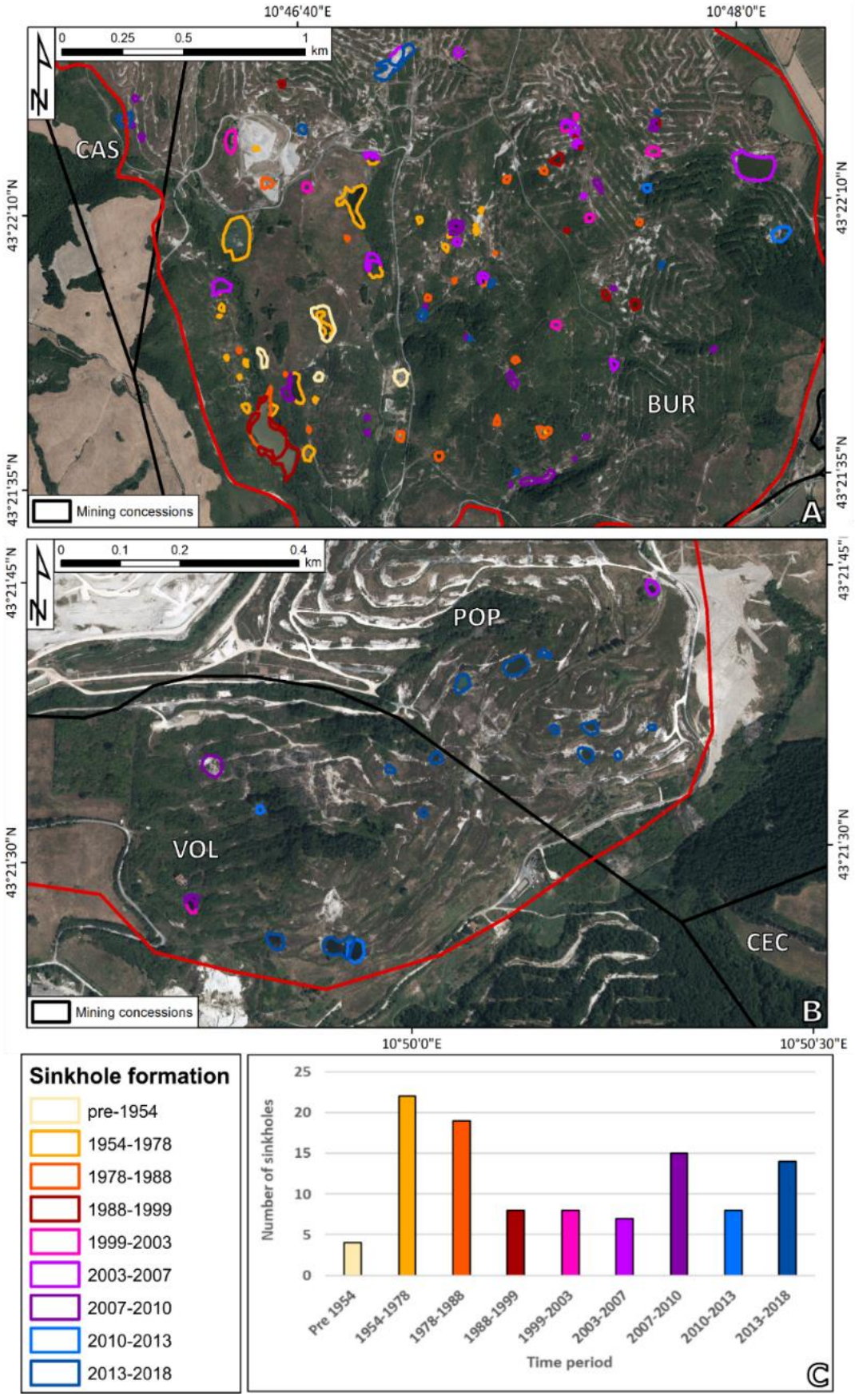

Figure 24 – Sinkholes catalogue for the mining concessions of Buriano-Casanova (A) and Poppiano-Volterra (B). The background image is an AGEA 2018 orthophoto (Table 5). The distribution of boreholes for temporal periods is presented in inset C. Sinkholes with contour variations are counted as their first appearance.

The obtained deformation map is presented in Figure 25. A total of ~24'0000 points cover the mining area of Saline di Volterra with an average density of ~800 MP/km^2. This high density is due to the fact that the thresholding applied during the InSAR processing was maintained low enough to maximize the MP coverage, but guaranteeing the reliability of the results within the two target areas, where the sinkholes are present and where the highest deformation rates are likely to be found. The coherence threshold was 0.35. This implies to have a noisier deformation map outside of the high displacement areas. This is acceptable since the targets of this paper are exactly these "fast" moving pixels.

The deformation map is classified on the basis of the average velocity values, expressed in mm/yr. A stability threshold of ±20 mm/yr was defined to highlight the subsidence bowls within the two mining areas. This threshold is defined depending on the standard deviation of the velocities, here equal to 2.5 times such value. A classical red-green-blue scale bar is used to classify the deformation map; yellow to dark red points refer to movements away from the sensor with negative sign, light blue points refer to movements through the sensor whereas green points fall within the stability threshold. All the measurements are referred to the Line of Sight (LOS) and are differential values, i.e. referred to a reference point assumed as stable. The reference point was selected in the urban area of Volterra in correspondence of the main road crossing the hamlet, where the oldest edifices are built. To the knowledge of the authors, the area is stable as confirmed also by other interferometric data available for the whole Tuscany Region (https://geoportale.lamma.rete.toscana.it/difesa_suolo/#/viewer/openlayers/326 and Raspini et al., 2018).

The deformation map clearly highlights the presence of several subsidence bowls within the contours of the two areas of interest that are part of the mining concessions around Saline di Volterra. Some of the bowl reach in their central portion LOS velocities higher than -200 mm/yr. The characterization of the two mining areas, Buriano-Casanova and Poppiano-Volterra, is presented in the following chapters. It is worth noting that there are some other moving areas outside the mining areas potentially linked to the motion of complex landslides and small earthflows, which characterize the clayey slopes around Volterra (Bianchini et al., 2017).

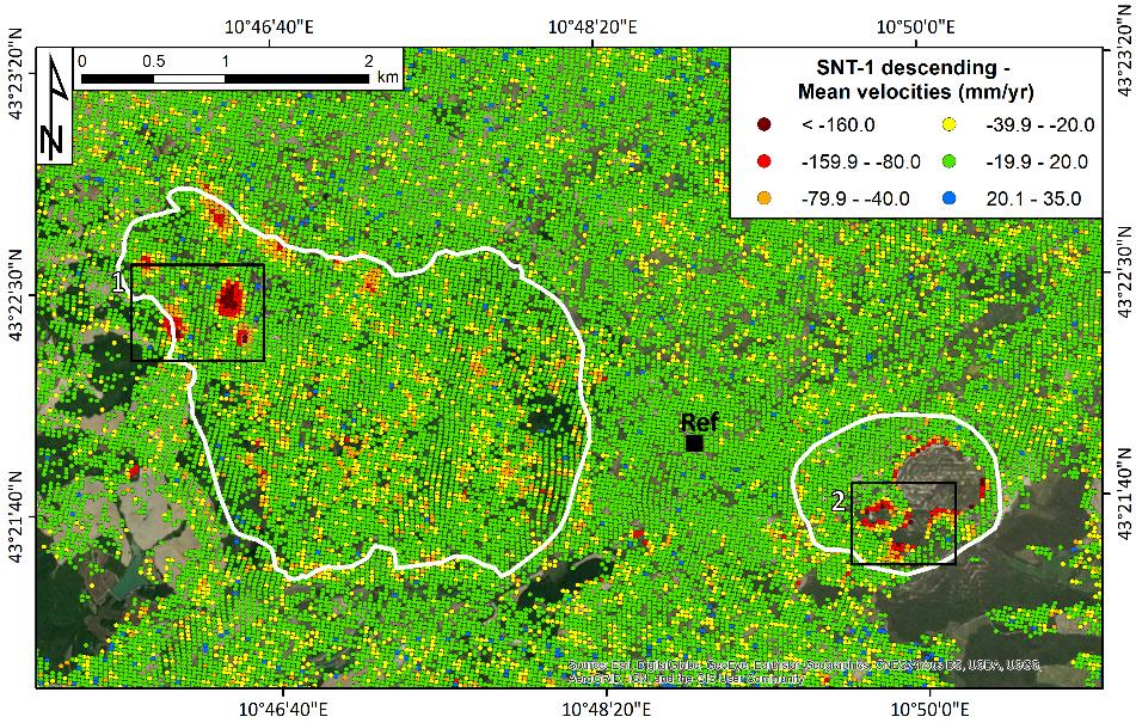

Figure 25 - Sentinel-1-derived deformation map for the area of interest. The black dot is the reference point, located in the stable area of the Saline di Volterra city. The white contours are the two target areas. The two black square represent the two areas with the highest deformation rates (1, Buriano-Casanova, part of the Buriano deformation area; 2, Poppiano-Volterra, part of the Poppiano deformation area) which are the focus of the next two chapters.

6.2.1 Buriano-Casanova mining area

The north-western portion of the Buriano-Casanova mining area presents at least five well-defined subsidence bowls with LOS velocities higher than 80 mm/yr. Among these, the bowl A and B (Figure 26) are the ones with the highest deformation rates, up to -250 and -230 mm/yr, respectively. This implies that the two subsidence bowls reach in their central portion an accumulated displacement higher than 500 mm in a period a little longer than two years.

The subsidence bowls are located in the most recent mining expansion of this area, at the border between the Buriano and Casanova concessions, where some of the most recent sinkholes are found (Figure 24). Bowls A and B occupy a surface of ~0.04 km^2 and ~0.03 km^2, respectively. In the first case, the orthophotographic analysis did not highlight the presence of any formed sinkholes, whereas in the area of bowl B a sinkhole is evident from the 2013' orthophoto and it is expanding in the last years (see Figure 26b).

Figure 26c shows the time series of deformation for the bowl A. The time series extracted from the center of the bowl (point 1) has a purely linear trend with minor oscillations of the displacement values. The deformation rate for point 1 is equal to -210 mm/yr. Point 2 is located in the southern border of the subsidence bowl and it is characterized by a lower deformation rate (-122 mm/yr), as expected moving away from the center of the subsidence area. The time series is again linear with a minor acceleration event between May and July 2018 (point 2). During this period, the velocity change is ~150 mm/yr. This behavior is shared by several points in the same sector of the bowl. The northern portion of the bowl presents the lowest velocities, up to 40 mm/yr and linear trends with no significant accelerations (point 3).

Figure 26d presents the time series of deformation for the bowl B. The time series analysis are focused on the points around the mapped sinkholes. Points 4 and 5 are extracted from the southern and northern border of the sinkhole, respectively. The time series referred to point 4 shows a linear trend with a strong acceleration between August and November 2017, with LOS velocities passing from ~-200 mm/yr to ~-420 mm/yr. Such acceleration is not evident in the time series of point 5 whose deformation rate (-137 mm/yr) is constant over time with minor order oscillations. It is interesting to notice that moving away from the sinkhole the time series tend to stabilize in the last 6 months (point 6 is an example of this trend).

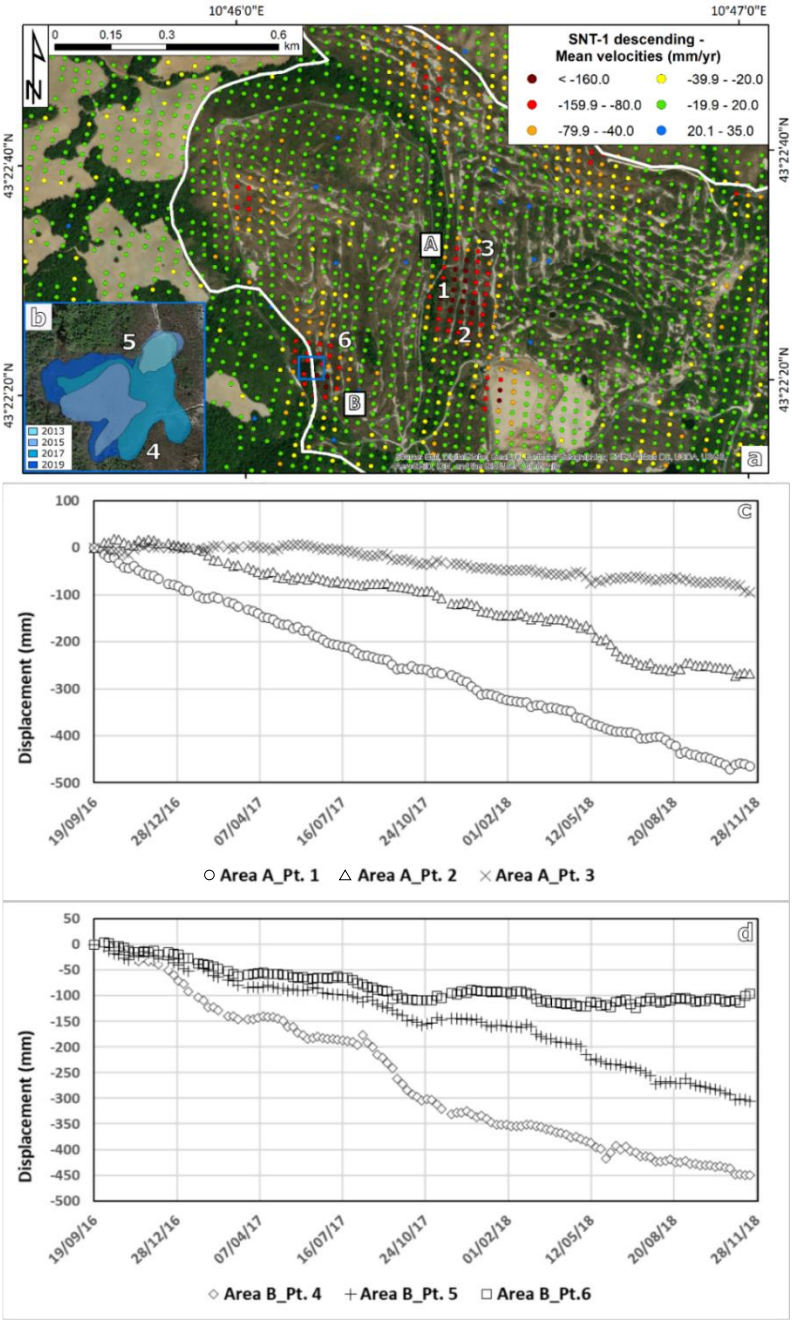

Figure 26 – Deformation map for the high deformation area of Buriano-Casanova. A and B are the two subsidence bowls with the highest deformation rates: the first with no signs of sinkhole development, the second with a well-developed sinkhole expanding over time Numbers 1 to 6 indicate areas where the time series of insets (c) and (d) have been extracted.

6.2.2 Poppiano-Volterra mining area

The central portion of the Poppiano-Volterra area presents a distribution of the measurement points within the subsidence bowls slightly different than the previous example. In fact, only the external border of the moving areas is well-defined. In fact, the loss of coherence is so strong that a large part of what it is supposed to be the main subsidence area is not covered by any measurement point, even considering the specific data processing applied. The loss of coherence can have a triple interpretation: i) land cover characteristics; ii) high surface changes between the images of the stack and iii) presence of fast motions that create decorrelation. It is worth noting that the land cover is basically the same as the Buriano-Casanova mining concession and the surface changes induced by salt dissolution mining are not big as in the case of e.g. open pit mining. Considering this, the hypothesis of the presence of fast deformation rates exceeding the ~2 mm/day unwrapping threshold seems the most reasonable.

Due to the lack of measurement points, the subsidence bowls are less defined as it is for the Buriano-Casanova area. One clear bowl can be identified in the area of point 1 (Figure 27a). The low point density prevents further visual interpretation of the deformation map. In general terms, LOS velocities greatly increase forward the low coherence areas, passing from less than ±10 mm/yr to more than 100 mm/yr, in some cases exceeding -220 mm/yr.

The time series of deformation extracted for the points with the highest deformation rates along the internal border of the high deformation areas are presented in Figure 27b (points 1,2,4,5 and 6). All these time series highlight an acceleration with different magnitudes in the last months of the monitored period. The breaking point is located between June and August 2018.

Point 1 is the one showing the most evident acceleration. Although having already an accumulated deformation of 250 mm in less than 2 years (LOS velocity of -152 mm/yr), this point triplicated its deformation trend after the beginning of June 2018. In the second part of the time series the accumulated deformation is equal to 220 mm in a ~6 months period (the estimated LOS velocity is equal to ~450 mm/yr). Such acceleration is not as evident in the other time series, but the velocity change is still relevant, ranging between 120 and 180 mm/yr. The behavior of the time series in the last six months supports the previous hypothesis, i.e. the presence of very high deformation rates where measurement points could not be obtained.

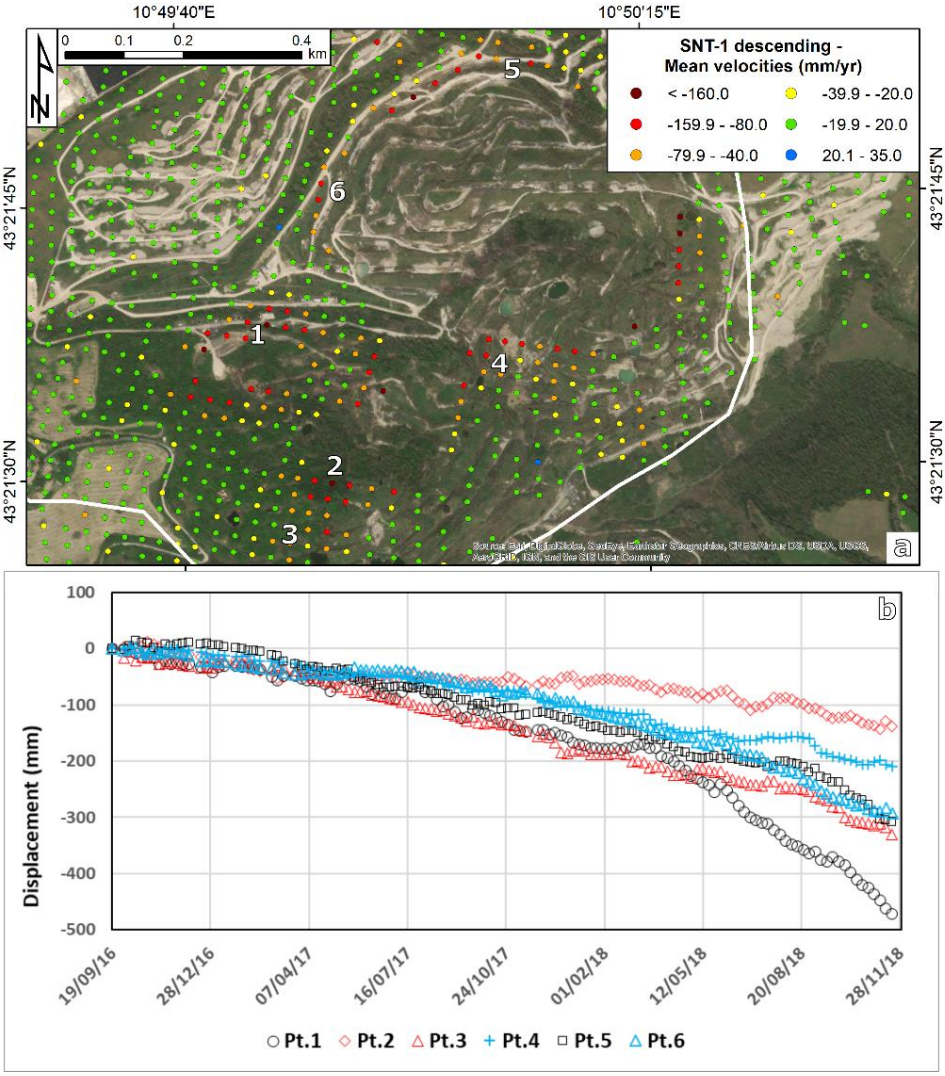

Figure 27 – (a) Deformation map for the mining area of Poppiano-Volterra. Numbers 1 to 6 indicate areas where the time series of inset (b) have been extracted. The background image of inset (a) is an ESRI World Image.

6.2.3 Sinkhole-scale analysis of the deformation map

An additional analysis is performed at sinkhole scale. The deformation map is filtered by using the polygons of the 105 sinkholes mapped in the areas of Buriano-Casanova and Poppiano-Volterra. A 10 m buff is created around each polygon to define an area of influence. The average, maximum, minimum and standard deviation values of the LOS velocities of the measurement points within each sinkhole are extracted. This information is available for more than half of the sinkholes, 58 in the Buriano-Casanova area and 9 in the Poppiano-Volterra concession. For the remaining sinkholes no measurement points are available.

The analysis of the velocity values allows discovering that sixty percent of the sinkholes (including the areas of influence) present average velocities within the ±10 mm/yr interval. Twenty-eight percent of the sinkholes have average deformation rates lower than -20 mm/yr. Only 10% of the sinkholes show average velocities faster than -40 mm/yr; 3 of them exceed -80 mm/yr.

In order to assist the interpretation of the results, the pure evaluation of the average velocity values is associated to the information regarding the age of formation of the sinkholes. The results are presented in Figure 28. The box plot is showing the median, minimum and maximum values of the LOS velocities of all the

measurement points included in the sinkholes of each temporal interval. The graph shows an evident increase of the deformation rates for the most recent sinkholes. The oldest temporal intervals (before 1988) show very similar velocity distributions, with median values around -10 mm/yr. LOS velocities regularly increase until the period 2003-2010, when a strong increase of the maximum velocities is recorded.

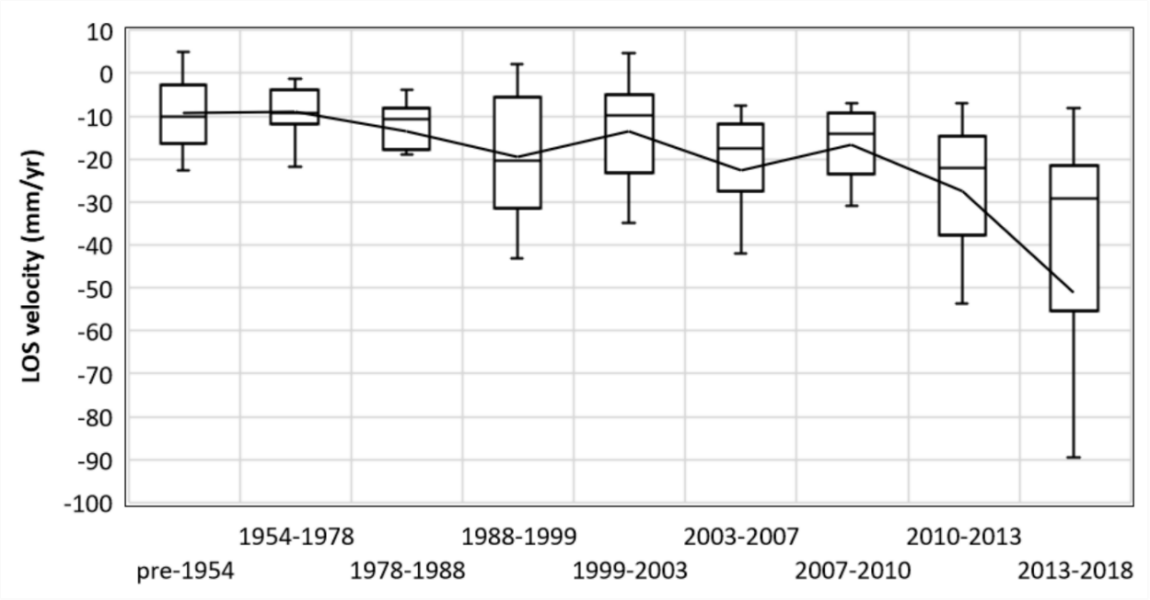

Figure 28 – Box plot showing the variability of the velocity values depending on the time of formation of the sinkholes in the mining concession around Saline di Volterra. The straight line represents the mean value, the stroke within each box plot the median value.

6.3 Valle D'Aosta region

The CRI results for the entire VdA Region show how the PS distribution will be strongly affected by both local morphology and land use.

Depending on the orbit, eastward or westward valleys could be partially visible or incomplete shadowing, this is especially evident along the tributaries valleys of the Dora Baltea (Figure 29). These "low PS density" areas are represented by values of the CRI below 20, covering around the 25% of the total VdA territory. It is worth noting that along these valleys is quite rare to obtain a shadowing zone in both orbits, the coverage of at least one orbit is most of the time guaranteed. Values of CRI near zero are also registered where LUI tends to zero, i.e. in areas with perennial ice coverage or in water basins. This is evident along the north-north-western border of the VdA where the largest ice sheets are present.

On the other hand, CRI values higher than 60 indicate a high to very high radar visibility. The 22% of the regional territory records these values. Very high CRI values are recorded only along the flat Dora Baltea valley where the largest urban areas are present; here the density of PS measurements depends only on the type of surface. It is recalled that the CRI index depends only on the land use when the effect of the topography is low, i.e. when RI is above 50. High values of CRI are found along favourably oriented valleys, depending on the acquisition geometry, and at high altitudes, where the vegetation is sparse or absent and debris or outcropping rocks dominate the landscape. Here the PS density can be quite high, but the quality of the derived time series of deformation can be affected by the snow coverage for long periods (Cignetti et al., 2016).

The 33% of the Region is considered as “medium visibility”. Thus, the number of PS points is related not only to topography or land use variations, but also to the type of processing used (Notti et al., 2014).

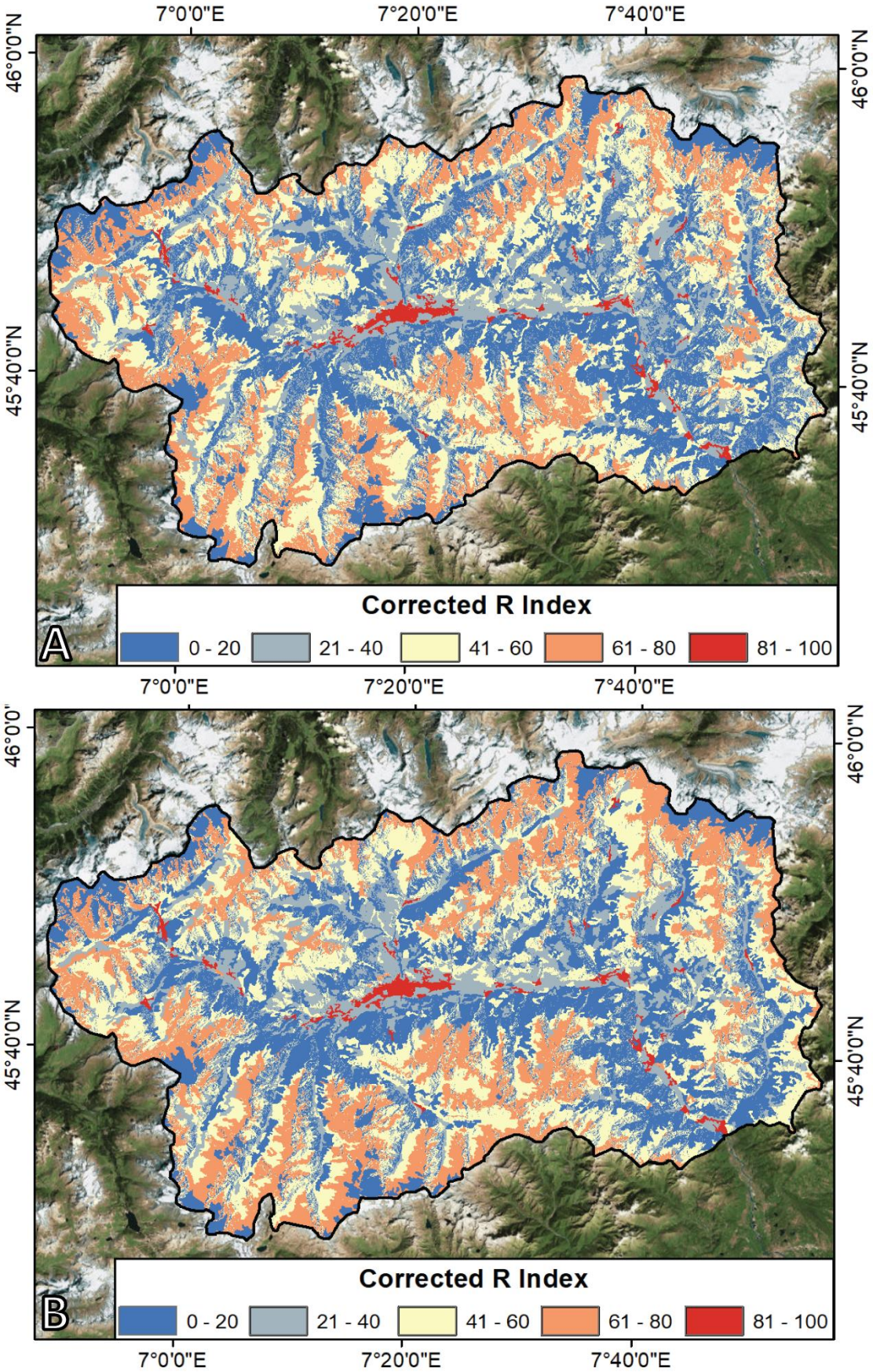

Figure 29 – CRI maps for the Valle d'Aosta Region. A) and B) are referred to the ascending and descending orbits, respectively.

6.3.1 Deformation maps

For the deformarion maps there were exploited Sentinel-1A and 1B radar images acquired in C-band (wavelength equal to 5.55 cm) in ascending (track 88) and descending (track 66) orbits and their derived information (or products). Both data stacks are composed by 130 images reaching the end of February 2018, starting from October 2014 for the ascending orbit and from November 2014 for the descending orbit. Considering the high number of images composing the datasets, the estimation of the displacements rates easily reaches a precision higher than 1 mm/yr (Raspini et al., 2018).

Despite the challenging environment, the SqueeSAR processing of Sentinel-1 images gives good results in terms of both density of points and noise of single measurements. The outputs of the interferometric investigation are shown in

Figure *30*. Almost 360,000 points for each orbit were found, obtaining a mean density of around 100 PS/km^2. The density is maximum along the Dora Baltea valley, in correspondence of the Aosta city, whereas it is minimum along tributaries valleys where shadowing/layover effects are possible (as shown by CRI maps, Figure 29). No PS are registered where high vegetation or the presence of ice strongly limited the coherence of the radar images, as predicted by the CRI (Figure 29).

Considering a stability threshold of 3 mm/yr, equal to 1.5 times the standard deviation of the estimated velocity values of the datasets, the 94.4% of the PS in ascending orbit and the 92.9% in descending orbit are considered as stable (

Figure 30). This fact means either that the PS points do not record any ground motion or that the deformation rate is so small to be distinguishable from the noise without a detailed analysis.

Significant clusters of moving points outside the 3 mm/yr threshold have been anyway registered, sometimes involving entire slope sectors. It is interesting to notice that in some cases the terrain morphology allows obtaining consistent results in both orbits. This is evident considering some well-known large slope deformations such as the Punta Chaligne, Torgnon, Cervinia and Emarese DSGSDs (areas 1 to 4 in

Figure *30*A and B). All these large slope phenomena records velocities outside the stability threshold, ranging between 5 and 10 mm/yr, as expected for this type of movements (Crosta et al., 2013).

The effects of slope aspect can be seen by the results obtained along N-S oriented valleys in the south-western portion of VdA. Along these valleys deformation rates above the stability threshold, up to 20-30 mm/yr, are usually recorded in one single orbit. This is the case of the left flanks of Valgrisenche and Cogne Valleys in ascending orbit (points 5 and 6 in

Figure 30A) and of the right sides of Rhêmes and Valsavarenche Valleys (points 7 and 8 in
Figure 30B).

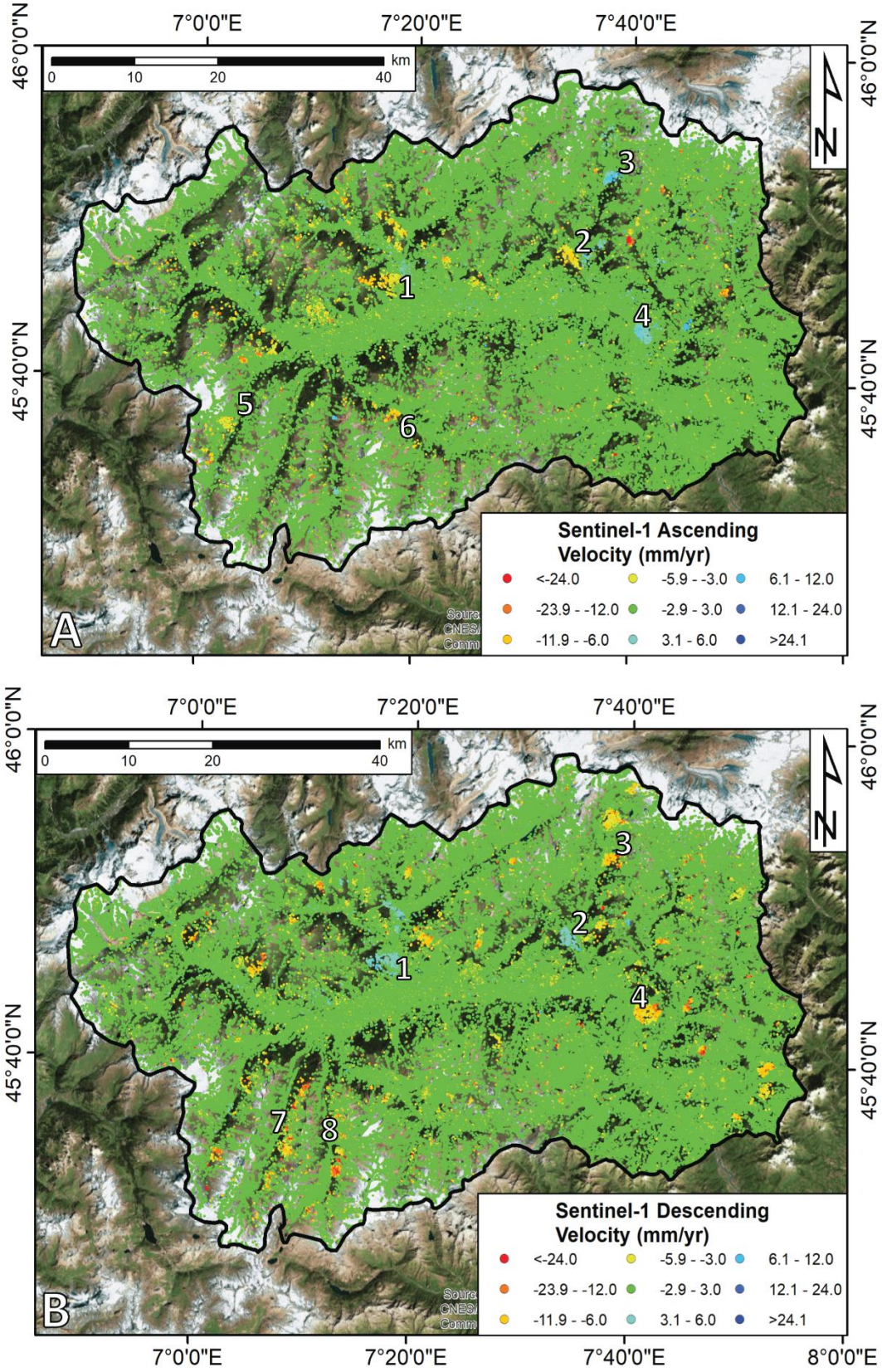

Figure 30 – Deformation maps, derived using the SqueeSAR algorithm, for the VdA Region. A) ascending orbit results, B) descending orbit results. 1) Punta Chaligne DSGSD; 2) Torgnon DSGSD; 3) Cervinia DSGSD; 4) Emarese DSGSD; 5) Valgrisenche Valley; 6) Cogne Valley; 7) Rhêmes Valley; 8) Valsavarenche Valley. The maps are overlaid on a Bing Aerial image.

6.3.2 Moving areas mapping

The methodology explained in the Chapter 5.3 allows extracting a total of 277 moving areas in the test site (Figure 31), 115 for ascending orbit, with mean velocity values ranging from -39 mm/yr to 33 mm/yr, and 152 for descending orbit (the mean velocity range is equal to -60 mm/yr - +18 mm/yr).

Moving areas are quite widespread in VdA, with two maximum density sectors along Rhêmes and Cogne valleys (see Figure 30A and Figure 30B for the localization). The 71% of VdA municipalities host at least one moving area; the 27% of these municipalities records more than 5 deformation clusters and only the 9% more than 15 (Figure 31). The 32% of the municipalities registered the presence of only one moving area. The maximum number of moving areas (28) are found within the Ayas municipality, located in the north-eastern part of the region (polygon enclosing point 3 of Figure 31).

Considering the radar reliability of the moving areas, the 40% and the 46% of them in ascending and descending orbits, respectively, are considered as "highly reliable" (green in the contingency matrix of Figure 17). This means that both the time series and the measurement of displacement vector are representative of the real movement along the slope. On the other hand, the 6% (ascending orbit) and the 15% (descending orbit) of the clusters obtain a D grade (Figure 17), meaning that the PS time series are noisy or follow a non-linear trend and, because of the terrain morphology, the real displacement vector is strongly underestimated. The percentage for the ascending orbit is the result of a higher weight of the local morphology, with some clusters detected along southward/northward slopes.

The spatial overlapping between moving areas of different orbits is not quite common. This is due to i) slope orientation effects, i.e. velocity variations in the same area considering different orbits and ii) shadowing effects, i.e. impossibility of obtaining data because of the presence of steep morphologies that prevent the identification of PS in one of the two orbits.

Landslides and slope mass wasting phenomena are the main target of this work. Thus, we overlapped the IFFI catalogue with the database of moving areas in both orbits. The 28% and the 38% of the moving areas in ascending and descending orbits, respectively, fall into the contours of already known landslides. Almost half of the moving areas are found in correspondence of debris deposits along steep slopes connected to the recent activity of rock falls. The largest part of these motions is found at high altitude, preferentially above 2,000 m a.s.l. Complex and rotational landslides equally featured the remaining 50% of the landslides. Some of these active deformations are part of large DSGSD; however, they indicate a localized motion not related to an entire flank-scale movement. We found that the 25% of all the moving areas fall into the perimeter of a known DSGSD.

The 10% of the moving areas in ascending orbit (12 in total) fall within the perimeter of a mapped rock glacier, 6 classified as active and 6 as relict. In descending orbit, the percentage reach the 15% (24 moving areas), subdivided into 18 active rock glaciers and 6 relicts. Because of the presence or absence of an active permafrost layer, mean velocity values differ between the two types of rock glaciers. Relict forms are barely above the 10 mm/yr threshold, whereas active rock glaciers reach values three times higher. This difference has been already highlighted by Cignetti et al., 2016 using ERS 1/2 and Envisat interferometric products.

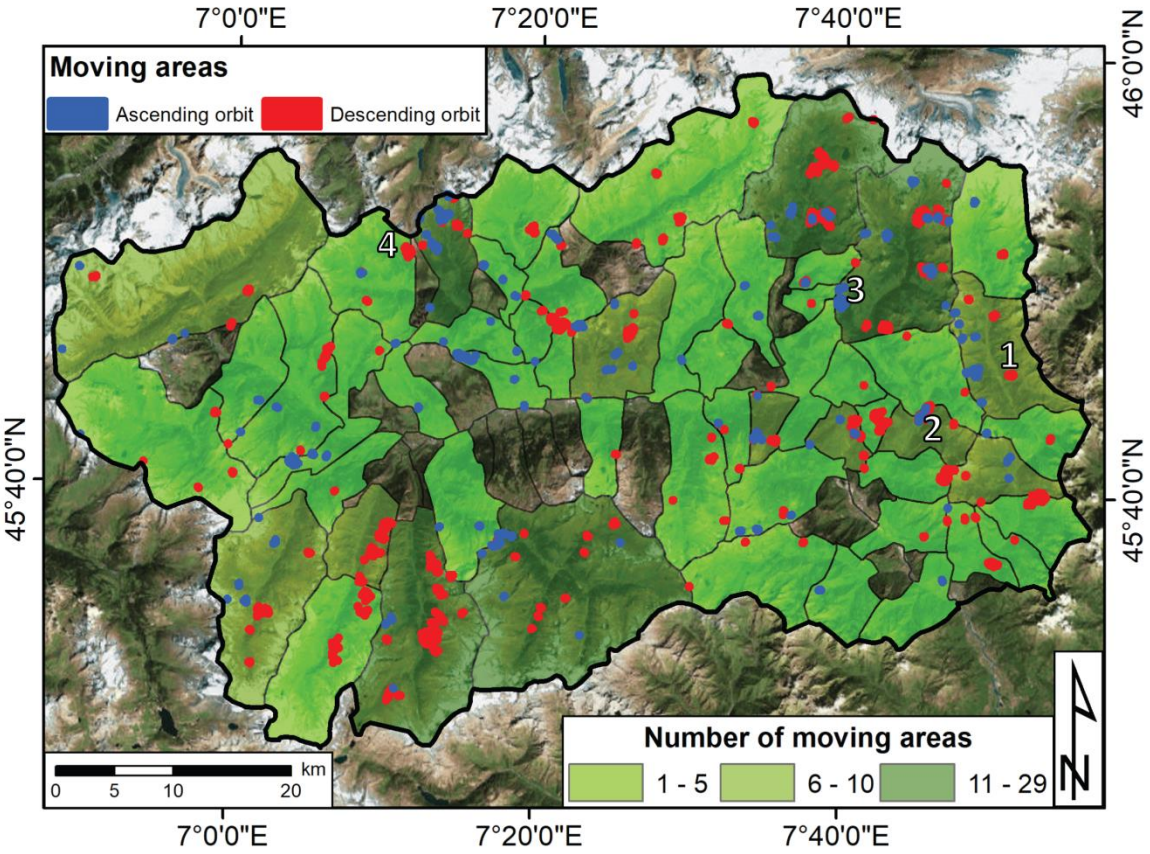

Figure 31 – Moving areas above the 10 mm/yr threshold. The contours represent the VdA municipalities. 1) Bosmatto landslide; 2) Allesaz landslide; 3) Ayas municipality; 4) Saint Rhémy En Bosses municipality. The data are overlaid on a Bing Aerial image.

Figure 32 presents two examples, taken from two valleys located in the north-eastern part of VdA, of moving areas falling within the perimeter of already mapped landslides (IFFI catalogue). The first moving area characterizes a well-known landslide located above the village of Bosmatto in the Gressoney Saint Jean municipality, along the Lys Valley. The landslide is classified as complex (according to Varnes classification) and composed by two landslide bodies that involve both detrital deposits and bedrock. The southern portion of the body is almost completely vegetated, whereas the northern one presents a heterogeneous detrital cover. In October 2000 a debris flows originated from the blocky sector of the Bosmatto landslide was triggered by intense rainfalls, running down the Letze Creek and destroying several private houses, depositing 2-3 m of detrital with rock blocks of maximum estimated volume equal to 103 cubic meters (Luino, 2005). The moving area involves the upper portion of the landslide, where the detrital deposit is found, and registering very high deformation rates, up to 50 mm/yr in the crown area of the landslide. LOS velocities gradually decrease to 15 mm/yr along the central sector of the landslide. This moving area has been only detected in descending orbit because of geometric effects of the slope that strongly reduce the amount of detectable motion (low C index). A time series of deformation for the upper portion of the landslide, where the highest LOS velocities are found, is shown in Figure 32C (black points). The movement is quite regular and linear throughout the monitored period, with noisy data in correspondence of snow seasons; this fact is evident in the last part of the series (between November and February 2018). The entity and temporal evolution is confirmed by levelling data and by GBInSAR (Ground Based Interferometry) measurements (Carlà et al., 2018).

The second example (Figure 32B) is referred to the village of Allesaz, in the Challand Saint Anselme municipality, along the Ayas Valley. The hamlet and its surroundings are affected by large deformation clusters in both orbits. These moving areas coincide with the perimeter of already mapped landslides; the biggest one, that completely involve the Allesaz village, is 1.8 km long and 600 m large, being a complex phenomenon that runs from an altitude of 1800 m a.s.l. to the bottom of the valley, along the Evançon Creek. LOS velocities reach maximum values of -20 mm/yr in descending orbit and 15 mm/yr in ascending orbit in the upper part of the landslide, at an altitude ranging between 1200 and 1300 m a.s.l. This case study is an example of overlapping between moving areas measured in different orbits. Velocities progressively decrease along the landslide, dropping below 15 mm/yr in both orbits. The time series of deformation (Figure 32C, light blue and red points) referred to the upper portion of the landslide show a linear and continuous trend, similar to Bosmatto. The noisy periods are here limited and less evident; this is due to a climatic evidence, in fact the Bosmatto landslide is located at highest altitude (crown area at around 2,700 m a.s.l.), thus characterized by more persistent snow cover during winters.

Figure 33 shows two examples of moving areas recorded outside of known landslide boundaries, along slopes already affected by mapped phenomena. The first case study is taken from the Ayas Valley, in the homonymous municipality (Figure 33A). This area is characterized by three moving areas; the first one, the largest (area 1 in Figure 33A), is composed by 45 PS points located between Col Tantanè and Barmasc, at a height ranging from 2000 to 2600 m a.s.l. The other two areas (2 and 3 in Figure 33A), smaller and composed by 4 PS each, are located western than Col Tantanè, at an altitude of 2500 -2600 m a.s.l. LOS velocities of the area 1 range between -42 mm/yr in the northern portion and -15 mm/yr along its south-western border. This moving area is located between two known landslides, along a steep slope with widespread detrital deposits. Considering local morphology and satellite data, we hypothesized the contour of the possible upper limit of the unstable area, as shown by the white dashed line in Figure 33A. The time series of deformation for the area 1 shows that the movement is constant over time (red points in Figure 33C), with noisy periods related to the presence of snow, as shown before (Figure 32C). Area 2 and 3 have similar average LOS velocities (around -15 mm/yr) and are placed near the upper limit of a mapped landslide, classified as “rotational slide”. Here the deformation recorded could suggest i) a retrogression of the landslide already included in the IFFI catalogue (Figure 33A) or ii) the motion of small unstable debris masses on top of the steep slope, not connected to the activity of the mapped phenomenon.

In Figure 33B a second example of moving area that does not intersect landslide inventories is presented. The deformation cluster is located in the Saint Rhémy En Bosses municipality, along the Cote de Barasson at an altitude between 1,900 and 2,200 m.a.s.l. The cluster is composed by 60 PS points with velocities ranging between -30 and -12 mm/yr with time series of deformation showing a linear trend with little winter oscillations and a slight deceleration between June and November 2015 (blue points in Figure 33C). This part of the Saint Rhémy municipality is affected by two large complex landslides threatening the access to one of the main connections between Italy and Switzerland, the Gran San Bernardo (GSB) tunnel. Thanks to the satellite data it is possible to mark the contour of a moving area that, if completely mobilized, could hazard the state road that in the hamlet of Thoules, 300 m below the cluster of deformation, connects the GSB tunnel access road to the local road network.

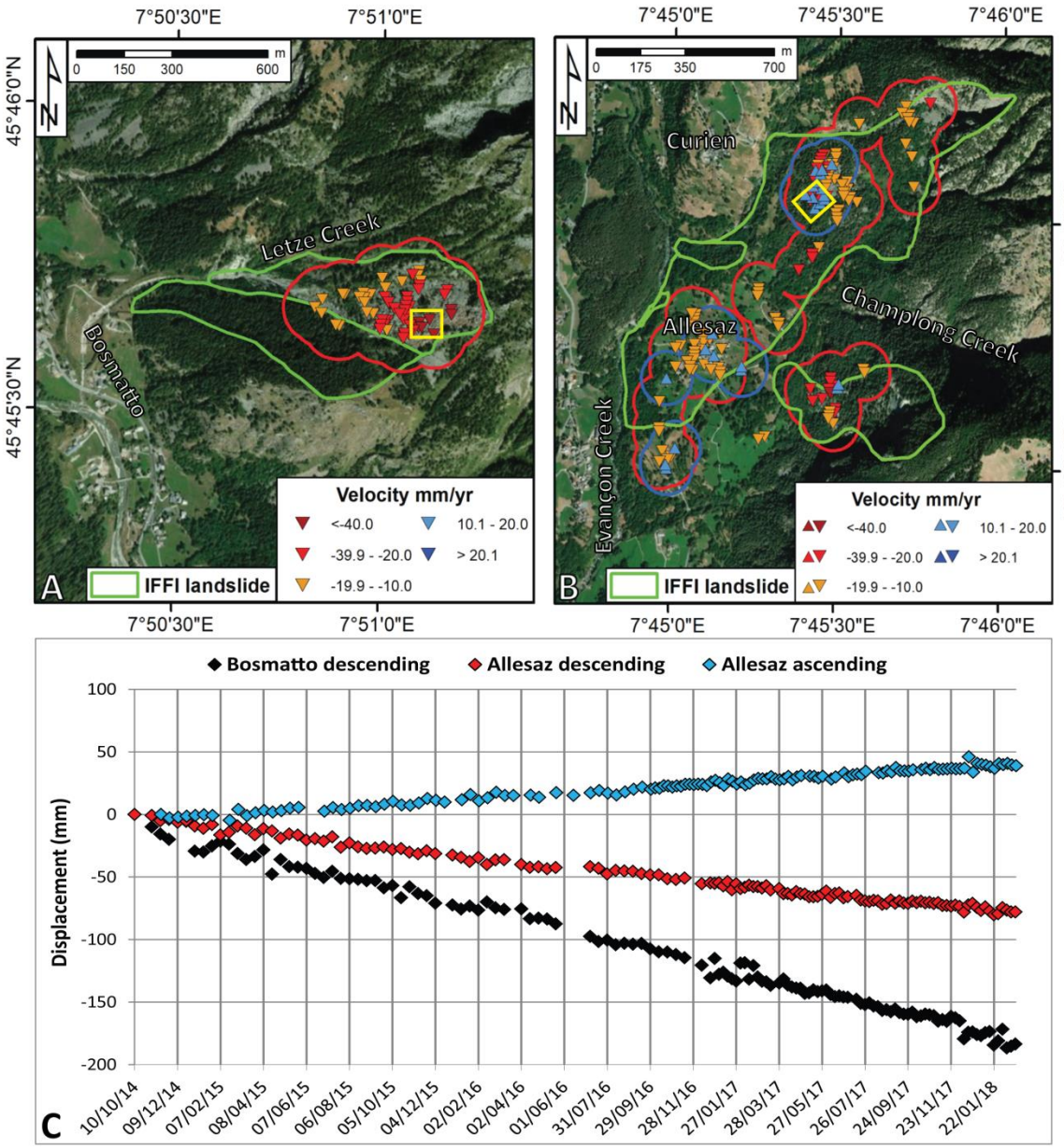

Figure 32 - Moving areas falling within the contour of already mapped landslides. The Sentinel-1-derived PS points are represented as triangles with downward orientation if the orbit is descending, upward if it is ascending. Red and blue contours represent moving areas in descending and ascending orbits, respectively. A) Bosmatto landslide; B) Allesaz landslides; C) average time series of deformation for the sectors indicated by yellow rectangles.

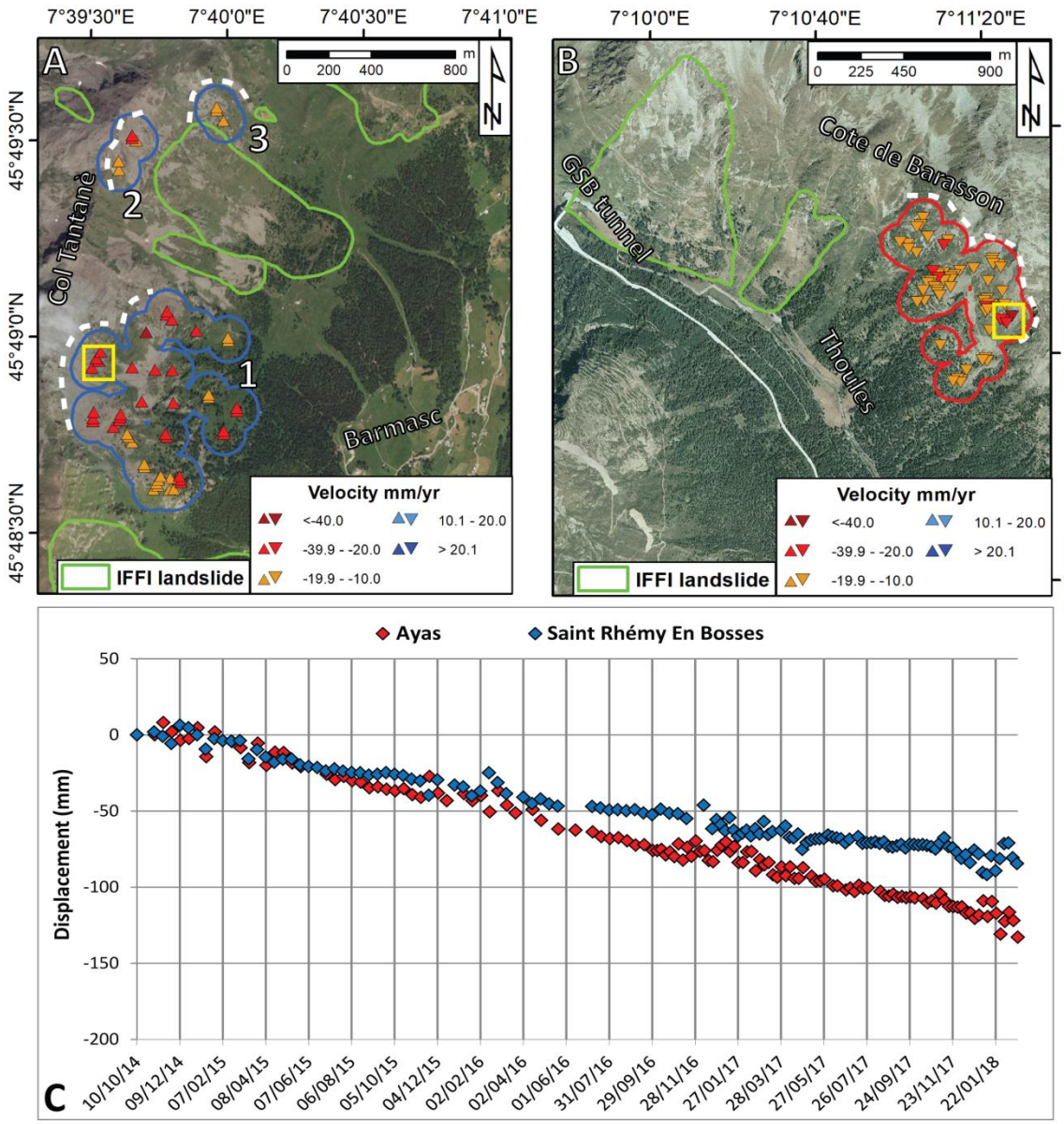

Figure 33 - Moving areas falling outside the contours of already mapped landslides. The Sentinel-1-derived PS points are represented as triangles with downward orientation if the orbit is descending, upward if it is ascending. Red and blue contours represent moving areas in descending and ascending orbits, respectively. The white dashed lines represent possible landslide crowns traced on the basis of terrain morphology and PS data. Two examples from the Ayas (A) and Saint Rhémy En Bosses (B) municipalities are reported. C) average time series of deformation for the sectors indicated by yellow rectangles.

7 Discussion

The main goal of the thesis was to propose a "hot-spot" InSAR analysis at regional scale of two Italian Regions with strong geomorphological differences, in order to highlight the main active moving areas over the Regions. Starting from deformations maps, which contain thousands of measurements points, an easy-to-use semi-automatic method was performed.

A large number of geo-hazards affects Tuscany Region, in fact 117.000 landslides are catalogued in the IFFI inventory and 1094 km² of subsidence areas are mapped. Therefore, it is important creating a priority list of the main active phenomena on the territory, in order to help the local administrator to correctly allocate funds and plan proper remedial actions. Therefore, the "hot-spot" analysis has been performed to highlight relevant ground deformations such as landslides, subsidence and uplift, starting from large MTInSAR dataset updated annually three times. With this approach, it was possible summarising hundreds of thousands of points in single clusters, grouped into a geo-database containing interferometric parameters, geographical and geomorphological information, a brief evaluation of the possible triggering cause and information about the temporal evolution of moving areas.
In this case, it wasn't carry out a simple clusters analysis of a single deformation map, but rather a comparison among three several periods: i) the first one from October 2014 to April 2017, ii) the second one from October 2014 to October 2017, iii) the third one from October 2014 to April 2018. In this way, it was possible to study the spatial and temporal evolution of the deformation clusters, every six months starting from the first period, and determining which of these was more significant. In fact, although the clusters are extracted from deformation maps elaborated over a long period, sometimes they may represent unrepresentative episodic phenomena (14% of the total). In addition, the TGPA have been defined, as the overlapping between clusters detected in different analysis periods and acquisition geometries. These areas give an idea about the persistence of the motions, highlighting the most enduring and representative areas affected by geohazards. The analysis of the three periods point out a decreasing trend of PS/DS density and as a consequence a decrease of the spatial distribution of the clusters and LOS velocity values. On one side, this is probably due to the increasing of radar images used during the processing phase, along the three analysis periods, which improve the accuracy of the output data. On the other side, the absence of intense rainfall periods during the monitored period caused a long-term reduction of landslides motion, causing some of the cluster of the first period to fall outside the fixed moving threshold.
The cluster database, obtained every six months, can be a reliable tool for updating the geo-hazard inventories. In fact, it was possible to re-evaluate the state of activity of known landslides within the IFFI database. The result does not highlight new areas affected by subsidence, but in the future this methodology may ensure the mapping of new phenomena. Detecting new areas affected by subsidence, potentially connected with excessive exploitation of the groundwater, can play a role key for the water source managing.

A second "hot-spot" analysis was carried out for the Valle d'Aosta Region in order to retrieve areas characterized by high deformation rates and to interpret the results obtained by a geomorphological/geological point of view. Despite the mountain environment and its characteristics that could have strongly limited the interferometric analysis, a total of 277 moving areas have been derived. The final output of this activity is a "radar interpreted" database of deformation clusters that includes various geographical, geomorphological and geological information useful for contextualizing satellite data into the natural environment. This database is delivered to regional authorities in charge of hydrogeological risk management (geological service of the Valle d'Aosta Region) and to the Regional Civil Protection. These

entities actively collaborated to design the database, proving a continuous exchange of information between academia and risk management actors.

The products generated in this way are currently implemented in the landslide risk management chain of the Valle d'Aosta Region, focusing on landslide state of activity definition and landslide mapping. The aim is not to update or define the activity of every landslide with PS inside but to detect only those ones with the highest deformation rates at the moment of the analysis and that could have the highest probability of future failures. Landslide mapping based on interferometric data is challenging task; in fact, due to the intrinsic limitations of the technique (presence of vegetation, topographic effects, etc…) it is difficult to obtain a complete interferometric data coverage of a landslide. Thus, landslide contours must be defined with the support of other remotely sensed data, such as multitemporali optical images, in situ measurements and field surveys. As shown by Figure 33, the deformation clusters can be used as a proxy for delimiting the spatial distribution of active motions, but they cannot be used to define a precise landslide contour without the help of other external data. Consequently, the procedure is intended as a tool for a rapid definition of slope movements at regional scale, creating a priority list for future ground surveys and further detailed scale analyses.
As mentioned before, the Alpine regions are challenging environments for interferometric applications. It is necessary to know a priori the spatial distribution of possible "no data" areas, using approaches based on the integration between morphology, land cover and satellite acquisition geometry, as the CRI here used. The results obtained are a clear reflection of the morphological limitations forced by valley orientation in the Valle d'Aosta territory. The first case presented of Bosmatto (Figure 32A) is an example of this. This landslide is in fact well detectable only in descending orbit, where 90% of the real displacement vector can be measured. This percentage drastically falls below 20% in ascending orbit. On the other hand, the Allesaz landslide (Figure 32B) is one example of slope motion that could be detected more or less in the same way in both orbits. It was estimated that this type of overlapping realizes only in 20% of the mapped moving areas. Considering topographic and land cover limitations, it is important to rank the cluster of deformations giving them a quality score (Barra et al., 2017). In this case we used a "radar visibility index" that can be based on two quantities, one related to the time series (coherence), one connected to the terrain (C index). The first index takes into account the level of noise of the time series, especially at high altitudes where the snow cover is persistent for several months (Cignetti et al., 2016). The second index is introduced in order to evaluate the effect of slope orientation on the interferometric measurements.

The regional scale processing approach could have some limitation at detailed scale, especially if the point density is low (for different reasons). That is why for the computational power it is unsustainable extracting hundreds of millions points and at the same time it is unmanageable for the end-users work with very big shape-files as outputs. Therefore, it is worth to apply a proper extraction grid with a well-balanced coherence threshold during the processing steps. So, in this thesis we analysed the case of the salt dissolution mine in Saline di Volterra, where it was expected to find very high deformation rates as testified by the presence of numerous sinkholes. Although the impact of ground deformation is, for now, not directly interfering with any human activity, the quantification of the deformation triggered by this mining activity is certainly of interest for the local entities and land planners, considering that only part of the mining concessions is currently exploited. Therefore, a target oriented processing approach was designed, in order to spot the fastest motions over the area, squeezing as much as possible the information contained in the Sentinel-1 images, within the technical and intrinsic limitations of the technique. This assumes that sinkholes are likely connected to very high subsidence rates (e.g. Raucoles et al., 2003), well recognizable from other slow-moving phenomena that characterize the area. It is important to maximize the spatial sampling of

measurement points and to reduce the temporal baseline of interferograms in order to decrease the aliasing error. The result is a deformation map involving low-coherence radar target where the fast moving areas are well-detected (see Figure 6) or detected as much as technically possible (see Figure 27). The trade off is a higher standard deviation of the velocity estimation and the presence of measurement points with uncorrelated signal. It is worth noting that such local-scale approach is clearly not suitable for small scale mapping activities, where the high point density would negatively impact on the definition of the moving areas, creating too many false positives. The processing approach allowed deriving a high density of measurement points covering the mining concessions around Saline di Volterra. The analysis of the deformation map revealed the presence of several subsidence bowls which are in some cases correspondent to areas where sinkholes have been already formed in the recent past. Figure *34* shows the measurement points with the fastest movements spotted within the mining area and all of the points extracted with the regional processing approach. As we can see, the density improvement compared to the Tuscany Region wide areas results are significant. In this case, 393 points were extracted in the main deformation areas, against a total of 33 points with the regional processing approach.

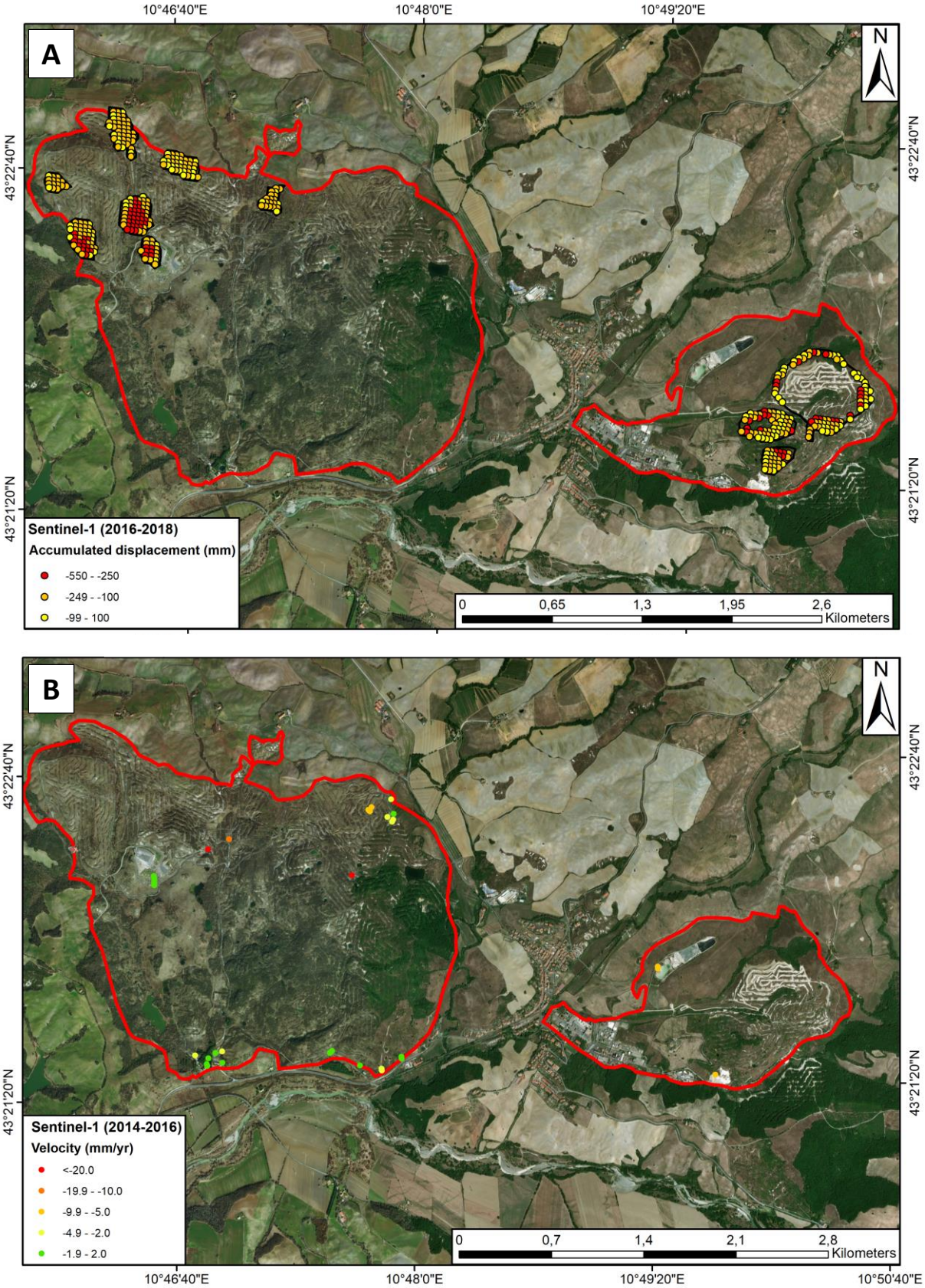

Figure 34 – (A) shows the fastest measurement points extracted over the mining areas. (B) shows all of the measurement point extracted with the regional processing approach.

Conclusion

In this PhD Thesis, the potentialities and drawbacks of the interferometric technique have been presented and then exploited to define three different procedures, applied in different environment and at different scales, for the use of multi-band PSI products. This thesis work represents the main outcome of a three years-long activity at the Department of Earth Sciences of the University of Florence, Centre technologic de telecomunicacions de Catalunya research center and TRE-Altamira (Barcelona). The main goal is to test and evaluate the potential and applicability of space-borne SAR data, processed by means of different PSI approaches, as operational tools for the characterization of geohazards in different geological and geomorphological environments.

The main goal of the thesis hinges on illustrating different methodologies that could be merged in one single workflow to detect active moving areas, characterize them in detail and cross-correlate the satellite data with ancillary information, implementing the obtained products and results in the Civil Protection chain and geohazard risk management. The proposed case studies were intended as examples, although referred to different environments and geohazards, for the working approaches to be used from regional to detailed scale.

For the Tuscany Region, located in central Italy and characterized by an extremely variegated landscape with different geohazards, ranging from landslides to subsidence, we exploited Sentinel-1 images for active moving areas detection at regional scale. A hotspot-like methodology is proposed, exploiting the temporal repetitiveness of Sentinel-1 data analysed by means of the SqueeSAR algorithm to create deformation maps in three different periods with a 6 months update. Thanks to a filtering approach based on a velocity threshold, it was possible extract a total of 652 deformation clusters, divided in three different periods, to study their spatial and temporal evolution. The final output is a flexible geo-database that contains interferometric parameters, geographical, geomorphological and geological information, a brief evaluation of the possible triggering cause and information about the temporal evolution of the moving areas. Considering the 6-days repeatability of the Sentinel-1 constellation, this clustering methodology turns out to be reliable, fast and readily reproducible. This work represents the first cluster database in Tuscany region, focused on landslide and subsidence phenomena, required by regional Civil Protection for risk management. In fact, thanks to this first update at regional scale it is possible create a priority list, with the most important deformation areas, reducing economic and personnel costs and correctly plan countermeasures at municipal scale.

Saline di Volterra is a local scale application of multi-temporal satellite interferometry targeting a solution mining area in southern Tuscany. The surroundings of Saline di Volterra host several brine wells that pump water into a salt level at a depth ranging between 60 and 400 m below surface. The mining activity has a relevant environmental impact in terms of depletion of the water resources and in terms of ground motion, creating several sinkholes which were mapped through multi-temporal analysis of orthophotos. The deformation map, obtained through the analysis of Sentinel-1 images, revealed the presence of several subsidence bowls, sometimes corresponding to sinkholes formed in the recent past. The subsidence bowls have a common deformation pattern, with LOS velocities increasing forward the center of the bowl. The temporal evolution of the measurement points can vary a lot on case-basis. Finally, a correlation between LOS velocities and age of formation of sinkholes have been found. Although with some uncertainties, the processing approach presented in this work was able to detect fast deformation rates that are usually

puzzling to solve in mining areas. This detailed scale and target-oriented approach demonstrated its capability to provide useful information in terms of density of measurement points and quality of the time series. A future evolution of this work could be further analyses that involve the decrease of the temporal frequency of data processing and its application in other mining contexts, going forward to the creation of a monitoring system based on satellite interferometric data.

Valle d'Aosta Region (Northwestern Italy) is an alpine region characterized by a wide spectrum of mass wasting phenomena. Our approach, based on simple GIS tools and indexes, allowed detecting 277 moving areas above the selected velocity threshold. Overall, landslides (complex, rotational, DSGSD), rock glacier evolution and detrital-related deformation are responsible for the detected motions. This work presents an example of a clustering analysis applied to a large stack of Sentinel-1 satellite interferometric products that has been derived using the SqueeSAR algorithm. This type of approach allows reducing the time needed for a complete analysis of an interferometric dataset. In mountainous areas, where the field data collection is sometimes limited or impossible, the presented approach is intended to create priority areas to be focused for further investigations. In this way it is possible to increase, with reduced economic and personnel costs, the "landslide knowledge" of all the actors involved within the landslide risk management chain at regional scale. Well knowing the limitations of the interferometric technique, especially in mountain regions, it is reasonable to rely on clustering approaches in order to derive multi-temporal synoptic views of ground motions over wide areas.

References

A. H. (2008). The classification, recording, databasing and use of information about building damage caused by subsidence and landslides. *Quarterly Journal of Engineering Geology* and *Hydrogeology*, 41(3), 409-424.

Abdikan, S., Sanli, F. B., Ustuner, M., & Calò, F. (2016). Land cover mapping using Sentinel-1 SAR data. *The International Archives of Photogrammetry, Remote Sensing and Spatial Information Sciences*, *41*, 757.

Achim, A., Tsakalides, P., & Bezerianos, A. (2003). SAR image denoising via Bayesian wavelet shrinkage based on heavy-tailed modeling. *IEEE Transactions on Geoscience and Remote Sensing*, 41(8), 1773-1784.

Adam, N., Gonzalez, F. R., Parizzi, A., & Liebhart, W. (2011). Wide area persistent scatterer interferometry. In Geoscience and Remote Sensing Symposium (IGARSS), 2011. *IEEE International*, 1481-1484. *IEEE*.

Aguzzi, M., Amorosi, A., Colalongo, M.L., Ricci Lucchi, M., Rossi, V., Sarti, G., & Vaiani, S.C. (2007). Late Quaternary climatic evolution of the Arno coastal plain (Western Tuscany, Italy) from subsurface data. *Sedimentary Geology,* 202, 211-229.

Amorosi, A., Rossi, V., Sarti, G., & Mattei, R. (2013) Coalescent valley fills from the late Quaternary record of Tuscany (Italy). *Quaternary International*, 288, 129-138.

Amorosi, A., Sarti, G., Rossi, V., & Fontana, V. (2008) Anatomy and sequence stratigraphy of the late Quaternary Arno valley fill (Tuscany, Italy). *Advanced Applied Sequence Stratigraphi*, 1, 55-66.

Ancochea, E., Hernán, F., Huertas, M.J., Brändle, J.L., & Herrera, R. (2006.) A new chronostratigraphical and evolutionary model for La Gomera: implications for the overall evolution of the Canarian Archipelago. *Journal of Volcanology and Geothermal Research*, 157(4), 271-293.

Ancochea, E., Huertas, M.J., Cantagrel, J.M., Coello, J., Fúster, J.M., Arnaud, N., & Ibarrola, E. (1999). Evolution of the Cañadas edifice and its implications for the origin of the Cañadas Caldera (Tenerife, Canary Islands). *Journal of Volcanology and Geothermal Research*, 88(3), 177-199.

ARPAT (2006). Quadro conoscitivo ambientale degli insediamenti Solvay nelle province di Pisa e Livorno (2000-2005). Technical report.

Aschbacher, J., & Milagro-Pérez, M. P. (2012). The European Earth monitoring (GMES) programme: Status and perspectives. *Remote Sensing of Environment*, *120*, 3-8.

Aslan, G., Foumelis, M., Raucoules, D., De Michele, M., Bernardie, S., & Cakir, Z. (2020). Landslide mapping and monitoring using persistent scatterer interferometry (PSI) technique in the French Alps. *Remote Sensing*, *12*(8), 1305.

Atzori, S., Hunstad, I., Chini, M., Salvi, S., Tolomei, C., Bignami, C., Stramondo S., Trasatti E., Antonioli A., & Boschi, E. (2009). Finite fault inversion of DInSAR coseismic displacement of the 2009 L'Aquila earthquake (central Italy). *Geophysical Research Letters*, 36(15).

Auer, S., Gernhardt, S., & Bamler, R. (2011). Ghost persistent scatterers related to multiple signal reflections. *IEEE Geoscience and Remote Sensing Letters*, 8(5), 919-923.

Avallone, A., Zollo, A., Briole, P., Delacourt, C., & Beauducel, F. (1999). Subsidence of Campi Flegrei (Italy) detected by SAR interferometry. *Geophysical Research Letters*, 26(15), 2303-2306.

Baer, G., Magen, Y., Nof, R. N., Raz, E., Lyakhovsky, V., & Shalev, E. (2018). InSAR measurements and viscoelastic modeling of sinkhole precursory subsidence: Implications for sinkhole formation, early warning, and sediment properties. *Journal of Geophysical Research: Earth Surface*, 123(4), 678-693.

Bally, P. (2012). Scientific and technical memorandum of the international forum on satellite EO and geohazards, 21–23 May 2012. Santorini, Greece. 10, 5270.

Balteanu, D., Enciu, P., & Deak, G. (2006). A large scale collapse in the Ocnele Mari salt mine field, Getic Subcarpathians, Romania. *Studia Geomorfologica Carpatho–Balcanica*, XL, 119-126.

Bamler, R., & Hartl, P. (1998). Synthetic aperture radar interferometry. *Inverse problems*, 14(4), R1.

Barra, A., Monserrat, O., Mazzanti, P., Esposito, C., Crosetto, M., & Scarascia Mugnozza, G. (2016). First insights on the potential of Sentinel-1 for landslides detection. *Geomatics, Natural Hazards and Risk*, *7*(6), 1874-1883.

Barra, A., Solari, L., Béjar-Pizarro, M., Monserrat, O., Bianchini, S., Herrera, G., Crosetto, M., Sarro, R., Gonzales-Alonso, E., Mateos, R.M., Ligüerzana, S., Lopez, C., & Moretti, S. (2017). A Methodology to Detect and Update Active Deformation Areas Based on Sentinel-1 SAR Images. *Remote Sensing*, *9*(10), 1002.

Barsch, D. (1996). Rockglaciers: Indicators for the Present and Former Geoecology in High Mountain Environments. In *Springer Series in Physical Environment*; Springer Verlag, Berlin, Germany, Volume 16, pp. 331; 978-3-642-80093-1.

Batini, F., Brogi, A., Lazzarotto, A., Liotta, D., & Pandeli, E. (2003). Geological features of Larderello-Travale and Mt. Amiata geothermal areas (southern Tuscany, Italy). *Episodes*, *26*(3), 239-244.

Béjar-Pizarro, M., Notti, D., Mateos, R.M., Ezquerro, P., Centolanza, G., Herrera, G., *et al*. (2017). Mapping Vulnerable Urban Areas Affected by Slow-Moving Landslides Using Sentinel-1 InSAR Data. *Remote Sensing*, 9(9), 876.

Belcher, D. P., & Baker, C. J. (1996). High resolution processing of hybrid strip-map/spotlight mode SAR. *IEEE Proceedings-Radar, Sonar and Navigation*, 143(6), 366-374.

Bell, F.G., Stacey, T.R., & Genske, D.D. (2000). Mining subsidence and its effect on the environment: Some differing examples. *Environmental Geology*, 2000, 40, 135-152.

Berardino, P., Fornaro, G., Lanari, R., Sansosti, E. (2002). A new algorithm for surface deformation monitoring based on small baseline differential SAR interferograms. *IEEE Transactions on Geoscience and Remote Sensing*, 40 (11), 2375-2383.

Berti, M., Corsini, A., Franceschini, S., & Iannacone, J. P. (2013). Automated classification of Persistent Scatterers Interferometry time series. *Natural Hazards and Earth System Sciences*, 13(8), 1945-1958.

Bianchini, S., Ciampalini, A., Raspini, F., Bardi, F., Di Traglia, F., Moretti, S., & Casagli, N. (2015). Multi-temporal evaluation of landslide movements and impacts on buildings in San Fratello (Italy) by means of C-band and X-band PSI data. *Pure and Applied Geophysics*, 172(11), 3043-3065.

Bianchini, S., Cigna, F., Righini, G., Proietti, C., & Casagli, N. (2012). Landslide hotspot mapping by means of persistent scatterer interferometry. *Environmental Earth Sciences*, *67*(4), 1155-1172.

Bianchini, S., Del Soldato, M., Solari, L., Nolesini, T., Pratesi, F., & Moretti, S. (2016). Badland susceptibility assessment in Volterra municipality (Tuscany, Italy) by means of GIS and statistical analysis. *Environmental Earth Sciences*, 75(10), 1-14.

Bianchini, S., Herrera, G., Mateos, R.M., Notti, D., Garcia, I., Mora, O., Moretti, S. (2013). Landslide activity maps generation by means of persistent scatterer interferometry. *Remote Sensing*, 5(12), 6198-6222.

Bianchini, S., Raspini, F., Ciampalini, A., Lagomarsino, D., Bianchi, M., Bellotti, F., & Casagli, N. (2017). Mapping landslide phenomena in landlocked developing countries by means of satellite remote sensing data: the case of Dilijan (Armenia) area. *Geomatics, Natural Hazards and Risk*, *8*(2), 225-241.

Bianchini, S., Solari, L., & Casagli, N. (2017). A gis-based procedure for landslide intensity evaluation and specific risk analysis supported by persistent scatterers interferometry (PSI). *Remote Sensing*, 9 (11), 1093.

Bicocchi, G., D'Ambrosio, M., Rossi, G., Rosi, A., Tacconi-Stefanelli, C., Segoni, S., Nocentini, M., Vannocci, P., Tofani, V., & Catani, F. (2016). Geotechnical in situ measures to improve landslides forecasting models: A case study in Tuscany (Central Italy). In *Landslides and Engineered Slopes. Experience, Theory and Practice: Proceedings of the 12th International Symposium on Landslides* (Napoli, Italy, 12-19 June 2016) (p. 419). CRC Press.

Bistacchi, A., Dal Piaz, G., Massironi, M., Zattin, M., & Balestrieri, M. (2001). The Aosta–Ranzola extensional fault system and Oligocene–Present evolution of the Austroalpine–Penninic wedge in the northwestern Alps. *International Journal of Earth Sciences*, 90, 654-667.

Blanco, P., Mallorqui, J., Duque, S., & Navarrete, D. (2006). Advances on DInSAR with ERS and ENVISAT data using the Coherent Pixels Technique (CPT). In *Geoscience and Remote Sensing Symposium*, *2006. IGARSS 2006. IEEE International Conference on*, 1898-1901. IEEE.

Bonano, M., Manunta, M., Pepe, A., Paglia, L., & Lanari, R. (2013). From previous C-band to new X-band SAR systems: Assessment of the DInSAR mapping improvement for deformation time-series retrieval in urban areas. *Transactions on Geoscience and Remote Sensing*, 51(4), 1973-1984. IEEE.

Bonforte, A., Guglielmino, F., Coltelli, M., Ferretti, A., & Puglisi, G. (2011). Structural assessment of Mount Etna volcano from Permanent Scatterers analysis. *Geochemistry, Geophysics, Geosystems*, 12(2).

Bortolotti, V. (1992). The Tuscany–Emilian Apennine. *Regional Geological Guidebook*, 4, 329. S.G.I. BEMA Editrice.

Bovenga, F., Wasowski, J., Nitti, D. O., Nutricato, R., & Chiaradia, M. T. (2012). Using COSMO/SkyMed X-band and ENVISAT C-band SAR interferometry for landslides analysis. *Remote Sensing of Environment*, 119, 272-285.

Brogi, A. (2008). The structure of the Monte Amiata volcano-geothermal area (Northern Apennines, Italy): Neogene-Quaternary compression versus extension. *International Journal of Earth Sciences*, *97*(4), 677-703.

Buffet, A. (1998). The collapse of Compagnie des Salins SG4 and SG5 drillings. In *Proceedings of SMRI fall meeting, Rome* (pp. 79-105).

Burgalassi, D., Cheli, B.,Luzzati, T., Del Soldato, V., & Freschi, E. (2010). Analisi delle ricadute ambientali della Solvay sul territorio della Val di Cecina. In *La Solvay e in Val di Cecina: ricadute socio-economiche e ambientali di una grande industria chimica sul suo territorio*, Cheli, B., Luzzati T. (Eds.), Edizioni Plus srl, Pisa, Italy, pp. 145-217.

Butteri, M., Doveri, M., Giannecchini, R., & Gattai, P. (2010). Hydrogeologic-hydrogeochemical multidisciplinary study of the confined gravelly aquifer in the coastal Pisan Plain between the Arno River and Scolmatore Canal (Tuscany). *Memorie Descrittive Carta Geologica d'Italia*, XC, 51–66.

Calamai A., Cataldi R., Squarci P., & Taffi, L. (1970). Geology, Geophysics and Hydrogeology of the Monte Amiata Geothermal Field. *Geothermics 1(Spec)*, 1-9.

Calcaterra, D., de Riso, R., & Santo, A. (2003). Landslide hazard and risk mapping: experiences from Campania, Italy. In L. Picarelli (Eds) *Fast Slope Movements, Prediction and Prevention for Risk Mitigation*, 63-70. Patron Editore.

Calò, F., Ardizzone, F., Castaldo, R., Lollino, P., Tizzani, P., Guzzetti, F., Lanari R., Angeli M.G., Pontoni F., & Manunta, M. (2014). Enhanced landslide investigations through advanced DInSAR techniques: The Ivancich case study, Assisi, Italy. *Remote Sensing of Environment*, 142, 69-82.

Cantini, P., Testa, G., Zanchetta, G., & Cavallini, R. (2001). The Plio-Pleistocene evolution of extensional tectonics in northern Tuscany, as constrained by new gravimetric data from the Montecarlo Basin (lower Arno Valley, Italy). *Tectonophysics*, 330, 25–43.

Canuti, P., Casagli, N., Ermini, L., Fanti, R., & Farina, P. (2004). Landslide activity as a geoindicator in Italy: significance and new perspectives from remote sensing. *Environmental Geology*, *45*(7), 907-919.

Canuti, P., Casagli, N., Farina, P., Marks, F., Ferretti, A., & Menduni, G. (2005). Land subsidence in the Arno River Basin studied through SAR interferometry. In *Proceedings of the 7th International Symposium on Land Subsidence, Shanghai, China, 23–28 October 2005*, 1, 407-416.

Capecchi, F., Guazzone, G., & Pranzini, G. (1975). Il bacino lacustre di Firenze-Prato-Pistoia; geologia del sottosuolo e ricostruzione evolutiva. *Bollettino della Societa Geologica Italiana*, *94*(4), 637-660.

Carmignani, L., Decandia, F. A., Disperati, L., Fantozzi, P. L., Kligfield, R., Lazzarotto, A., Liotta, D., & Meccheri, M. (2001). Inner Northern Apennines. In *Anatomy of an Orogen: the Apennines and adjacent Mediterranean* Basins, 197-213. Springer Netherlands.

Carmignani, L., Decandia, F. A., Fantozzi, P. L., Lazzarotto, A., Liotta, D., & Meccheri, M. (1994). Tertiary extensional tectonics in Tuscany (northern Apennines, Italy). *Tectonophysics*, 238(1-4), 295-310, 313-315.

Carracedo, J.C. (1994) The Canary Island: an example of structural control on the growth of large oceanic-island volcanoes. *Journal of Volcanology and Geothermal Research*, 60(3-4), 225-241.

Carracedo, J.C., Pérez-Torrado, F.J., Ancochea, E., Meco, J., Hernán, F., Cubas, C.R., Casillas, R., Rodríguez-Badiola, E., & Ahijado, A. (2002). Cenozoic Volcanism II, The Canary Islands. In: *Gibsson W, Moreno T (Eds) The Geology of Spain*. *The Geological Society*, 439–472.

Carraro, F., & Giardino, M. (2004). Quaternary glaciations in the western Italian Alps-a review. In *Quaternary Glaciations – Extent and Chronology. Part 1. Developments in Quaternary Science*; Ehlers, J., Gibbard, P.L., Eds.; Elsevier Science, Volume 2, pp. 201-208.

Casagli, N., Cigna, F., Bianchini, S., Hölbling, D., Füreder, P., Righini, G., Del Conte, S., Freidl, B., Schneiderbauer, S., Iasio, G., Vlcko, J., Greif, H., Proske, H., Granica, K., Falco, S., Lozzi, S., Mora, O., Arnaud, A., Novali, F., & Bianchi, M. (2016). Landslide mapping and monitoring by using radar and optical remote sensing: examples from the EC-FP7 project SAFER. *Remote Sensing Applications: Society and Environment*, 4, 92-108.

Casagli, N., Frodella, W., Morelli, S., Tofani, V., Ciampalini, A., Intrieri, E., *et al*. (2017). Spaceborne, UAV and ground-based remote sensing techniques for landslide mapping, monitoring and early warning. *Geoenvironmental Disasters*, 4, 9.

Casagrande, A. (1948). Classification and identification of soils. *Transaction of the American Society of Civil Engineers*, 113, 901-930.

Castañeda, C., Gutiérrez, F., Manunta, M., & Galve, J. P. (2009). DInSAR measurements of ground deformation by sinkholes, mining subsidence, and landslides, Ebro River, Spain. *Earth Surface Processes and Landforms*, 34(11), 1562-1574.

Chang, H. C., Ge, L., & Rizos, C. (2005). DInSAR for mine subsidence monitoring using multi-source satellite SAR images. In *Geoscience and Remote Sensing Symposium, 2005. IGARSS'05. Proceedings. 2005 IEEE International*, 3, 1742-1745. IEEE.

Cheli B., Coli A., Del Soldato V., Luzzati T.(2014). “Stima delle ricadute economiche della Solvay sul territorio della Val di Cecina dal 2006 al 2012”, Discussion Papers del Dipartimento di Scienze Economiche – Università di Pisa, n. 193.

Chen, F., Lin, H., Zhang, Y., & Lu, Z. (2012). Ground subsidence geo-hazards induced by rapid urbanization: Implications from InSAR observation and geological analysis. *Natural Hazards and Earth System Sciences*, *12*(4), 935-942.

Chini, M., Atzori, S., Trasatti, E., Bignami, C., Kyriakopoulos, C., Tolomei, C., & Stramondo, S. (2010). The May 12, 2008,(Mw 7.9) Sichuan earthquake (China): multiframe ALOS-PALSAR DInSAR analysis of coseismic deformation. *IEEE Geoscience and Remote Sensing Letters*, 7(2), 266-270.

Ciampalini, A., Bardi, F., Bianchini, S., Frodella, W., Del Ventisette, C., Moretti, S., & Casagli, N. (2014). Analysis of building deformation in landslide area using multisensor PSInSAR™ technique. *International Journal of Applied Earth Observation and Geoinformation*, 33, 166-180.

Ciampalini, A., Raspini, F., Bianchini, S., Frodella, W., Bardi, F., Lagomarsino, D., *et al*. (2015). Remote sensing as tool for development of landslide databases: the case of the Messina Province (Italy) geodatabase. *Geomorphology*, 249, 103-118. https://doi.org/10.1016/j.geomorph.2015.01.029.

Ciampalini, A., Raspini, F., Lagomarsino, D., Catani, F., & Casagli, N. (2016). Landslide susceptibility map refinement using PSInSAR data. *Remote Sensing of Environment*, 184, 302-315.

Cigna, F., & Tapete, D. (2017). PROTHEGO Deliverable D.02.01: Available satellite InSAR data for the European WHL sites, Version 1.0. JPI-CH Heritage Plus PROTHEGO project, Open Report. Date 27/04/2017. pp. 45 (iii + 18 + 23). Available at: http://prothego.eu/docs/PROTHEGO_D.02.01.pdf.

Cigna, F., Bateson, L. B., Jordan, C. J., & Dashwood, C. (2014). Simulating SAR geometric distortions and predicting Persistent Scatterer densities for ERS-1/2 and ENVISAT C-band SAR and InSAR applications: Nationwide feasibility assessment to monitor the landmass of Great Britain with SAR imagery. *Remote Sensing of Environment*, 152, 441-466.

Cigna, F., Bianchini, S., & Casagli, N. (2013). How to assess landslide activity and intensity with Persistent Scatterer Interferometry (PSI): the PSI-based matrix approach. *Landslides*, *10*(3), 267-283.

Cigna, F., Del Ventisette, C., Liguori, V., & Casagli, N. (2011). Advanced radar-interpretation of InSAR time series for mapping and characterization of geological processes. *Natural Hazards and Earth System Sciences*, 11(3), 865.

Cigna, F., Tapete, D., & Casagli, N. (2012). Semi-automated extraction of Deviation Indexes (DI) from satellite Persistent Scatterers time series: tests on sedimentary volcanism and tectonically-induced motions. *Nonlinear Processes in Geophysics*, 19(6), 643-655.

Cignetti, M., Manconi, A., Manunta, M., Giordan, D., De Luca, C., Allasia, P., & Ardizzone, F. (2016). Taking advantage of the esa G-pod service to study ground deformation processes in high mountain areas: A Valle d'Aosta case study, northern Italy. *Remote Sensing*, 8(10), 852.

Colesanti, C., & Wasowski, J. (2006). Investigating landslides with space-borne Synthetic Aperture Radar (SAR) interferometry. *Engineering geology*, 88(3), 173-199.

Colombo, D., Farina, P., Moretti, S., Nico, G., & Prati, C. (2003, July). Land subsidence in the Firenze-Prato-Pistoia basin measured by means of spaceborne SAR interferometry. In *Geoscience and Remote Sensing Symposium, 2003. IGARSS'03. Proceedings. 2003 IEEE International*, 4, 2927-2929. IEEE.

Coltorti, M., Brogi, A., Fabbrini, L., Firuzabadì, D., & Pieranni, L. (2011). The sagging deep-seated gravitational movements on the eastern side of Mt. Amiata (Tuscany, Italy). *Natural hazards*, *59*(1), 191-208.

Comune di Pisa (1997). Relazione Generale e Allegati Tecnici del Piano Strutturale del Comune di Pisa. Available online: http://www.comune.pisa.it/doc/sit-pisa/nuovo_prg/relaz.html.

Corine Land Cover of Italy (2012). ISPRA, http://www.sinanet.isprambiente.it/it/ sia-ispra/download-mais/corine-land-cover (accessed on 30 July 2018).

Costantini, M. (1998). A novel phase unwrapping method based on network programming. *IEEE Transactions on Geoscience and Remote Sensing*, 36(3), 813-821.

Costantini, M., Falco, S., Malvarosa, F., Minati, F. (2008). A new method for identification and analysis of persistent scatterers in series of SAR images. In*: Proceedings of IGARSS 2008, Boston*.

Costantini, M., Falco, S., Malvarosa, F., Minati, F., Trillo, F., Vecchioli, F. (2014). Persistent scatterer pair interferometry: approach and application to COSMOSkyMed SAR data. *Journal of Selected Topics in Appied Earth Observation Remote Sensing*, 7(7).

Costantini, M., Minati, F., Ciminelli, M. G., Ferretti, A., & Costabile, S. (2015). Nationwide ground deformation monitoring by persistent scatterer interferometry. In *Geoscience and Remote Sensing Symposium (IGARSS), 2015 IEEE International*, 1472-1475. IEEE.

Crosetto, M., Biescas, E., Duro, J., Closa, J., & Arnaud, A. (2008). Generation of advanced ERS and Envisat interferometric SAR products using the stable point network technique. *Photogrammetric Engineering Remote Sensing*, 74 (4), 443-450.

Crosetto, M., Castillo, M., & Arbiol, R. (2003). Urban subsidence monitoring using radar interferometry. *Photogrammetric Engineering Remote Sensing*, 69(7), 775-783.

Crosetto, M., Crippa, B., Biescas, E. (2005b). Early detection and in-depth analysis of deformation phenomena by radar interferometry. *Engineering Geology*, 79, 81–91.

Crosetto, M., Crippa, B., Biescas, E., Monserrat, O., & Agudo, M. (2005a). State of the art of land deformation monitoring using differential SAR interferometry. In *ISPRS Hannover Workshop*, 17-20.

Crosetto, M., Gili, J. A., Monserrat, O., Cuevas-González, M., Corominas, J., & Serral, D. (2013). Interferometric SAR monitoring of the Vallcebre landslide (Spain) using corner reflectors. *Natural Hazards and Earth System Sciences*, 13(4), 923.

Crosetto, M., Monserrat, O., Cuevas, M., & Crippa, B. (2011). Spaceborne differential SAR interferometry: Data analysis tools for deformation measurement. *Remote Sensing*, 3(2), 305-318.

Crosetto, M., Monserrat, O., Cuevas-González, M., Devanthéry, N., & Crippa, B. (2016). Persistent scatterer interferometry: a review. *ISPRS Journal of Photogrammetry and Remote Sensing*, 115, 78-89.

Crosetto, M., Monserrat, O., Cuevas-González, M., Devanthéry, N., Luzi, G., & Crippa, B. (2015). Measuring thermal expansion using X-band persistent scatterer interferometry. *ISPRS Journal of Photogrammetry and Remote Sensing*, 100, 84-91.

Crosetto, M., Monserrat, O., Iglesias, R., & Crippa, B. (2010). Persistent scatterer interferometry: potential, limits and initial C- and X-band comparison. *Photogrammetric Engineering & Remote Sensing*, 76(9), 1061-1069.

Crosta, G.B., Frattini, P., & Agliardi, F. (2013). Deep seated gravitational slope deformations in the European Alps. *Tectonophysics*, 605, 13-33.

Cruden, D. M., & Varnes, D. J. (1996). Landslides investigation and mitigation, transportation research board. *Landslide types and process, National Research Council, National Academy Press, Special Report*, *247*, 36-75.

Cumming I.G., Wong F.H. (2005) Digital processing of synthetic aperture radar data: Algorithms and implementation. Artech House.

Dai, K., Li, Z., Tomás, R., Liu, G., Yu, B., Wang, X., Cheng, H., Chen, J., & Stockamp, J. (2016). Monitoring activity at the Daguangbao mega-landslide (China) using Sentinel-1 TOPS time series interferometry. *Remote Sensing of Environment*, *186*, 501-513.

Dal Piaz, G.V., Bistacchi, A., & Massironi, M. (2003). Geological outline of the Alps. *Episodes*, 26, 175-180.

Davalillo, J. C., & Zucca, F. (2014). A methodology for improving landslide PSI data analysis. *International Journal of Remote Sensing*, 35(6), 2186-2214.

De Zan, F., & Guarnieri, A.M. (2006). TOPSAR: Terrain observation by progressive scans. IEEE *Transactions on Geoscience and Remote Sensing*, 44, 2352-2360.

Del Soldato, M., Bianchini, S., Calcaterra, D., De Vita, P., Martire, D. D., Tomás, R., & Casagli, N. (2017). A new approach for landslide-induced damage assessment. *Geomatics, Natural Hazards and Risk*, *8*(2), 1524-1537.

Del Soldato, M., Farolfi, G., Rosi, A., Raspini, F., & Casagli, N. (2018a). Subsidence Evolution of the Firenze–Prato–Pistoia Plain (Central Italy) Combining PSI and GNSS Data. *Remote Sensing*, *10*(7), 1146.

Del Soldato, M., Riquelme, A., Bianchini, S., Tomàs, R., Di Martire, D., De Vita, P., Moretti, S., & Calcaterra, D. (2018b). Multisource data integration to investigate one century of evolution for the Agnone landslide (Molise, southern Italy). *Landslides*, *15*(11), 2113-2128.

Del Ventisette, C., Solari L., Raspini, F., Ciampalini, A., Di Traglia, F., Moscatelli, M., Pagliaroli, A., & Moretti, S. (2015). Use of PSInSAR data to map highly compressible soil layers. *Geologica Acta: an International Earth Science Journal*, 13(4).

Devanthéry, N., Crosetto, M., Monserrat, O., Cuevas-González, M., & Crippa, B. (2014). An approach to persistent scatterer interferometry. *Remote Sensing*, 6(7), 6662-6679.

Di Martire, D., Iglesias, R., Monells, D., Centolanza, G., Sica, S., Ramondini, M., Pagano L., Mallorqui J.J., & Calcaterra, D. (2014). Comparison between differential SAR interferometry and ground measurements data in the displacement monitoring of the earth-dam of Conza della Campania (Italy). *Remote Sensing of Environment*, 148, 58-69.

Di Martire, D., Paci, M., Confuorto, P., Costabile, S., Guastaferro, F., Verta, A., & Calcaterra, D. (2017). A nation-wide system for landslide mapping and risk management in Italy: The second Not-ordinary Plan of Environmental Remote Sensing. *International Journal of Applied Earth Observation and Geoinformation*, 63, 143-157.

Di Paola, G., Alberico, I., Aucelli, P. P. C., Matano, F., Rizzo, A., & Vilardo, G. (2016) Coastal subsidence detected by SAR interferometry and its effects coupled with future sea level rise: the case of the Sele plain (southern Italy). *Journal of Flood Risk Management*.

Dini, I., Rosi, A., & Rossi, A. (1990). Monitoring ground elevation changes in the Larderello geothermal region, Tuscan, Italy. *International Symposium on Geothermal Energy*, 1109-1114.

Dong, J., Zhang, L., Li, M., Yu, Y., Liao, M., Gong, J., & Luo, H. (2018). Measuring precursory movements of the recent Xinmo landslide in Mao County, China with Sentinel-1 and ALOS-2 PALSAR-2 datasets. *Landslides*, 15, 135-144.

Donnellan, A., Rundle, J., Ries, J., Fox, G., Pierce, M., Parker, J., Crippen, R., DeJong, E., Chao, B., Kuang, W., McLeod, D., Matu'ura, M., & Bloxham, J. (2004). Illuminating Earth's interior through advanced computing. *Computing in Science & Engineering*, 6(1), 36-44.

Du, Z., Ge, L., Ng, A. H. M., & Li, X. (2018). Investigation on mining subsidence over Appin–West Cliff Colliery using time-series SAR interferometry. *International Journal of Remote Sensing*, 39(5), 1528-1547.

Duro, J., Inglada, J., Closa, J., Adam, N., & Arnaud, A. (2003). High resolution differential interferometry using time series of ERS and ENVISAT SAR data. FRINGE Workshop 2003, 1-5.

Falorni, G., Morgan, J., & Eneva, M. (2011). Advanced InSAR techniques for geothermal exploration and production. *Geothermal Resources Council Transactions*, 35, 1661-1666.

Fan, J., Zhao, H., Tu, P., Wang, Y., Guo, X., Ge, D., & Liu, G. (2010). CRInSAR for landslide deformation monitoring: A case in threegorge area. In *Geoscience and Remote Sensing Symposium (IGARSS), IEEE International*, 3956-3959. IEEE.

Farina, P., Casagli, N., & Ferretti, A. (2007). Radar-interpretation of InSAR measurements for landslide investigations in civil protection practices. In *First North American Landslide Conference* (pp. 272-283).

Farina, P., Casagli, N., & Ferretti, A. (2007). Radar-interpretation of InSAR measurements for landslide investigations in civil protection practices. Proceedings of the First North American Landslide Conference, Vail, Colorado, 3-8 June 2007; Shaefer, V.R., Schuster, R.L., Turner A.K., Eds.; Association of Engineering Geologists; pp. 272-283.

Farina, P., Colombo, D., Fumagalli, A., Marks, F., & Moretti, S. (2006). Permanent Scatterers for landslide investigations: outcomes from the ESA-SLAM project. *Engineering Geology*, 88(3), 200-217.

Fell R., Corominas J., Bonnard C., Cascini L., Leroi E., Savage W.Z. (2008). Guidelines for landslide susceptibility, hazard and risk-zoning for land use planning. *Engineering Geology*, 102(3-4), 85-98.

Ferretti, A. (2014). Satellite InSAR data: reservoir monitoring from space. EAGE Publications.

Ferretti, A., Colombo, D., Fumagalli, A., Novali, F., & Rucci, A. (2015). InSAR data for monitoring land subsidence: time to think big. *Proceedings of the International Association of Hydrological Sciences*, 372, 331.

Ferretti, A., Fumagalli, A., Novali, F., Prati, C., Rocca, F., & Rucci, A. (2011). A new algorithm for processing interferometric data-stacks: SqueeSAR. *IEEE Transactions on Geoscience and Remote Sensing*, *49*(9), 3460-3470.

Ferretti, A., Novali, F., Bürgmann, R., Hilley, G., & Prati, C. (2004). InSAR permanent scatterer analysis reveals ups and downs in San Francisco Bay area. Eos, *Transactions American Geophysical Union*, 85(34), 317-324.

Ferretti, A., Prati, C., & Rocca, F. (2000). Nonlinear subsidence rate estimation using permanent scatterers in differential SAR interferometry. *IEEE Transactions on Geoscience and Remote Sensing*, 38(5), 2202-2212.

Ferretti, A., Prati, C., & Rocca, F. (2001). Permanent scatterers in SAR interferometry. *IEEE Transactions on geoscience and remote sensing*, *39*(1), 8-20.

Ferretti, A., Prati, C., Rocca, F., & Wasowski, J. (2006). Satellite interferometry for monitoring ground deformations in the urban environment. In *Proceedings 10th IAEG Congress*, 100-110.

Ferretti, A., Prati, C., Rocca, F., Casagli, N., Farina, P., & Young, B. (2005). Permanent Scatterers technology: a powerful state of the art tool for historic and future monitoring of landslides and other terrain instability phenomena. In *Proc. of 2005 International Conference on Landslide Risk Management. AA Balkema, Vancouver, Canada*.

Ferretti, A., Savio, G., Barzaghi, R., Borghi, A., Musazzi, S., Novali, F., Prati, A., & Rocca, F. (2007). Submillimeter accuracy of InSAR time series: Experimental validation. *IEEE Transactions on Geoscience and Remote Sensing*, 45(5), 1142-1153.

Fiaschi, S., Mantovani, M., Frigerio, S., Pasuto, A., & Floris, M. (2017). Testing the potential of Sentinel-1A TOPS interferometry for the detection and monitoring of landslides at local scale (Veneto Region, Italy). *Environmental Earth Sciences*, 76, 492.

Fratini, F., & Rescic, S. (2014). The stone materials of the historical architecture of Tuscany, Italy. *Geological Society*, London, Special Publications, 391(1), 71-92.

Frattini, P., Crosta, G.B., & Allievi, J. (2013). Damage to buildings in large slope rock instabilities monitored with the PSInSAR™ technique. *Remote Sensing*, 5, 4753-4773,

Frey, M., Desmons, J., & Neubauer, F. (1999). The new metamorphic map of the Alps. Schweiz. Mineral. Petrogr. Mitt., 79, 1-230.

Frodella, W., Ciampalini, A., Gigli, G., Lombardi, L., Raspini, F., Nocentini, M., Scardigli, C., & Casagli, N. (2016). Synergic use of satellite and ground based remote sensing methods for monitoring the San Leo rock cliff (Northern Italy). *Geomorphology*, 264, 80-94.

Funk, C., Verdin, A., Michaelsen, J., Peterson, P., Pedreros, D., & Husak, G. (2015). A global satellite assisted precipitation climatology. *Earth System Science Data Discussions*, 8(1).

Fuster, J.M., Araña, V., Brandle, J.L., Navarro, M., Alonso, U., & Aparicio, A. (1968). Geología y volcanología de las islas Canarias: Tenerife. Instituto Lucas Mallada, CSIC, Madrid.

Gabriel, A.K., Goldstein, R.M., Zebker, H.A. (1989). Mapping small elevation changes over large areas: differential radar interferometry. *Journal of Geophysical Research*, 94 (B7), pp. 9183-9191.

Gagnon, L., & Jouan, A. (1997). Speckle filtering of SAR images-A comparative study between complex-wavelet-based and standard filters. *In proceedings SPIE, 3169, 80-91*.

Galloway, D. L., & Burbey, T. J. (2011). Regional land subsidence accompanying groundwater extraction. *Hydrogeology Journal*, *19*(8), 1459-1486.

Galloway, D. L., Jones, D. R., & Ingebritsen, S. E. (1999). *Land subsidence in the United States* (Vol. 1182), US Geological Survey.

Galve, J.P., Castañeda, C., & Gutiérrez, F. (2015). Railway deformation detected by DInSAR over active sinkholes in the Ebro Valley evaporite karst, Spain. *Natural Hazards Earth System Sciences*, 15, 2439-2448.

Garlicki, A. (1993). Solution mining of Miocene salts in Poland and its environmental impact. Seventh Symposium on Salt, Vol 1, pp 419-424, Elsevier Science Publishers B. V., Amsterdam.

Gee, D., Sowter, A., Grebby, S., de Lange, G., Athab, A., & Marsh, S. (2019). National geohazards mapping in Europe: Interferometric analysis of the Netherlands. *Engineering Geology*, 256, 1-22.

Ghiglia, D. C., & Pritt, M. D. (1998). Two-dimensional phase unwrapping: theory, algorithms, and software. *Analytical Science*, 4.

Gianelli, G., Puxeddu, M., Batini, F., Bertini, G., Dini, I., Pandeli, E., & Nicolich, R. (1988). Geological model of a young volcano-plutonic system: the geothermal region of Monte Amiata (Tuscany, Italy). *Geothermics*, *17*(5-6), 719-734.

Giardino, M., & Ratto, S. (2007). Analisi del dissesto da frana in Valle d'Aosta. In *Rapporto sulle frane in Italia*; Trigila, A., Ed.; APAT Rapporti, Rome, Italy; pp. 121-150.

Gillespie, T. W., Chu, J., Frankenberg, E., & Thomas, D. (2007). Assessment and prediction of natural hazards from satellite imagery. *Progress in Physical Geography*, 31(5), 459-470.

Gisotti, G. (1991, May). A Case of Induced Subsidence for Extraction of Salt by Hydrosolution. In *4 th International Symposium on Land Subsidence.*

Glade, T., Anderson, M., & Crozier, M. (2005). *Landslide Hazard and Risk*. John Wiley & Sons Publisher Ltd, Chichester.

Goel, K., & Adam, N. (2014). A distributed scatterer interferometry approach for precision monitoring of known surface deformation phenomena. *IEEE Transactions on Geoscience and Remote Sensing*, 52(9), 5454-5468.

Goldstein, R. M., & Werner, C. L. (1998). Radar interferogram filtering for geophysical applications. *Geophysical research letters*, 25(21), 4035-4038.

Gomba, G., Parizzi, A., De Zan, F., Eineder, M., & Bamler, R. (2015). Toward operational compensation of ionospheric effects in SAR interferograms: The split-spectrum method. *IEEE Transactions on Geoscience and Remote Sensing*, 54(3), 1446-1461

Greif, V., & Vlcko, J. (2012). Monitoring of post-failure landslide deformation by the PS-InSAR technique at Lubietova in Central Slovakia. *Environmental Earth Sciences*, 66(6), 1585-1595.

Guarascio, M. (1987). Microseismic Monitoring of Solution Mining Cavities. APCOM 87: Mining, 1, 49.

Guillou, H., Perez-Torrado, F.J., Hansen, A., Carracedo, J.C., & Gimeno, D. (2004). The Plio- Quaternary volcanic evolution of Gran Canaria based on new K–Ar ages and magneto stratigraphy. *Journal of Volcanology Geothermal Research*, 135,221-246.

Haeberli, W., Schaub, Y., & Huggel, C. (2017). Increasing risks related to landslides from degrading permafrost into new lakes in de-glaciating mountain ranges. *Geomorphology*, 293, 405-417.

Hanssen, R. F. (2001). Radar interferometry: data interpretation and error analysis, (Vol. 2). Springer Science & Business Media.

Hernandez, B., Cocco, M., Cotton, F., Stramondo, S., Scotti, O., Courboulex, F., & Campillo, M. (2004). Rupture history of the 1997 Umbria-Marche (Central Italy) main shocks from the inversion of GPS, DInSAR and near field strong motion data. Annals of Geophysics.

Herrera, G., Fernández, M. Á., Tomás, R., González-Nicieza, C., López-Sánchez, J. M., & Vigil, A. Á. (2012). Forensic analysis of buildings affected by mining subsidence based on Differential Interferometry (Part III). *Engineering Failure Analysis*, *24*, 67-76.

Herrera, G., Gutiérrez, F., García-Davalillo, J. C., Guerrero, J., Notti, D., Galve, J. P., Fernández-Merodo J.A., & Cooksley, G. (2013). Multi-sensor advanced DInSAR monitoring of very slow landslides: The Tena Valley case study (Central Spanish Pyrenees). *Remote Sensing of Environment*, 128, 31-43.

Herrera, G., Mateos, R. M., García-Davalillo, J. C., Grandjean, G., Poyiadji, E., Maftei, R., Filipciuc, T.C., Auflic, M. J., Jez, J., Podolszki, L., & Trigila, A. (2018). Landslide databases in the geological surveys of Europe. *Landslides*, *15*(2), 359-379.

Herrera, G., Notti, D., García-Davalillo, J. C., Mora, O., Cooksley, G., Sánchez, M., Arnaud, A., & Crosetto, M. (2011). Analysis with C-and X-band satellite SAR data of the Portalet landslide area. *Landslides*, 8(2), 195-206.

Herrera, G., Tomás, R., López-Sánchez, J. M., Delgado, J., Mallorqui, J. J., Duque, S., & Mulas, J. (2007). Advanced DInSAR analysis on mining areas: La Union case study (Murcia, SE Spain). *Engineering Geology*, 90(3), 148-159.

Hetland, E.A., Musé, P., Simons, M., Lin, Y.N., Agram, P.S., & DiCaprio, C.J. (2012). Multiscale InSAR time series (MInTS) analysis of surface deformation. *Journal of Geophysical Research Solid Earth*, 117 (B2).

Hilley G.E., Bürgmann R., Ferretti A., Novali F., & Rocca F. (2004) Dynamics of Slow-Moving Landslides from Permanent Scatterer. *Analysis. Science*, 304, 1952-1955.

Hölbling, D., Füreder, P., Antolini, F., Cigna, F., Casagli, N., & Lang, S. (2012). A semi-automated object-based approach for landslide detection validated by persistent scatterer interferometry measures and landslide inventories*. Remote Sensing*, 4(5), 1310-1336.

Holik, J.S, Rabinowitz, P.D., & Austin, J.A. (1991). Effects of Canary hotspot volcanism on structure of oceanic-crust off Morocco. *Journal of Geophysical Research Solid Earth and Planets*, 96, 12039-12067.

Holzner, J., & Bamler R. (2002) Burst-mode and ScanSAR interferometry. *IEEE Transaction on Geoscience and Remote Sensing*, 40(9), 1917-1934.

Hong, Y., Adler, R., & Huffman, G. (2007). Use of satellite remote sensing data in the mapping of global landslide susceptibility. *Natural Hazards*, *43*(2), 245-256.

Hooper, A. (2006) Persistent scatterer radar interferometry for crustal deformation studies and modeling of volcanic deformation. Ph.D. Thesis, Stanford University.

Hooper, A. (2008). A multi-temporal InSAR method incorporating both persistent scatterer and small baseline approaches. *Geophysical Research Letters*, 35(16).

Hooper, A., Zebker, H., Segall, P., & Kampes, B. (2004). A new method for measuring deformation on volcanoes and other natural terrains using InSAR persistent scatterers. *Geophysical Research Letters*, 31, 1-5.

Hu, R. L., Yue, Z. Q., Wang, L. U., & Wang, S. J. (2004). R eview on current status and challenging issues of land subsidence in China. *Engineering Geology*, 76(1), 65-77.

Hu, R., Wang, S., Lee, C., & Li, M. (2002). Characteristics and trends of land subsidence in Tanggu, Tianjin, China. *Bulletin of Engineering Geology and the Environment*, *61*(3), 213-225.

Huang, Q., Crosetto, M., Monserrat, O., & Crippa, B. (2017). Displacement monitoring and modelling of a high-speed railway bridge using C-band Sentinel-1 data. *ISPRS Journal of Photogrammetry and Remote Sensing*, 128, 204-211.

Hürlimann, M., Martí, J., & Ledesma, A. (2004). Morphological and geological aspects related to large slope failures on oceanic islands: The huge La Orotava landslides on Tenerife, Canary Islands. *Geomorphology*, 62, 143-158.

Ilieva, M., Polanin, P., Borkowski, A., Gruchlik, P., Smolak, K., Kowalski, A., & Rohm, W. (2019). Mining Deformation Life Cycle in the Light of InSAR and Deformation Models. *Remote Sensing*, 11(7), 745.

Imaizumi, F., Nishiguchi, T., Matsuoka, N., Trappmann, D., & Stoffel, M. (2018). Interpretation of recent alpine landscape system evolution using geomorphic mapping and L-band InSAR analysis. *Geomorphology*, 310, 125-137.

Intrieri, E., Raspini, F., Fumagalli, A., Lu, P., Del Conte, S., Farina, P., Allievi, J., Ferretti, A., & Casagli, N. (2018). The Maoxian landslide as seen from space: detecting precursors of failure with Sentinel-1 data. *Landslides*, *15*(1), 123-133.

Jebur, M. N., Pradhan, B., & Tehrany, M. S. (2015). Using ALOS PALSAR derived high-resolution DInSAR to detect slow-moving landslides in tropical forest: Cameron Highlands, Malaysia. *Geomatics, Natural Hazards and Risk*, 6(8), 741-759.

Johnson, K. S. (1998). Land subsidence above man-made salt-dissolution cavities. In Land subsidence case studies and current research: Proceedings of the Dr. Joseph F. Poland symposium on land subsidence. *Association of Engineering Geologists*, 8, 385-392.

Johnson, K. S. (2005). Subsidence hazards due to evaporite dissolution in the United States. *Environmental Geology*, 48(3), 395-409.

Jones, C. E., & Blom, R. G. (2014). Bayou Corne, Louisiana, sinkhole: Precursory deformation measured by radar interferometry. *Geology*, 42(2), 111-114.

Joyce, K. E., Belliss, S. E., Samsonov, S. V., McNeill, S. J., & Glassey, P. J. (2009). A review of the status of satellite remote sensing and image processing techniques for mapping natural hazards and disasters. *Progress in Physical Geography*, 33(2), 183-207.

Kalia, A. C., Frei, M., & Lege, T. (2017). A Copernicus downstream-service for the nationwide monitoring of surface displacements in Germany. *Remote Sensing of Environment*, 202, 234-249.

Kampes, B. M. (2006). *Radar interferometry: persistent scatterer technique* (Vol. 12). Springer Science & Business Media.

Karang, I. W. G. A., & Nishio, F. (2011). Internal waves in the Lombok Strait revealed by ALOS PALSAR images. In *Geoscience and Remote Sensing Symposium*, 2011. *IEEE International* (pp. 253-256). IEE.

Kenyi, L. W., & Kaufmann, V. (2003). Estimation of rock glacier surface deformation using SAR interferometry data. *IEEE Transactions on Geoscience and Remote Sensing*, 41(6), 1512-1515.

Ketelaar, V. B. H. (2009). Persistent Scatterer InSAR. In *Satellite Radar Interferometry: Subsidence Monitoring Techniques*, 27-49.

Kim, J. W., Lu, Z., & Degrandpre, K. (2016). Ongoing deformation of sinkholes in wink, texas, observed by time-series Sentinel-1a SAR interferometry (preliminary results). *Remote Sensing*, 8(4), 313.

Kim, S. W., Wdowinski, S., Dixon, T. H., Amelung, F., Kim, J. W., & Won, J. S. (2010). Measurements and predictions of subsidence induced by soil consolidation using persistent scatterer InSAR and a hyperbolic model. *Geophysical Research Letters*, *37*(5).

Kong, W.K. (2002). Risk assessment of slopes. *Quarterly Journal of Engineering Geology and Hydrogeology*, 35, 213–222.

Kos, A., Amann, F., Strozzi, T., Delaloye, R., Ruette, J., & Springman, S. (2016). Contemporary glacier retreat triggers a rapid landslide response, Great Aletsch Glacier, Switzerland. *Geophysical Research Letters*, 43(24).

Kvam, P. H., & Vidakovic, B. (2007). *Nonparametric statistics with applications to science and engineering* (Vol. 653, pp. 448). John Wiley & Sons.

Lagios, E., Sakkas, V., Parcharidis, I., & Dietrich, V. (2005). Ground deformation of Nisyros Volcano (Greece) for the period 1995–2002: Results from DInSAR and DGPS observations. *Bulletin of Volcanology*, 68(2), 201-214.

Lambeck, K., Antonioli, F., Anzidei, M., Ferranti, L., Leoni, G., Scicchitano, G., & Silenzi, S. (2011). Sea level change along the Italian coast during the Holocene and projections for the future. *Quaternary International*, 232, 250-257.

Lanari, R., Mora, O., Manunta, M., Mallorquí, J. J., Berardino, P., & Sansosti, E. (2004). A small-baseline approach for investigating deformations on full-resolution differential SAR interferograms. *IEEE Transactions on Geoscience and Remote Sensing*, 42(7), 1377-1386.

Lazecký, M., Rapant, P., Perissin, D., & Bakoň, M. (2014). Deformations of highway over undermined Ostrava-Svinov area monitored by InSAR using limited set of SAR images. *Procedia Technology*, 16, 414-421.

Lee, C. W., Lu, Z., Jung, H. S., Won, J. S., & Dzurisin, D. (2010). Surface deformation of Augustine Volcano, 1992-2005, from multiple-interferogram processing using a refined Small Baseline Subset (SBAS) Interferometric Synthetic Aperture Radar (InSAR) approach: Chapter 18 in The 2006 eruption of Augustine Volcano, Alaska (No. 1769-18, pp. 453-465). US Geological Survey.

Lillesand, T., Kiefer, R. W., & Chipman, J. (1979). *Remote sensing and image interpretation*. John Wiley & Sons, New York.

Liu, X., Xing, X., Wen, D., Chen, L., Yuan, Z., Liu, B., & Tan, J. (2019). Mining-Induced Time-Series Deformation Investigation Based on SBAS-InSAR Technique: A Case Study of Drilling Water Solution Rock Salt Mine. *Sensors*, 19(24), 5511.

Llanes, P., Herrera, R., Gómez, M., Muñoz, A., Acosta, J., Uchupi, E., & Smith, D. (2009). Geological evolution of the volcanic island La Gomera, Canary Islands, from analysis of its geomorphology. *Marine Geology*, 264 (3-4), 123-139.

Lomoschitz, A., Hervas, J., Yepes, J., & Meco J (2008). Characterisation of a Pleistocene debris-avalanche deposit in the Tenteniguada Basin, Gran Canaria Island, Spain. *Landslides*, 5, 227–234.

Longépé, N., Rakwatin, P., Isoguchi, O., Shimada, M., Uryu, Y., & Yulianto, K. (2011). Assessment of ALOS PALSAR 50 m orthorectified FBD data for regional land cover classification by support vector machines. *IEEE Transactions on Geoscience and Remote Sensing*, 49(6), 2135-2150.

Longpré, M.A., del Potro, R., Troll, V.R., & Nicoll, G.R. (2008). Engineering geology and future stability of the El Risco landslide, NW-Gran Canaria, Spain. *Bulletin of Engineering Geology and the Environment*, 67, 165.

López-Vinielles, J., Ezquerro, P., Fernández-Merodo, J. A., Béjar-Pizarro, M., Monserrat, O., Barra, A., Blanco, P., García-Robles, J., Filatov, A., García-Davalillo, J. C., Sarro, R., Mulas, J., Mateos, R. M., Azañón, J. M., Galve, J. P., & Herrera, G. (2020). Remote analysis of an open-pit slope failure: Las Cruces case study, Spain. *Landslides*, 1-16.

Lu, P., Casagli, N., & Catani, F. (2010). PSI-HSR: a new approach for representing Persistent Scatterer Interferometry (PSI) point targets using the hue and saturation scale. *International Journal of Remote Sensing*, 31(8), 2189-2196.

Luino, F. (2005). Sequence of instability processes triggered by heavy rainfall in the northern Italy. *Geomorphology*, 66(1-4), 13-39.

Lv, X., Yazıcı, B., Zeghal, M., Bennett, V., & Abdoun, T. (2014). Joint-scatterer processing for time-series InSAR. *IEEE Transactions on Geoscience and Remote Sensing*, 52(11), 7205-7221.

Ma, C., Cheng, X., Yang, Y., Zhang, X., Guo, Z., & Zou, Y. (2016). Investigation on mining subsidence based on multi-temporal InSAR and time-series analysis of the small baseline subset—Case study of working faces 22201-1/2 in Bu'ertai mine, Shendong coalfield, China. *Remote Sensing*, 8(11), 951.

Mancini, F., Stecchi, F., & Gabbianelli, G. (2009a). GIS-based assessment of risk due to salt mining activities at Tuzla (Bosnia and Herzegovina). *Engineering Geology*, 109(3), 170-182.

Mancini, F., Stecchi, F., Zanni, M., & Gabbianelli, G. (2009b). Monitoring ground subsidence induced by salt mining in the city of Tuzla (Bosnia and Herzegovina). *Environmental Geology*, 58(2), 381-389.

Manzella, A., Bonciani, R., Allansdottir, A., Botteghi, S., Donato, A., Giamberini, S., Lenzi, A., Paci, M., Pellizzone, A., & Scrocca, D. (2018). Environmental and social aspects of geothermal energy in Italy. *Geothermics*, *72*, 232-248.

Marinkovic, P., Larsen, Y., Levinsen, J. F., Broge, N. H., Sørensen, C. S., & Dehls, J. (2016). Something is "subsiding" in the state of Denmark-Operational prospects for nationwide subsidence mapping with Sentinel-1. In *ESA Living Planet Symposium 2016*.

Martha, T. R., Kerle, N., Jetten, V., van Westen, C. J., & Kumar, K. V. (2010). Characterising spectral, spatial and morphometric properties of landslides for semi-automatic detection using object-oriented methods. *Geomorphology*, *116*(1-2), 24-36.

Martí, J., & Gudmundsson, A. (2000). The Las Cañadas caldera (Tenerife, Canary Islands): an overlapping collapse caldera generated by magma-chamber migration. *Journal of Volcanology and Geothermal Research*, 103, 161-174.

Martí, J., Hurlimann, M., Ablay. G.J., & Gudmundsson, A. (1997). Vertical and lateral collapses in Tenerife and other ocean volcanic islands. *Geology*, 25, 879-882.

Martí, J., Mitjavila, J., & Araña, V. (1994). Stratigraphy, structure and geochronology of the Las Cañadas caldera (Tenerife, Canary Islands). *Geological Magazine*, 131, 715-727.

Martínez J.D., Johnson K.S., & Neal J.T. (1998). Sinkholes in evaporite rocks: Surface subsidence can develop within a matter of days when highly soluble rocks dissolve because of either natural or human causes. *American Scientist*, 86(1), 38-51.

Martinotti, G., Giordan, D., Giardino, M., & Ratto, S. (2011). Controlling factors for deep-seated gravitational slope deformation (DSGSD) in the Aosta Valley (NW Alps, Italy). *Geological Society of London*, Spec. Publ., 351, 113-131.

Massironi, M., Zampieri, D., Bianchi, M., Schiavo, A., & Franceschini, A. (2009). Use of PSInSAR™ data to infer active tectonics: Clues on the differential uplift across the Giudicarie belt (Central-Eastern Alps, Italy). *Tectonophysics*, 476(1), 297-303.

Massonnet, D., & Feigl, K. L. (1998). Radar interferometry and its application to changes in the Earth's surface. *Reviews of geophysics*, *36*(4), 441-500.

MATTM - Italian Ministry of the Environment and Protection of Land and Sea. Piano Straordinario di Telerilevamento Ambientale (PSTA); Linee guida per l'analisi dei dati intereferometrici satellitari in aree soggette a dissesti idrogeologici; MATTM: Rome, Italy, 2010 (p. 108).

Meckel, T. A., ten Brink, U. S., & Williams, S. J. (2006). Current subsidence rates due to compaction of Holocene sediments in southern Louisiana. *Geophysical Research Letters*, *33*(11).

Meisina, C., Notti, D., Zucca, F., Ceriani, M.,Colombo, A., Poggi, F., Roccati, A., & Zaccone, A. (2013). The use of PSInSAR™ and SqueeSAR™ techniques for updating landslide inventories. *Landslide Science and Practice*, 81-87. Springer.

Meisina, C., Zucca, F.,Notti, D., Colombo, A., Cucchi, A., Savio, G., Giannico, C., & Bianchi, M. (2008). Geological Interpretation of PSInSAR Data at Regional Scale. *Sensors*, 8, 7469–7492.

Menendez, I., Silva, P.G., Martin-Betancor, M., Perez-Torrado, F.J., Guillou, H., & Scaillet, S. (2008). Fluvial dissection, isostatic uplift, and geomorphological evolution of volcanic islands (Gran Canaria, Canary Islands, Spain). *Geomorphology*, 102, 189-203.

Meta A., Mittermayer J., Prats P., Scheiber R., & Steinbrecher U. (2010). TOPS imaging with TerraSAR-X: Mode design and performance analysis. *IEEE Transaction on Geoscience and Remote Sensing*, 40(2), 759–769.

Monserrat, O., Crosetto, M., Cuevas, M., & Crippa, B. (2011). The thermal expansion component of persistent scatterer interferometry observations. *IEEE Geoscience and Remote Sensing Letters*, 8(5), 864-868.

Monti Guarnieri A., & Prati C. (1996). ScanSAR focusing and interferometry. *IEEE Transaction on Geoscience and Remote Sensing*, 34(4), 1029–1038.

Monti Guarnieri A., & Rocca F. (1999). Combination of low- and highresolution SAR images for differential interferometry. *IEEE Transaction on Geoscience Remote Sensing*, 37, 2035-2049.

Montoya, L., & Masser, I. (2005). Management of natural hazard risk in Cartago, Costa Rica. *Habitat International*, 29, 493-509.

Mora, O., Mallorqui, J. J., Duro, J., & Broquetas, A. (2001). Long-term subsidence monitoring of urban areas using differential interferometric SAR techniques. In Geoscience and Remote Sensing Symposium, 2001. IGARSS'01. *IEEE 2001 International*, 3, 1104-110. IEEE.

Mora, O., Mallorqui, J.J., & Broquetas, A. (2003). Linear and nonlinear terrain deformation maps from a reduced set of interferometric SAR images. IEEE *Transaction on Geoscience Remote Sensing*, 41 (10), 2243–2253.

Moreira A., Mittermayer J., Scheiber R. (1996) Extended chirp scaling algorithm for air- and spaceborne SAR data processing in stripmap and ScanSAR imaging modes. *IEEE Transaction on Geoscience Remote Sensing*, 34(5), 1123–1136.

Morra Di Cella, U., Letey, S., Pogliotti, P., Curtaz, M., Cremonese, E., & Vagliasindi, M. (2011). Nuovo catasto dei rock glaciers della Valle d'Aosta. *Le modificazioni climatiche e i rischi naturali*; CNR IRPI, Bari, Italy, pp. 65-68.

Mura, J. C., Paradella, W. R., Gama, F. F., Silva, G. G., Galo, M., Camargo, P. O., Silva, A. Q., &. Silva, A. (2016). Monitoring of non-linear ground movement in an open pit iron mine based on an integration of advanced DInSAR techniques using TerraSAR-X data. *Remote Sensing*, 8(5), 409.

Nagler, T., Rott, H., & Kamelger, A. (2002). Analysis of landslides in Alpine areas by means of SAR interferometry. In Geoscience and Remote Sensing Symposium, 2002. IGARSS'02. *2002 IEEE International*,1, 198-200. IEEE.

Nannoni, R., & Capperi, M. (1989). *Miniere e minerali della Val di Cecina. Gruppo Mineralogico Cecinese*. Tipografie Grafiche Favillini, Livorno.

Neal, J. T. (1991). Prediction of subsidence resulting from creep closure of solutioned-mined caverns in salt domes. In *Proceedings of the 4th International Symposium on Land Subsidence. LAHS Publications, Houston, Texas, the USA* (pp. 225-234).

Ng, A. H. M., Ge, L., Du, Z., Wang, S., & Ma, C. (2017). Satellite radar interferometry for monitoring subsidence induced by longwall mining activity using Radarsat-2, Sentinel-1 and ALOS-2 data. *International Journal of Applied Earth Observation and Geoinformation*, 61, 92-103.

Nicolich, R., Primiero, A., Zgur, F., & Di Marzo, N. (2002). 3D Seismic Imaging and Numerical Modelling of Subsidence in Solution Mining of Rocksalt. In *64th EAGE Conference & Exhibition. European Association of Geoscientists & Engineers*.

Nof, R. N., Baer, G., Ziv, A., Raz, E., Atzori, S., & Salvi, S. (2013). Sinkhole precursors along the Dead Sea, Israel, revealed by SAR interferometry. *Geology*, 41(9), 1019-1022.

North, M., Farewell, T., Hallett, S., & Bertelle, A. (2017). Monitoring the response of roads and railways to seasonal soil movement with Persistent Scatterers Interferometry over six UK sites. *Remote sensing*, *9*(9), 922.

Notti, D., Calò, F., Cigna, F., Manunta, M., Herrera, G., Berti, M., Meisina C., Tapete D., & Zucca, F. (2015). A user-oriented methodology for DInSAR time series analysis and interpretation: Landslides and subsidence case studies. *Pure & Applied Geophysics*, 172(11), 3081.

Notti, D., Davalillo, J. C., Herrera, G., & Mora, O. (2010). Assessment of the performance of X-band satellite radar data for landslide mapping and monitoring: Upper Tena Valley case study. *Natural Hazards and Earth System Sciences*, 10(9), 1865.

Notti, D., Herrera, G., Bianchini, S., Meisina, C., García-Davalillo, J.C., & Zucca, F. (2014). A methodology for improving landslide PSI data analysis. *International Journal of Remote Sensing*, 35, 2186-2214.

Oliveira, S. C., Zêzere, J. L., Catalão, J., & Nico, G. (2015). The contribution of PSInSAR interferometry to landslide hazard in weak rock-dominated areas. *Landslides*, 12(4), 703-719.

Osmanoğlu, B., Dixon, T. H., Wdowinski, S., Cabral-Cano, E., & Jiang, Y. (2011). Mexico City subsidence observed with persistent scatterer InSAR. *International Journal of Applied Earth Observation and Geoinformation*, 13(1), 1-12.

Pagliara, P., Basile, G., Cara, P., Corazza, A., Duro, A., Manfrè, B., Onori, R., Proietti, C., & Sansone, V. (2014). Integration of earth observation and ground-based HR data in the civil protection emergency cycle: the case of the DORIS project. In *Mathematics of Planet Earth. Lecture Notes in Earth System Sciences*; Pardo-Igúzquiza, E., Guardiola-Albert, C., Heredia, J., Moreno-Merino, L., Durán, J., Vargas-Guzmán, J., Eds.; Springer Berlin, Heidelberg, Germany, pp. 263-266.

Paine, J. G., Buckley, S. M., Collins, E. W., & Wilson, C. R. (2012). Assessing collapse risk in evaporite sinkhole-prone areas using microgravimetry and radar interferometry. *Journal of Environmental and Engineering Geophysics*, 17(2), 75-87.

Papageorgiou, E., Foumelis, M., & Parcharidis, I. (2012). Long-and short-term deformation monitoring of Santorini Volcano: unrest evidence by DInSAR analysis. *IEEE Journal of Selected Topics in Applied Earth Observations and Remote Sensing*, 5(5), 1531-1537.

Papathoma-Köhle, M., Neuhäuser, B., Ratzinger, K., Wenzel, H., & Dominey-Howes, D. (2007). Elements at risk as a framework for assessing the vulnerability of communities to landslides. *Natural and Hazards Earth System*, 7(6), 765-779.

Paris, R., Guillou, H., Carracedo, J.C., & Pérez-Torrado, F.J. (2005). Volcanic and morphological evolution of La Gomera (Canary Islands), based on new K–Ar ages and magnetic stratigraphy: implications for oceanic island evolution. *Journal of Geological Society London*, 162, 501–512.

Pascucci, V., Fontanesi, G., Merlini, S., & Martini, I. P. (2001). Neogene Tuscan shelf-western Tuscany extension evidences of the early post-compressional deposits (Tyrrhenian Sea-Northern Apennines, Italy). Ofioliti, 26(2a), 187-196.

Patacca, E., Sartori, R., & Scandone, P. (1990). Tyrrhenian basin and Apenninic arcs: kinematic relations since late Tortonian times. *Società Geologica Italiana*, 45(1), 425-451.

Pawluszek-Filipiak, K., & Borkowski, A. (2020). Monitoring mining-induced subsidence by integrating differential radar interferometry and persistent scatterer techniques. *European Journal of Remote Sensing*, 1-13.

Peduto, D., Cascini, L., Arena, L., Ferlisi, S., Fornaro, G., & Reale, D. (2015). A general framework and related procedures for multiscale analyses of DInSAR data in subsiding urban areas. *ISPRS Journal of Photogrammetry and Remote Sensing*, 105, 186-210.

Peduto, D., Ferlisi, S., Nicodemo, G., Reale, D., Pisciotta, G., & Gullà, G. (2017). Empirical fragility and vulnerability curves for buildings exposed to slow-moving landslides at medium and large scales. *Landslides*, 1-15.

Peduto, D., Nicodemo, G., Maccabiani, J., & Ferlisi, S. (2017b) Multi-scale analysis of settlement-induced building damage using damage surveys and DInSAR data: A case study in The Netherlands. *Engineering Geology*, 218, 117-133.

Peel, M. C., Finlayson, B. L., & McMahon, T. A. (2007). Updated world map of the Köppen-Geiger climate classification. *Hydrology and Earth System Sciences Discussions*, *4*(2), 439-473.

Peltier, A., Bianchi, M., Kaminski, E., Komorowski, J. C., Rucci, A., & Staudacher, T. (2010). PSInSAR as a new tool to monitor pre-eruptive volcano ground deformation: Validation using GPS measurements on Piton de la Fournaise. *Geophysical Research Letters*, 37(12).

Pepe, A., & Lanari, R. (2006) On the extension of the minimum cost flow algorithm for phase unwrapping of multitemporal differential SAR interferograms. *IEEE Transactions on Geoscience Remote Sensing*, 44, 2374-2383.

Perissin, D., & Wang, T. (2012). Repeat-pass SAR interferometry with partially coherent targets. IEEE *Transactions on Geoscience Remote Sensing*, 50 (1), 271-280.

Perski, Z., Hanssen, R., Wojcik, A., & Wojciechowski, T. (2009). InSAR analyses of terrain deformation near the Wieliczka Salt Mine, Poland. *Engineering Geology*, 106(1), 58-67.

Peyret, M., Djamour, Y., Rizza, M., Ritz, J. F., Hurtrez, J. E., Goudarzi, M. A., Nankali, H., Chéry J., Le Dorz, K., & Uri, F. (2008). Monitoring of the large slow Kahrod landslide in Alborz mountain range (Iran) by GPS and SAR interferometry. *Engineering Geology*, 100(3), 131-141.

Pinna S. (2002). Rischi ambientali e difesa del territorio, (p. 176). Franco Angeli.

Plank, S. (2014). Rapid damage assessment by means of multi-temporal SAR—A comprehensive review and outlook to Sentinel-1. *Remote Sensing*, *6*(6), 4870-4906.

Poenaru, V. D., Badea, A., Savin, E., Teleaga, D., & Poncos, V. (2011). Land degradation monitoring in the Ocnele Mari salt mining area using satellite imagery. In *Earth Resources and Environmental Remote Sensing/GIS Applications II* (Vol. 8181, p. 81810U). *International Society for Optics and Photonics*.

Pohl, C., & Van Genderen, J. L. (1998). Review article multisensor image fusion in remote sensing: concepts, methods and applications. *International Journal of Remote Sensing*, *19*(5), 823-854.

Pratesi, F., Tapete, D.,Terenzi, G., Del Ventisette, C., & Moretti, S. (2015). Rating health and stability of engineering structures via classification indexes of InSAR Persistent Scatterers. *Journal of Applied Earth Observation and Geoinformation*, 40, 81-90.

Pritchard, M. E., & Simons, M. (2004). An InSAR-based survey of volcanic deformation in the southern Andes. *Geophysical Research Letters*, 31(15).

Przyłucka, M., Herrera, G., Graniczny, M., Colombo, D., & Béjar-Pizarro, M. (2015). Combination of conventional and advanced DInSAR to monitor very fast mining subsidence with TerraSAR-X Data: Bytom City (Poland). *Remote Sensing*, 7(5), 5300-5328.

Qu, F., Zhang, Q., Lu, Z., Zhao, C., Yang, C., & Zhang, J. (2014). Land subsidence and ground fissures in Xi'an, China 2005–2012 revealed by multi-band InSAR time-series analysis. *Remote Sensing of Environment*, 155, 366-376.

Rampello, S., & Callisto, L. (1998). A study on the subsoil of the Tower of Pisa based on results from standard and high-quality samples. *Canadian Geotechnical Journal*, 35, 1074-1092.

Rapetti, F., & Vittorini, S. (1994). Rainfall in Tuscany: observation about extreme events. *Rivista Geografica Italiana*, *101*, 47-76.

Raspini, F., Bardi, F., Bianchini, S., Ciampalini, A., Del Ventisette, C., Farina, P., *et al.* (2017). The contribution of satellite SAR-derived displacement measurements in landslide risk management practices. *Natural Hazards*, 86(1), 327-351.

Raspini, F., Bianchini, S., Ciampalini, A., Del Soldato, M., Solari, L., Novali, F., Del Conte, S., Ferretti, A., & Casagli, N. (2018). Continuous, semi-automatic monitoring of ground deformation using Sentinel-1 satellites. *Scientific reports*, *8*.

Raspini, F., Bianchini, S., Ciampalini, A., Del Soldato, M., Solari, L., Novali, F., Del Conte, S., Ferretti, A., & Casagli, N. (2017). Real time monitoring of ground deformation using Sentinel-1 satellites. Submitted to Nature Communications.

Raspini, F., Bianchini, S., Ciampalini, A., Del Soldato, M., Solari, L., Novali, F., Del Conte, S., Rucci, A., Ferretti, A., & Casagli, N. (2018). Continuous, semi-automatic monitoring of ground deformation using Sentinel-1 satellites. *Scientific Reports*, 8(1), 1-11.

Raspini, F., Bianchini, S., Moretti, S., Loupasakis, C., Rozos, D., Duro, J., & Garcia, M. (2016). Advanced interpretation of interferometric SAR data to detect, monitor and model ground subsidence: outcomes from the ESA-GMES Terrafirma project. *Natural Hazards*, 83(1), 155-181.

Raspini, F., Ciampalini, A., Del Conte, S., Lombardi, L., Nocentini, M., Gigli, G., Ferretti A., & Casagli, N. (2015). Exploitation of amplitude and phase of satellite SAR images for landslide mapping: the case of Montescaglioso (South Italy). *Remote Sensing*, 7(11), 14576-14596.

Ratto, S., Bonetto, F., & Comoglio, C. (2003). The October 2000 flooding in Valle d'Aosta (Italy): Event description and land planning measures for the risk mitigation. *International Journal of River Basin Management*, 1(2), 105-116.

Raucoules, D., Maisons, C., Carnec, C., Le Mouelic, S., King, C., & Hosford, S. (2003). Monitoring of slow ground deformation by ERS radar interferometry on the Vauvert salt mine (France): Comparison with ground-based measurement. *Remote Sensing of Environment*, 88(4), 468-478.

Raucoules, D., Parcharidis, I., Feurer, D., Novalli, F., Ferretti, N., Carnec, C., Lagios, E., Sakkas, V., Le Mouelic, S., Cooksley, G., & Hosford, S. (2008). Ground deformation detection of the greater area of Thessaloniki (Northern Greece) using radar interferometry techniques. *Natural Hazards and Earth System Sciences*, *8*(4), 779-788.

Refice, A., Bovenga, F., Guerriero, L., & Wasowski, J. (2001). DInSAR applications to landslide studies. In Geoscience and Remote Sensing Symposium, 2001. IGARSS'01. *IEEE 2001 International*, 1, 144-146. IEEE.

Richman, D. (1971) Three dimensional azimuth-correcting mapping radar, Tech. rep., USA: United Technologies Corporation.

Rocca, F. (2004). Diameters of the orbital tubes in long-term interferometric SAR surveys. *IEEE Geoscience and Remote Sensing Letters*, 1(3), 224-227.

Rodriguez-Gonzalez, A., Fernandez-Turiel, J.L., Perez-Torrado, F.J., Hansen, A., Aulinas, M., Carracedo, J.C., Gimeno, D., Guillou, H., Paris, R., & Paterne, M. (2009). The Holocene volcanic history of Gran Canaria island: implications for volcanic hazards. *Journal of Quaternary Science*, 24, 697-709.

Rogers, C.D.F. (1995). Types and distribution of collapsible soils. In *Genesis and Properties of Collapsible Soils*; Derbyshire, E., Dijkstra, T., Smalley, I.J., Eds.; Springer Netherlands: Amsterdam, *The Netherland*, 1-17.

Rosen, P. A., Hensley, S., Joughin, I. R., Li, F. K., Madsen, S. N., Rodriguez, E., & Goldstein, R. M. (2000). *Synthetic aperture radar interferometry. Proceedings of the IEEE*, 88(3), 333-382.

Rosi, A., Agostini, A., Tofani, V., & Casagli, N. (2014). A procedure to map subsidence at the regional scale using the persistent scatterer interferometry (PSI) technique. *Remote Sensing*, 6(11), 10510-10522.

Rosi, A., Segoni, S., Catani, F., & Casagli, N. (2012). Statistical and environmental analyses for the definition of a regional rainfall threshold system for landslide triggering in Tuscany (Italy). *Journal of Geographical Sciences*, *22*(4), 617-629.

Rosi, A., Tofani, V., Agostini, A., Tanteri, L., Stefanelli, C. T., Catani, F., & Casagli, N. (2016). Subsidence mapping at regional scale using persistent scatters interferometry (PSI): The case of Tuscany region (Italy). *International Journal of Applied Earth Observation and Geoinformation*, *52*, 328-337.

Rosi, A., Tofani, V., Tanteri, L., Stefanelli, C. T., Agostini, A., Catani, F., & Casagli, N. (2018). The new landslide inventory of Tuscany (Italy) updated with PS-InSAR: geomorphological features and landslide distribution. *Landslides*, *15*(1), 5-19.

Rossi, V., Amorosi, A., Sarti, G., & Potenza, M. (2011). Influence of inherited topography on the Holocene sedimentary evolution of coastal systems: An example from Arno coastal plain (Tuscany, Italy). *Geomorphology*, 135, 117-128.

Rucker, M. L., Panda, B. B., Meyers, R. A., & Lommler, J. C. (2013). Using InSAR to detect subsidence at brine wells, sinkhole sites, and mines. *Carbonates and Evaporites*, 28(1-2), 141-147.

Salvatici, T., Tofani, V., Rossi, G., D'Ambrosio, M., Stefanelli, C.T., Masi, E. B., *et al*. (2018). Application of a physically based model to forecast shallow landslides at a regional scale. *Natural Hazards and Earth System Sciences*, 18, 1919-1935, https://doi.org/10.5194/nhess-18-1919-2018.Haeberli, W., Hallet, B., Arenson, L., Elconin, R., Humlum, O., Kääb, A., *et al*. (2006). Permafrost creep and rock glacier dynamics. *Permafrost and Periglacial Processes*, 17(3), 189-214.

Samieie-Esfahany, S., Hanssen, R., van Thienen-Visser, K., & Muntendam-Bos, A. (2009, November). On the effect of horizontal deformation on InSAR subsidence estimates. *In Proceedings of the Fringe 2009 Workshop, Frascati, Italy* (Vol. 30).

Sarabandi, K., & Chiu, T. C. (1996). Optimum corner reflectors for calibration of imaging radars. *IEEE Transactions on Antennas and Propagation*, 44(10), 1348-1361.

Sarro, R., Mateos, R.M., Herrera, G., García-Moreno, I., Reichenbach, P., Carralero, I.P., Naranjo, J., Bejar-Pizarro, M., Monserrat, O., Solari, L., Onori, R., Barra, A., Bianchini, S., Lopez, C., Moretti, S., Gonzalez-Alonso, E., Ligüérzana, S., Ardizzone, F., Crosetto, M., & Pagliara, P. (2017). Methodology for assessing rockfall susceptibility within the ambit of civil protection: the Safety project. In: *Proceedings of the 6th Interdisciplinary Workshop on Rockfall Protection, Barcelona, Spain*.

Sarti, G., Bini, M., & Giacomelli, S. (2010). The growth and the decline of Pisa (Tuscany, Italy) up to the Middle ages: Correlations with landscape and geology. Geological setting and urban development of selected Italian towns up to the Middle ages and legacies of ancient problems throughout the ages. II Quaternario Italian *Journal of Quaternary Science*, 23, 311-322.

Sarti, G., Rossi, V., & Amorosi, A. (2012) Influence of Holocene stratigraphic architecture on ground surface settlements: A case study from the City of Pisa (Tuscany, Italy). *Sedimentary Geology*, 281, 75-87.

Sarychikhina, O., Glowacka, E., Mellors, R., & Vidal, F. S. (2011). Land subsidence in the Cerro Prieto Geothermal Field, Baja California, Mexico, from 1994 to 2005: An integrated analysis of DInSAR, leveling and geological data. *Journal of Volcanology and Geothermal Research*, 204(1), 76-90.

Sato, H. P., & Une, H. (2016). Detection of the 2015 Gorkha earthquake-induced landslide surface deformation in Kathmandu using InSAR images from PALSAR-2 data. *Earth, Planets and Space*, 68(1), 47.

Schmidt, D.A., & Bürgmann, R. (2003). Time-dependent land uplift and subsidence in the Santa Clara valley, California, from a large interferometric synthetic aperture radar data set. *Journal of Geophysical Research: Solid Earth*, 1978-2012.

Schuster, R. L., & Highland, L. (2001). *Socioeconomic and environmental impacts of landslides in the western hemisphere*. Denver (CO): US Department of the Interior, US Geological Survey.

Scifoni, S., Bonano, M., Marsella, M., Sonnessa, A., Tagliafierro, V., Manunta, M., Lanari, R., Ojha, C., & Sciotti, M. (2016) On the joint exploitation of long-term DInSAR time series and geological information for the investigation of ground settlements in the town of Roma (Italy). *Remote Sensing Environment*, 182, 113-127.

Shimada, M., Itoh, T., Motooka, T., Watanabe, M., Shiraishi, T., Thapa, R., & Lucas, R. (2014). New global forest/non-forest maps from ALOS PALSAR data (2007–2010). *Remote Sensing of Environment*, 155, 13-31.

Shirzaei, M., & Walter, T. R. (2011). Estimating the effect of satellite orbital error using wavelet-based robust regression applied to InSAR deformation data. *IEEE Transactions on Geoscience and Remote Sensing*, 49(11), 4600-4605.

Showstack, R. (2014). Sentinel satellites initiate new era in earth observation. *Transactions American Geophysical Union*, 95, 239-240.

Singh, G., Venkataraman, G., Yamaguchi, Y., & Park, S. E. (2014). Capability assessment of fully polarimetric ALOS–PALSAR data for discriminating wet snow from other scattering types in mountainous regions. *IEEE Transactions on Geoscience and Remote Sensing*, 52(2), 1177-1196.

Singhroy, V. (2009). *Satellite remote sensing applications for landslide detection and monitoring. In Landslides–Disaster Risk Reduction* (pp. 143-158). Springer Berlin Heidelberg.

Skolnik, M. L. (2001). *Introduction to RADAR systems*. 3 edn. 1221 Avenue of the Americas, New York, NY 10020. Tata McGraw-Hill.

Solari, L., Barra, A., Herrera, G., Bianchini, S., Monserrat, O., Béjar-Pizarro, M., Crosetto, M., Sarro, R., & Moretti, S. (2018a). Fast detection of ground motions on vulnerable elements using Sentinel-1 InSAR data. *Geomatics, Natural Hazards and Risk*, *9*(1), 152-174.

Solari, L., Barra, A., Herrera, G., Bianchini, S., Monserrat, O., Béjar-Pizarro, M., Crosetto, M., Sarro, R., & Moretti, S. (2017b), Vulnerable Elements Activity Maps based on Sentinel-1 InSAR. *Geomatics, Natural Hazards and Risk*, 1, 24.

Solari, L., Ciampalini, A., Raspini, F., Bianchini, S., & Moretti, S. (2016). PSInSAR analysis in the Pisa Urban Area (Italy): A case study of subsidence related to stratigraphical factors and urbanization. *Remote Sensing*, 8(2), 120.

Solari, L., Ciampalini, A., Raspini, F., Bianchini, S., Zinno, I., Bonano, M., Manunta M., Moretti S., & Casagli, N. (2017a). Combined Use of C-and X-Band SAR Data for Subsidence Monitoring in an Urban Area. *Geosciences*, 7(2), 21.

Solari, L., Del Soldato, M., Bianchini, S., Ciampalini, A., Ezquerro, P., Montalti, R., Raspini, F., & Moretti, S. (2018b). From ERS 1/2 to Sentinel-1: subsidence monitoring in Italy in the last two decades. *Frontiers in Earth Science*, *6*, 149.

Solari, L., Raspini, F., Del Soldato, M., Bianchini, S., Ciampalini, A., Ferrigno, F., Tucci, S., & Casagli, N. (2018c). Satellite radar data for back-analyzing a landslide event: the Ponzano (Central Italy) case study. *Landslides*, 15(4), 773-782.

Solari, L., Raspini, F., Del Soldato, M., Bianchini, S., Ciampalini, A., Ferrigno, F., Tucci, S., & Casagli, N. (2017c). Radar satellite data for back-monitoring of a landslide event: the Ponzano (Central Italy) case study. Submitted to *Landslides*.

Solaro, G., De Novellis, V., Castaldo, R., De Luca, C., Lanari, R., Manunta, M., & Casu, F. (2016). Coseismic fault model of mw 8.3 2015 illapel earthquake (CHILE) retrieved from multi-orbit sentinel1-A DInSAR measurements. *Remote Sensing*, 8(4), 323.

Sorooshian, S., Nguyen, P., Sellars, S., Braithwaite, D., AghaKouchak, A., & Hsu, K. (2014). Satellite-based remote sensing estimation of precipitation for early warning systems. *Extreme Natural Hazards Disaster Risks Soc Implications*, 1, 99-112.

Sousa, J. J., & Bastos, L. (2013). Multi-temporal SAR interferometry reveals acceleration of bridge sinking before collapse. *Natural Hazards and Earth System Sciences*, 13(3), 659.

Sowter, A., Amat, M. B. C., Cigna, F., Marsh, S., Athab, A., & Alshammari, L. (2016). Mexico City land subsidence in 2014–2015 with Sentinel-1 IW TOPS: Results using the Intermittent SBAS (ISBAS) technique. *International Journal of Applied Earth Observation and Geoinformation*, *52*, 230-242.

Spence, R. J., Baxter, P. J., & Zuccaro, G. (2004). Building vulnerability and human casualty estimation for a pyroclastic flow: a model and its application to Vesuvius. *Journal of Volcanology and Geothermal Research*, 133(1), 321-343.

Speranza, G., Cosentino, D., Tecce, F., & Faccenna, C., (2013). Paleoclimate reconstruction during the Messinian evaporative drawdown of the Mediterranean Basin: Insights from microthermometry on halite fluid inclusions. *Geochemistry, Geophysics, Geosystems*, 14(12), 5054-5077.

Speranza, G., Vona, A., Vinciguerra, S., & Romano, C. (2016). Relating natural heterogeneities and rheological properties of rocksalt: New insights from microstructural observations and petrophyisical parameters on Messinian halites from the Italian Peninsula. *Tectonophysics*, 666, 103-120.

Spizzichino, D., Margottini, C., Trigila, A., Iadanza, C., & Linser, S. (2010). Landslides. *Mapping the impacts of natural hazards and technological accidents in Europe. An overview of the last decade. European Environment Agency EEA Technical report*, *13*, 2010.

Spreckels, V., Wegmüller, U., Strozzi, T., Musiedlak, J., & Wichlacz, H. C. (2001). Detection and observation of underground coal mining-induced surface deformation with differential SAR interferometry. In *ISPRS Workshop" High Resolution Mapping from Space* (pp. 227-234).

Stecchi, F., Antonellini, M., & Gabbianelli, G. (2009). Curvature analysis as a tool for subsidence-related risk zones identification in the city of Tuzla (BiH). *Geomorphology*, 107(3), 316-325.

Stephens, M. A. (1970). Use of the Kolmogorov-Smirnov, Cramér-Von Mises and related statistics without extensive tables. *Journal of the Royal Statistical Society. Series B (Methodological)*, 115-122.

Stramondo, S., Cinti, F. R., Dragoni, M., Salvi, S., & Santini, S. (2002). The August 17, 1999 Izmit, Turkey, earthquake: Slip distribution from dislocation modeling of DInSAR and surface offset. *Annals of Geophysics*, 45(3-4), 527-536.

Strozzi T., Farina P., Corsini A., Ambrosi C., Thüring M., Zilger J., Wiesmann A., Wegmüller U., Werner C. (2005) Survey and monitoring of landslide displacements by means of L-band satellite SAR interferometry. *Landslides*, 193-201.

Sun, Q., Hu, J., Zhang, L., & Ding, X. (2016). Towards slow-moving landslide monitoring by integrating multi-sensor InSAR time series datasets: The Zhouqu case study, China. *Remote Sensing*, 8(11), 908.

Sun, Q., Zhang, L., Ding, X. L., Hu, J., Li, Z. W., & Zhu, J. J. (2015). Slope deformation prior to Zhouqu, China landslide from InSAR time series analysis. *Remote Sensing of Environment*, 156, 45-57.

Tang, P., Chen, F., Guo, H., Tian, B., Wang, X., & Ishwaran, N. (2015). Large-area landslides monitoring using advanced multi-temporal InSAR technique over the giant panda habitat, Sichuan, China. *Remote Sensing*, 7, 8925-8949.

Tantianuparp, P., Shi, X., Zhang, L., Balz, T., & Liao, M. (2013). Characterization of landslide deformations in Three Gorges area using multiple InSAR data stacks. *Remote Sensing*, 5, 2704-2719.

Tapete, D., Fanti, R., Cecchi, R., Petrangeli, P., & Casagli, N. (2012). Satellite radar interferometry for monitoring and early-stage warning of structural instability in archaeological sites. *Journal of Geophysics and Engineering*, 9(4), S10.

Terzaghi, K. & Peck, R.B. (1967). *Soil Mechanics in Engineering Practice*. John Wiley & Sons: Hoboken, NJ, USA.

Testa, G., & Lugli, S. (2000). Gypsum–anhydrite transformations in Messinian evaporites of central Tuscany (Italy). *Sedimentary Geology*, 130(3), 249-268.

Theron, A., & Engelbrecht, J. (2018). The Role of Earth Observation, with a Focus on SAR Interferometry, for Sinkhole Hazard Assessment. *Remote Sensing*, 10(10), 1506.

Tofani, V., Raspini, F., Catani, F., & Casagli, N. (2013). Persistent Scatterer Interferometry (PSI) technique for landslide characterization and monitoring. *Remote Sensing*, 5(3), 1045-1065.

Tofani, V., Segoni, S., Agostini, A., Catani, F., & Casagli, N. (2013). Use of remote sensing for landslide studies in Europe. *Natural Hazards and Earth System Sciences*, *13*(2), 299-309.

Tomás, R., Cano, M., Garcia-Barba, J., Vicente, F., Herrera, G., Lopez-Sanchez, J. M., & Mallorquí, J. J. (2013). Monitoring an earthfill dam using differential SAR interferometry: La Pedrera dam, Alicante, Spain. *Engineering geology*, 157, 21-32.

Tomás, R., García-Barba, J., Cano, M., Sanabria, M. P., Ivorra, S., Duro, J., & Herrera, G. (2012). Subsidence damage assessment of a gothic church using Differential Interferometry and field data. *Structural Health Monitoring*, 11(6), 751-762.

Tomás, R., Herrera, G., Delgado, J., Lopez-Sanchez, J. M., Mallorquí, J. J., & Mulas, J. (2010). A ground subsidence study based on DInSAR data: Calibration of soil parameters and subsidence prediction in Murcia City (Spain). *Engineering Geology*, 111(1), 19-30.

Tomás, R., Li, Z., Lopez-Sanchez, J. M., Liu, P., & Singleton, A. (2015). Using wavelet tools to analyse seasonal variations from InSAR time-series data: a case study of the Huangtupo landslide. *Landslides*, 1-14.

Tomás, R., Romero, R., Mulas, J., Marturià, J.J., Mallorquí, J.J., Lopez-Sanchez, J.M., *et al*. (2014). Radar interferometry techniques for the study of ground subsidence phenomena: a review of practical issues through cases in Spain. *Environmental Earth Science*, 71, 163-181.

Torres, R., Snoeij, P., Geudtner, D., Bibby, D., Davidson, M., Attema, E., Potin, P., Rommen, B., Floury, N., Brown, M., & Traver, I. N. (2012). GMES Sentinel-1 mission. *Remote Sensing of Environment*, *120*, 9-24.

Tosi, L., Da Lio, C., Strozzi, T., & Teatini, P. (2016). Combining L-and X-band SAR interferometry to assess ground displacements in heterogeneous coastal environments: The Po River Delta and Venice Lagoon, Italy. *Remote Sensing*, 8(4), 308.

Tralli, D. M., Blom, R. G., Zlotnicki, V., Donnellan, A., & Evans, D. L. (2005). Satellite remote sensing of earthquake, volcano, flood, landslide and coastal inundation hazards. ISPRS Journal of Photogrammetry and *Remote Sensing*, 59(4), 185-198.

Trasatti, E., Casu, F., Giunchi, C., Pepe, S., Solaro, G., Tagliaventi, S., Berardino P., Manzo M., Pepe A., Ricciardi G.P., Sansoti E., Tizzani P., Zeni G. & Lanari R. (2008). The 2004–2006 uplift episode at Campi Flegrei caldera (Italy): Constraints from SBAS-DInSAR ENVISAT data and Bayesian source inference. *Geophysical Research Letters*, 35(7).

Trigila, A., Iadanza, C., & Spizzichino, D. (2010). Quality assessment of the Italian Landslide Inventory using GIS processing. *Landslides*, 7, 455-470.

Uzielli, M., Nadim, F., Lacasse, S., & Kaynia, A.M. (2008). A conceptual framework for quantitative estimation of physical vulnerability to landslides. *Engineering Geology*, 102, 251-256.

Vai, F., & Martini, I. P. (Eds.). (2013). *Anatomy of an orogen: the Apennines and adjacent Mediterranean basins.* Springer.

Vajedian, S., Motagh, M., Mousavi, Z., Motaghi, K., Fielding, E., Akbari, B., Wetzel, H. U., & Darabi, A. (2018). Coseismic Deformation Field of the Mw 7.3 12 November 2017 Sarpol-e Zahab (Iran) Earthquake: A Decoupling Horizon in the Northern Zagros Mountains Inferred from InSAR Observations. *Remote Sensing*, *10*(10), 1589.

Valle d'Aosta Region Glaciers and Rock Glaciers Catalogue. http://catastoghiacciai.regione.vda.it/Ghiacciai/MainGhiacciai.html# (accessed on 3 August 2018).

van der Horst, T., Rutten, M. M., van de Giesen, N. C., & Hanssen, R. F. (2018). Monitoring land subsidence in Yangon, Myanmar using Sentinel-1 persistent scatterer interferometry and assessment of driving mechanisms. *Remote Sensing of Environment*, *217*, 101-110.

Van Westen, C. J., Castellanos, E., & Kuriakose, S. L. (2008). Spatial data for landslide susceptibility, hazard, and vulnerability assessment: an overview. *Engineering geology*, *102*(3-4), 112-131.

Vecchiotti, F., Peduto, D., & Strozzi, T. (2017). Multi-sensor a priori PSI visibility map for nationwide landslide detection in Austria. In *Workshop on World Landslide Forum* (pp. 45-52). Springer, Cham.

Wang, H., Liu-Zeng, J., Ng, A. M., Ge, L., Javed, F., Long, F., Aoudia, A., Feng, J., & Shao, Z. (2017). Sentinel-1 observations of the 2016 Menyuan earthquake: A buried reverse event linked to the left-lateral Haiyuan fault. *International Journal of Applied Earth Observation and Geoinformation*, *61*, 14-21.

Wang, S., Lu, X., Chen, Z., Zhang, G., Ma, T., Jia, P., & Li, B. (2020). Evaluating the Feasibility of illegal open-pit mining identification using insar coherence. *Remote Sensing*, 12(3), 367.

Wang, T., Perissin, D., Rocca, F., & Liao, M. S. (2011). Three Gorges Dam stability monitoring with time-series InSAR image analysis. *Science China Earth Sciences*, 54(5), 720-732.

Warren, J. K. (2016). *Solution Mining and Salt Cavern Usage. In Evaporites* (pp. 1303-1374). Springer International Publishing.

Watts, A., & Masson, D. (2001). New sonar evidence for recent catastrophic collapses of the north flank of Tenerife, Canary Islands. *Bulletin of Volcanology*, 63(1), 8-19.

Werner, C., Wegmüller, U., Strozzi, T., & Wiesmann, A. (2003). Interferometric point target analysis for deformation mapping. In *Proceedings of IGARSS 2003, Toulouse, France.*

Whyatt, J., & Varley, F. (2008). *Catastrophic failures of underground evaporite mines*. In *Proceedings: 27th International Conference on Ground Control in Mining* (pp. 29-31).

Wright, T. J., Hooper, A. J., Marinkovic, P., González, P. J., Walters, R., Elliott, J. R., Ebmeier S. K., & Larsen, Y. (2014). The Sentinel-1 Constellation-A new era of operational InSAR. In AGU Fall Meeting Abstracts, December 2014.

Xia, Y., Kaufmann, H., & Guo, X. (2002). Differential SAR interferometry using corner reflectors. In Geoscience and Remote Sensing Symposium, 2002. IGARSS'02. *2002 IEEE International*, 2, 1243-1246. IEEE.

Yagüe-Martínez, N., Prats-Iraola, P., Gonzalez, F. R., Brcic, R., Shau, R., Geudtner, D., Eineder M., & Bamler, R. (2016) Interferometric processing of Sentinel-1 TOPS data. *IEEE Transactions on Geoscience and Remote Sensing*, 54(4), 2220-2234.

Yang, Z., Li, Z., Zhu, J., Yi, H., Hu, J., & Feng, G. (2017). Deriving dynamic subsidence of coal mining areas using InSAR and logistic model. *Remote Sensing*, 9(2), 125.

Yonezawa, C., Watanabe, M., & Saito, G. (2012). Polarimetric decomposition analysis of ALOS PALSAR observation data before and after a landslide event. *Remote Sensing*, 4(8), 2314-2328.

Zamfirescu, F., Mocuta, M., Constantinecu, T., Medves, E., & Danchiv, A. (2003). The main causes of a geomechanical accident of brine caverns at field II of Ocnele Mari-Romania. *Materials and Geoenvironment*, 50, 431-434.

Zebker, H. A., Rosen, P. A., & Hensley, S. (1997). Atmospheric effects in interferometric synthetic aperture radar surface deformation and topographic maps. *Journal of Geophysical research and Solid Earth*, 102(B4), 7547-7563.

Zhang, A., Lu, J., & Kim, J. W. (2018). Detecting mining-induced ground deformation and associated hazards using spaceborne InSAR techniques. *Geomatics, Natural Hazards and Risk*, 9(1), 211-223.